Estimating Period Lengthening of High-Rise Buildings

Application of vibration-based FE model updating on a small-scale steel tower structure for period lengthening estimation.

CIEM0500 Master Thesis

C.D. Rijna

Delft University of Technology

TU Delft

Estimating Period Lengthening of High-Rise Buildings

Application of vibration-based FE model updating on a small-scale steel tower structure for period lengthening estimation.

by

C.D. Rijna

Student Name	Student Number
Coen Rijna	4696441

Supervisor TNO:	A. J. Bronkhorst & D. Moretti
Supervisors TU Delft:	E. Lourens & A. Tsetas
Project Duration:	January, 2024 - October, 2024
Faculty:	Faculty of Civil Engineering and Geosciences, Delft

Style: TU Delft Report Style, with modifications by Daan Zwaneveld

TU Delft

Preface

This master's thesis concludes my studies at Delft University of Technology (TU Delft) in pursuit of a Master's degree in Civil Engineering. My research explores estimating period lengthening $\frac{\tilde{T}}{T}$ in structures through model updating, a promising approach for enhancing damping predictions in high-rise buildings.

When it came time to choose a subject for my master's thesis, I discovered the research TNO was conducting as part of the HiViBE project—a consortium of industry players working to improve predictions of dynamic properties for high-rise buildings in the Netherlands. Living in Rotterdam, the Netherlands' "skyscraper city," I had been intrigued by the engineering innovations enabling the construction of tall buildings, especially given the country's soft soil conditions. This made the topic even more compelling to me.

The research topic offered a perfect blend of my academic background and personal interests. It focused on incorporating soil-structure interaction as a factor in predicting the damping ratios of buildings. This allowed me to merge my knowledge of structural dynamics with geo-technical engineering, creating a well-rounded and intellectually stimulating project.

Working on this thesis was both a rewarding and challenging experience. Structural dynamics is often regarded as a complex field, and the inclusion of damping mechanisms adds further layers of difficulty. I recall speaking with a professor of computational mechanics, another demanding area within civil engineering, who simply responded with "oof" when I mentioned that my research involved damping. This reaction reflected the challenges ahead, but I kept determined about making a step forward with regard to the subject.

On a personal level, completing this thesis pushed me well beyond my comfort zone, as it was the first time I had managed a project of this scale independently. There were times when the scope and complexity felt overwhelming, but—thanks to the invaluable support and advice from friends, family, and supervisors—I was able to stay on track and push forward. This experience taught me what research truly is about: not simply "doing a lot of work" or arriving at a final answer, but going for a deeper understanding of both the process and the underlying mechanics of what you do. After my last progress meeting, I took a closer look at the meaning of the results I produced, looking for answers and explanations, and it was only then that I fully understood the relevance and impact of my work.

I am ultimately proud of the outcomes of this thesis. The results demonstrate the potential of the model updating approach to estimate period lengthening with some degree of accuracy. At the same time, the research uncovered various challenges that must be addressed before this method can be reliably applied to real-world structures. Most important among these are the uncertainties involved, which stem from both the complexity of the models and the variability of real-world conditions.

This project has deepened my understanding of structural dynamics and performing research as a whole. I hope it will be useful for future research, contributing to the ongoing effort to improve the design and safety of high-rise buildings in the Netherlands and beyond.

Finally, I would like to express my heartfelt gratitude to my supervisors, friends, and family for their unwavering support, guidance, and encouragement the past months, without them I would not have been able to finish this project succesfully!

C.D. Rijna
Delft, November 2024

Summary

This thesis investigates the possibility of estimating the period lengthening ($\tilde{T}/T$) of structures through a process called model updating. Period lengthening refers to the elongation of a structure's first natural frequency due to changes in boundary conditions, such as the introduction of a flexible base, which is an important factor in understanding soil-structure interaction and predicting the modal damping ratio of the fundamental mode of buildings, which governs wind-induced vibrations.
The research employs a 2D finite element (FE) model, based on Timoshenko beam elements, to simulate the dynamic behavior of a small-scale steel structure for which vibration measurements were previously conducted. These measurements provided dynamic properties such as natural frequencies and mode shapes. The structural properties of the FE model were updated using a Sequential Least Squares Quadratic Programming (SLSQP) algorithm to minimize discrepancies between the measured and simulated dynamic properties. This process allowed for the determination of period lengthening and its comparison with values derived from the previous experimental studies.

The research was conducted in two phases. In the first phase, synthetic modal data were used to validate the model updating approach and investigate the approach in a situation without model or measurement errors. This demonstrated that the algorithm effectively resolves the stiffness-to-mass ratios ($\frac{E_{steel}}{\rho}$ and $\frac{E_{steel}}{E_{spring}}$) rather than accurately determining individual properties. The comparison between stiff and soft springs revealed that period lengthening predictions for stiff springs were more accurate and stable, whereas soft springs exhibited greater sensitivity and larger discrepancies in the results.

In the second phase, real measurement data were used to update the FE model. The results were generally consistent with the synthetic data, although the optimization process revealed variations in period lengthening estimates due to the presence of a "plateau" in the cost function. This plateau was a region where the cost function did not really improve, despite different properties and resulting period lengthening values. This indicated that the model was unable to fit all dynamic properties perfectly, highlighting the influence of both model and measurement uncertainties.

The findings show that model updating can effectively estimate period lengthening, particularly for flexible foundations. However, the accuracy of the results is heavily dependent on both modeling and measurement uncertainties. It is important to critically assess results from the optimization, to determine if the optimization has fully converged and wether uncertainty of the parameter is small enough. Further research is recommended to address these uncertainties and refine the method for potential use in real-world applications, particularly in high-rise building design.

Contents

1 Introduction

1.1. Research context

Buildings in the Netherlands are becoming taller, more slender, and lighter, making them more susceptible to wind-induced vibrations. Current calculation methods do not accurately predict the actual vibration behavior of high-rise buildings [2]. This phenomenon is mainly caused by inaccurate prediction of building properties in the design phase. One of such design variables that has a large influence on the dynamic response is the damping ratio. Full scale measurements have shown a discrepancy between in-situ and design values of the modal damping ratio of the fundamental mode [3]. This discrepancy can lead to several undesirable situations: due to an overestimation of damping, high accelerations of high-rise buildings that can cause a diminished sense of safety in the building, but can also lead to the sopite syndrome, a form of mild motion sickness [17] . An underestimation of damping may lead to building designs that are too conservative and will therefore be unsustainable and cost-inefficient. To improve predictions, a consortium of market parties (the HiViBE consortium), led by TNO, has initiated a multi-year research program [1]. This thesis will serve as a part of this research program and will specifically focus on methods to improve the predictions of damping values of high-rise structures in the Netherlands.

When talking about damping of vibrations in high-rise buildings, one often means the damping value associated with the fundamental mode of the structure, since the response of this kind of structures is mainly governed by the response of the fundamental mode [3]. Before 1975, most studies on dynamic behavior and damping of high-rise buildings have been focusing on Ultimate Limit State (ULS) conditions, mainly caused by earthquake excitation [26]. Later, Serviceability Limit State (SLS) conditions due to wind loads became more important due to the previously mentioned changing characteristics of high-rise buildings. Several researchers, such as Jeary [13], Tamura [29], Lagomarsino [16] and Davenport and Hill-Caroll [10], proposed damping predictors for the SLS of tall buildings based on full-scale measurements. Bronkhorst et al. [3] showed that the damping estimated by these different empirical predictors and additionally by the Dutch design codes (such as NEN-EN 1991-1-4 [30] and NEN-EN 1990 [22]), can deviate significantly from the measured damping in Dutch high-rise buildings [4]. Several studies have identified a large influence of soil structure interaction (SSI) on the overall damping ratio of high-rise buildings [27][9] [4] and Gomez [26], who studied the relation between foundation stiffness and overall damping ratio, found a correlation suggesting that a lower foundation stiffness leads to a higher contribution of foundation damping to the overall damping ratio. Dutch soft soil conditions could therefore partly explain the deviation of damping values from design codes and empirical predictors.

In seismic design, Soil Structure Interaction (SSI) is often modeled with the substructure approach, using springs and dashpots to represent stiffness and damping of the foundation [23]. One approach to include soil-structure interaction is by modifying the damping ratio of the fundamental mode, through the use of the period lengthening ($\frac{\tilde{T}}{T}$) [23]. Veletsos and Meek [33] developed a theoretical relationship between building-, foundation-, and overall-damping of the fundamental mode through this parameter.

Cruz and Miranda [9] developed an analytical model based on the theoretical relationship of Veletsos et al. and found that for seismic vibrations, the change in overall damping ratio with increasing height mainly depends on SSI. Carranza et al. [4] showed that this approach is also applicable to high-rise buildings exposed to wind induced vibrations. He compared Eurocode predictions (NEN- EN 1991-1-4 [30]) of the damping ratio of the fundamental mode of a 154 m tall residential high-rise building in the Netherlands to predictions by an equivalent single-degree of freedom (SDOF) model with modified damping ratio (according to the period lengthening). This study showed that the estimated damping ratio using the SSI model was only 8% higher than the measured values, whereas the Eurocode predictions overestimated the damping value with 90 %. This result suggests that application of the SSI model could offer a better estimate of the damping at the design stage than determined using Dutch design codes (NEN-EN 1991-1-4 [30]) and NEN-EN 1990 [22]).

1.2. Research problem

Although results of the SSI modelling approach proposed by Cruz and Miranda [9] and Carranza et al. [5] are promising for a better prediction of wind-induced vibrations, several problems exist that prevent the approach from being used in design for high-rise buildings. First, both studies make different assumptions about the magnitude of the building- and the foundation damping (ζ_b and ζ_f respectively). It is unclear which assumptions lead to an optimal result of the overall damping ratio of the fundamental mode (ζ_0). Secondly, the period lengthening cannot be directly measured and therefore, there is no database with period lengthening values for a large set of buildings. This means it cannot be investigated which assumptions made about building- and foundation damping lead to an optimal result of the overall damping as computed using the SSI model. The third problem is about the estimation of building properties: during the design phase, there is uncertainty in determining the exact structural properties of a building, such as mass, stiffness, and damping characteristics. These properties are often based on assumptions or generalized models, which may not accurately reflect the true behavior of the building once constructed. This uncertainty complicates the prediction of dynamic behavior, including period lengthening. To be able to calculate the period lengthening based on structural properties of buildings, model updating could be applied. This method involves adjusting the parameters of a computational model to better match the measured dynamic response of a structure. By comparing the observed modal characteristics, such as natural frequencies and mode shapes, with those predicted by the model, the model parameters are iteratively refined to minimize the discrepancy between them. This approach enhances the accuracy of the model in representing the actual behavior of the structure, making it a powerful tool for predicting period lengthening.A preliminary study conducted prior to this thesis attempted to estimate the period lengthening of several buildings in Japan using an Euler-Bernoulli beam model with uniformly distributed mass and stiffness. While the results were promising, it was not possible to fully evaluate the method. In real-life situations, each building typically exists on a single, flexible foundation, and it is impossible to place a building on different base conditions or foundations to directly investigate period lengthening. This limitation makes it challenging to validate the accuracy of the model across varying conditions.

1.3. Research objective

The goal of this study is to develop a reliable method to determine the period lengthening ($\frac{\tilde{T}}{T}$) of a structure through model updating of a Finite Element (FE) model and to investigate which conditions play a role in the accuracy and precision of the outcome.

1.4. Research scope

This research will investigate the possibility of determining the period lengthening by model updating of a 2D FE-model, such that its dynamic properties match the dynamic properties of a small-scale steel frame. The natural frequencies and mode shapes used for the updating, correspond to bending modes in one direction only, with torsional modes excluded from consideration. Therefore, a 2D FE model and updating code was developed in python. These measured dynamic properties are obtained from previous research by Elisa Marchelli [18] and the process of obtaining those is not part of this research. The research will only cover the updating of the developed 2D FE model, no other types of models are investigated. The main focus is determining the value for period lengthening, and reflect on the accuracy of the procedure. It will not try to conclude something on the contribution to the modal damping ratio by building and foundation.

Figure 1.1: The small-scale steel building model of which vibration measurements were taken by Marchelli [18]. These measurement were then used to update properties of a FE model in this thesis, to determine the period lengthening.

1.5. Research questions

The main research question of this thesis is the following:

"How can the period lengthening of a structure be estimated reliably through model updating based on vibration measurements?"

To address the main research question of this thesis, it has been broken down into three specific research questions:

1. What parameters play a large role when estimating the period lengthening of a structure by model updating a 2D FE model.
2. What is the optimal setup for a model updating procedure to reliably estimate the period lengthening of a structure?
3. How well do period lengthening values computed through model updating of a 2D FE model compare to values obtained from measurements on a small-scale steel model.

This thesis aims to achieve several key objectives by exploring the research questions outlined. Specifically, it will evaluate the feasibility of determining period lengthening through model updating. This evaluation will involve analyzing the settings and input values of the optimization algorithm used to update the system parameters. Additionally, the accuracy of the algorithm's output will be assessed by comparing it to measured data. Through this process, the thesis will determine whether the approach produces sufficiently accurate results, which are necessary for understanding the damping distribution in buildings. Moreover, key challenges encountered during the process will be identified.

2
Literature Review

In this section, a literature review will be presented that focuses on background information and theories regarding the complexity of damping mechanisms of wind-induced vibrations in high rise buildings. In addition, current design practices and their limitations will be discussed. The chapter aims to identify research gaps and explain the setting and relevance of this study. In section 2.1, the background and motivations for this study are explained. In section 2.1.4, state-of-the-art modelling approaches focused on wind induced vibrations of high rise buildings are discussed and finally, in section 2.4, model updating and the application of it in this study is discussed.

2.1. Background

2.1.1. Recent developments in high-rise buildings in the Netherlands

The Dutch population has been growing for the last decades and this growth is generally concentrated in the Randstad, a metropolitan region in the west of the Netherlands [11]. In the vision of the Dutch government [19], one of the proposed solutions for the large population growth is to increase the density of this area. High-rise buildings are mentioned as an inspiring way to achieve this. Therefore, the amount of buildings higher than 70 meters has doubled since 2008 [12] and several larger Dutch cities have now published vision documents on high-rise buildings.

Two developments that characterize the development of high-rise buildings in the Netherlands are the increasing slenderness of buildings and the use of lighter materials [2]. Typically, slenderness is increasing with increasing building height, due to daylight requirements in cities, which dictate limitations to floor surface area for buildings higher than 70 meters [2] [25]. More slender buildings are more susceptible to wind-induced vibrations. In addition to increasing slenderness, lighter materials are used in the construction of HRB, following a trend within the building industry towards more sustainable designs of structures [2]. Heavy buildings are more vulnerable to horizontal vibrations[2]. Overall, these trends make HRB more susceptible to wind-induced vibrations.

2.1.2. Relevance of damping in wind-induced vibrations of HRB

Because of the increased susceptibility of wind induced vibrations, it becomes more important to understand the dynamic behaviour of HRB. Damping, which represents the energy loss during vibration, remains the most uncertain design parameter that needs to be determined [2] [26]. This is because the vibration energy is lost during a variety of uncertain and intricate processes or damping mechanisms, which will be discussed in section 2.1.3. The modal damping ratio is usually denoted using the letter ζ and is defined as the ratio between the actual damping and the critical damping, which is the minimum amount of damping required to prevent a system from oscillating or vibrating. More knowledge on damping of high-rise buildings is necessary because the parameter highly affects peak accelerations in buildings. The peak acceleration is the maximum acceleration that can occur in a building due to wind-induced vibration [30]. The main structural parameters determining the response are (1) the natural frequency and (2) the damping ratio of the building [2]. This research will focus on the damping ratio. To visualize the strong dependency between the damping ratio and the peak acceleration, Bronkhorst et al. Bronkhorst, Bentum, and Gomez performed a case study showing how the peak acceleration of a specific building is affected by the choice of damping ratio. He calculated this peak acceleration in the range of damping ratios estimated by various empirical damping predictors. A plot of this study can be seen in figure 2.2 (a).

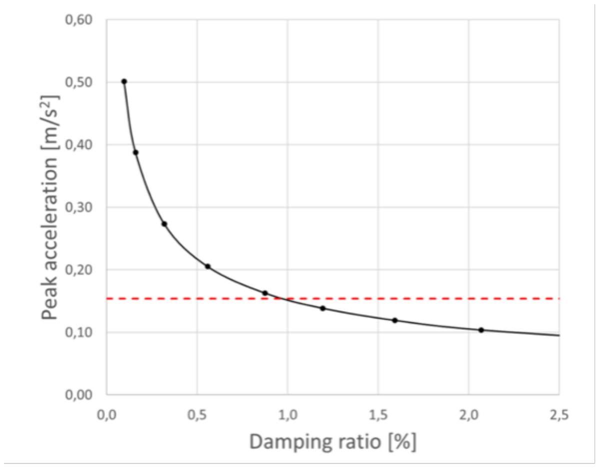

Figure 2.1: Sensitivity analysis performed by [2] to see how peak acceleration is affected by the damping ratio for a specific building. The limit value according to NEN 6702 is specified by the dashed red line.

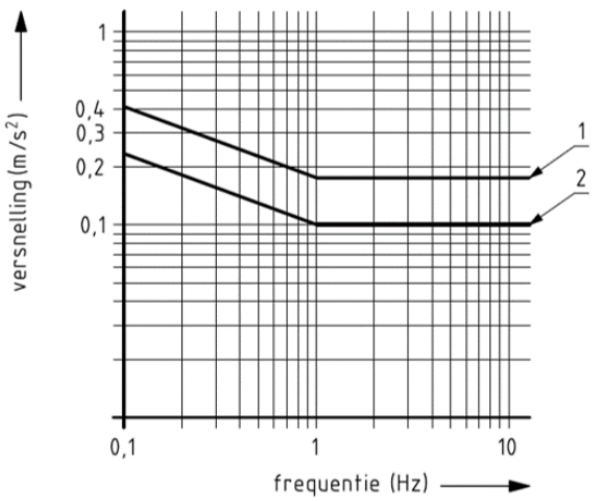

Figure 2.2: Limit values specified by NEN 6702 for the peak acceleration with a return period of 1 year for wind-induced vibrations in buildings. 1 = office function, 2 = living function [22].

Limits on allowable peak accelerations in the Netherlands can be found on in NEN 6702. In this design code, SLS (Serviceability Limit State) conditions have been defined for buildings in the Netherlands. These limits can be seen in figure 2.2. In current design practice however, often the (more strict) criteria from ISO 10137 are used. With these criteria it becomes difficult to meet comfort levels for buildings over 150-200 m.
Peak accelerations can be calculated using the procedure in EN 1991-1-4 [30], which will be further explained in section 2.2

2.1.3. Damping mechanisms

Davenport and Hill-Carrol [10] describe four damping mechanisms for high-rise buildings: (1) intrinsic material damping (main mechanism in the main load bearing structure (MLBS)), (2) frictional damping (main mechanism in the non-structural elements), (3) aerodynamic damping and (4) radiation damping (damping in the foundation). Others, such as Jeary [14] and Smith and Willford [28] have progressed

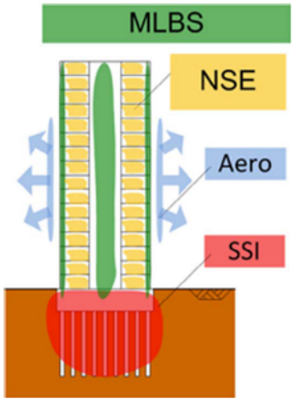

Figure 2.3: Visual representation of a building with several damping mechanisms as identified by [26]

further on these concepts by describing several damping mechanisms. In table 2.1, a summary of these damping mechanisms is portrayed, using the description as proposed by Gomez [26]. Auxiliary damping is added, which is described by Carranza [4]. Important to note is that this study focuses on the overall damping ratio, which includes all of the individual damping mechanisms described in table 2.1. It aims at determining the period lengthening to separate the contribution to the overall damping by the foundation damping from the contribution by the building damping. This is further explained in section 2.2.3

2.1.4. Estimation of damping in design practices

Damping ratios of buildings can be estimated using the European code EN 1991-1-4 [30]. The values made available in this code are obtained by field experiments on high-rise buildings, mostly from other countries than the Netherlands, and can be seen as rough estimates [2]. The damping values are fixed and depend only on the material of the main load-bearing structure of a building (such as steel, concrete or mixed). Values can be found in figure 2.5.

Empirical damping estimators

The Eurocode formulation of damping assigns values for overall damping of the fundamental mode based on building material (steel, concrete or mixed). To include parameters such as building height, aspect ratio and natural frequency, several researchers, such as Jeary [13], Tamura [29], Lagomarsino [16] and Davenport and Hill-Caroll[10], have developed alternative damping estimators. These estimators are based on empirical relations between parameters and measured damping ratio's of buildings and none seems to fully capture the damping behaviour of high rise buildings [2]. An overview of the researchers and their proposed damping estimators can be seen in figure 2.5. Important to note is that none of these damping estimators give insight in the distribution over different building components, nor do they include SSI as one of the governing factors in the overall damping ratio [2].

2.1.5. Applicability of estimators

Bronkhorst et al. [2] showed that both Eurocode procedure and the several damping predictors proposed by researchers largely deviate from measured damping ratios of buildings. For most buildings, this difference between measured and predicted values is large (more than 50%) and the differentiation made in most models between concrete and steel buildings is not apparent from these measurement results. This underlines the need for a more accurate method for damping estimation.

2.2. Modified damping to include SSI effects

2.2.1. Current design practice: Eurocode model

To determine the response of high-rise buildings to wind forces, modal analysis is performed. In modal analysis, the total response of the structure is described as the superposition of vibration modes [5]. The maximum response of each mode can individually be described as a single degree of freedom

Table 2.1: Description of several damping mechanisms in a building as identified by [26]

Building component	Damping mechanism
Main load bearing structure (MLBS)	Consists of three mechanisms 1. Material damping is caused by energy dissipation in the form of heat, due to friction of molecules. In the lab, damping ratios for pure materials such as concrete and steel can be found according to Smith and Willford [4]. 2. Slip on connections 3. Yielding of structural elements
Non-structural elements (NSE)	facades, partition walls, cladding, fixed furniture and mechanical and electrical shafts. Deform as structural elements deform, but energy dissipation generally much weaker [4].
Aerodynamic /external damping	Aerodynamic damping in high-rise buildings refers to the energy dissipation caused by the interaction between the building's vibrations and the surrounding air during wind-induced motions. However, it is often considered negligible because the wind speed is significantly higher than the building's vibration speed, making the wind's influence on the relative motion dominant. As a result, the resistive forces generated by the building's movement against the wind are too small to meaningfully reduce vibration amplitudes and therefore Aerodynamic damping is often considered negligible [4]
Auxiliary/supplementary damping	Elements that are added to a structure to increase the amount of damping, such as tuned mass dampers, tuned liquid dampers, friction dampers and viscous and visco-elastic dampers. These elements can increase overall damping with up to 5% [4].
Foundation damping	Energy dissipation in the foundation is mainly through: 1. *Hysteretic damping:* energy dissipation due to internal friction within the soil material, occuring in hysteretic loops when loaded cyclically [2] [4] 2. *Wave radiation or geometric damping:* energy dissipation through the radiation of elastic waves in the soil [4].

Reference	Damping estimator [%]	Limit value
EN 1991-1-4 [5]	$\zeta = 0.8$ (steel) * $\zeta = 1.6$ (concrete) * $\zeta = 1.2$ (mixed) *	-
Davenport and Hill-Caroll [17]	$\zeta = 3(\sigma_x/H)^{0.075}$ (5 – 20 stories, steel) $\zeta = 3(\sigma_x/H)^{0.11}$ (5 – 20 stories, concrete) $\zeta = 2(\sigma_x/H)^{0.11}$ (> 20 stories, steel) $\zeta = 2.5(\sigma_x/H)^{0.11}$ (> 20 stories, concrete)	-
Jeary [18]	$\zeta = f_n + 10^{\sqrt{d}/2} \cdot x/H + 0.15$	$\zeta \leq 60/H + 1.3$
Tamura et al. [19]	$\zeta = 1.3f_n + 4 \cdot 10^4 \cdot x/H + 0.29$ (steel) $\zeta = 1.4f_n + 4.7 \cdot 10^4 \cdot x/H - 0.18$ (concrete)	$x/H < 2 \cdot 10^{-5}$
Lagomarsino [20]	$\zeta = 0.32f_n + 0.78/f_n$ (steel) $\zeta = 0.72f_n + 0.70/f_n$ (concrete) $\zeta = 0.29f_n + 1.29/f_n$ (mixed)	-

Figure 2.4: Overview of empirical damping estimators and damping estimators specified by Dutch design codes. Taken from [2]. x is the maximum displacement at the top of the building (in m), σ_x is the standard deviation of the displacement at the top of the building (in mm), H and d are the height and width of the building (in m) and f_n is the natural frequency of the building.

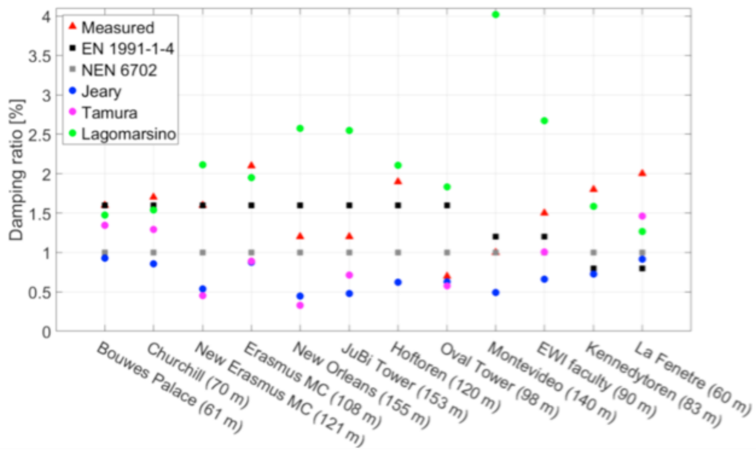

Figure 2.5: Predicted and measured damping for 12 high-rise buildings in the Netherlands (H ≥ 60 m). The first 8 buildings have a concrete structure, the Montevideo and EWI faculty have a mixed structure, and the Kennedytoren and La Fenetre have a steel structure. The height of the load-bearing part of the building structure is specified between brackets (i.e. antennas, masts or special roof structures are not considered). Taken from [2]

system (SDOF) with a modal mass, stiffness and damping. The Eurocode describes a procedure to calculate the peak acceleration of a high-rise building based on an equivalent SDOF that describes the first mode of vibration of the building [30] [2]. This is, because the first mode commonly governs the maximum dynamic response of a high-rise building under wind load [26] [4]. In figure 2.6, the Eurocode model is depicted. The stiffness k_i in this figure, represents the stiffness of the building only. Soil stiffness and therefore soil damping is not included in the current approach.

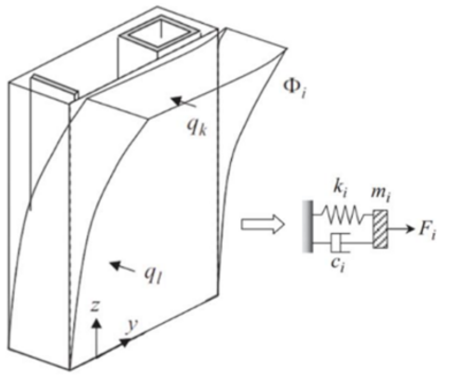

Figure 2.6: Structural model used in the EN 1991-1-4 [4] and approximation as a single degree of freedom (as first mode governs maximum response in wind-induced vibrations.

2.2.2. Modelling SSI in dynamic response

Soil-Structure Interaction (SSI) or Soil-Foundation-Structure Interaction is a concept referring to the mechanical processes arising when the structure or system is impacted by the deformability of the soil [2]. The Eurocode model disregards any effects of this interaction between the foundation and the structure, while inertial displacements and rotations can be a significant source of flexibility and energy dissipation in the soil-structure system[23]. To include SSI in model calculations, two principal methods exist: the direct analysis and the substructure approach [5] [23]. In the direct analysis, the soil and structure are included in the same model and analysed as a complete system. Often, it consists of a Finite Element (FE) or Boundary Element (BE) formulation of the system. In the substructure approach, the soil and the structure will be modelled separately and then combined to formulate the complete solution. Here, the flexibility of the soil is represented by local springs and dashpots (see figure 2.7). These springs and dashpots can be frequency dependent or independent [32].

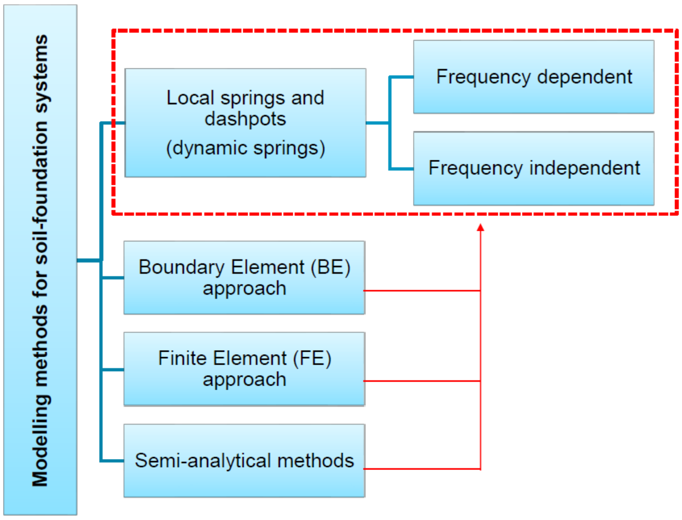

Figure 2.7: Methods for modelling SSI [32]

2.2.3. Modification of damping for SSI in Seismic-Induced Vibrations

For earthquake excitations, the National Institute of Standards and Technology (NIST) in the United States prescribes a modelling procedure based on the substructure approach that includes SSI through rotational and translational springs [23]. To include base moments, the Eurocode SDOF model is modified to an SDOF stick model. The model is depicted in figure 2.8.

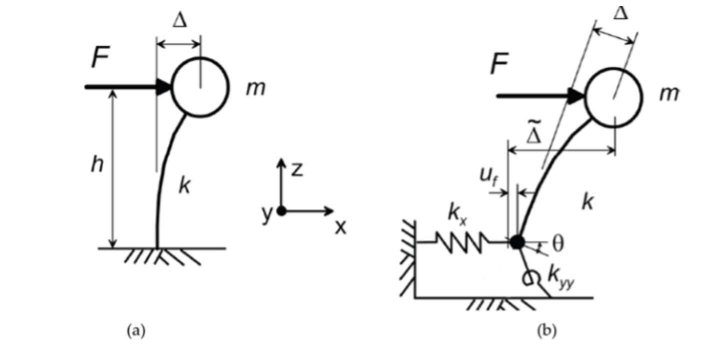

Figure 2.8: Schematic of deflections caused by a force in the case of (a) a fixed-base structure, and (b) a structure with a flexibility and damping at the base by [23].

figure 2.8 shows an SDOF stick model on a *fixed base* in (a), meaning a combination of a rigid foundation elements on a rigid base, and a *flexible base* in (b), meaning that the analysis considers the compliance (i.e., deformability) of both the foundation elements and the soil. It is important to consider this difference, as a flexible base introduces a period lengthening, which is an increase in the natural period of a system [23] [26]. The period lengthening is defined as $\frac{\tilde{T}}{T}$ and related the stiffness of the foundation to the stiffness of the structure. Veletsos and Meek [33] defined the period lengthening for the model in figure 2.8 as:

$$\frac{\tilde{T}}{T} = \sqrt{1 + \frac{k}{k_x} + \frac{kh^2}{k_{yy}}} \tag{2.1}$$

where:

T = Fundamental period of fixed base structure
$\tilde{T}$ = Fundamental period of flexible base structure
k = damage level
k_x = translational stiffness
k_{yy} = rotational stiffness
h = effective modal height (= height of center of mass of first mode)

The importance of the period lenghtening parameter has been described by Wolf (1995) [35], who derived an equation for the modification of the overall damping ratio of the fundamental mode, based on this parameter:

$$\zeta_0 = \zeta_f + \frac{1}{\frac{\tilde{T}}{T}^n}\zeta_b \tag{2.2}$$

where:

ζ_0 = Overall damping of the flexible-base system
ζ_f = Foundation damping
ζ_b = Building damping
n = taken as 3 for linearly viscous structural damping and 2 otherwise
$\frac{\tilde{T}}{T}$ = period lengthening

This relation defines how much the overall damping of the model is affected by the flexibility of the foundation and is used to modify the modal damping ratio used to calculate the response of buildings to seismic excitation [23].

2.2.4. Relevance of damping modification for SSI-effects

In the context of earthquake induced vibrations, Cruz and Miranda [9] have shown how important SSI is when it comes to the overall damping ratio. They suggested that the decrease of damping ratio with increasing building height is mainly due to SSI, as model calculations closely follow the trend of empirical data (see figure figure 2.10). In addition, Cruz and Miranda [8] showed through a parametric study how SSI-effects can either increase or reduce the effective modal damping ratio of the fundamental period. Meaning that the overall damping ratio could turn out to be lower than the structural damping, simply due to SSI. An experimental study by Vivek and Raychowdhury (2017) [34] showed a linear correlation between the period elongation and overall damping ratio for two small scale steel building models on various flexible foundation types, ranging from loose sand to dense sand. These relationships are shown in figure 2.9.

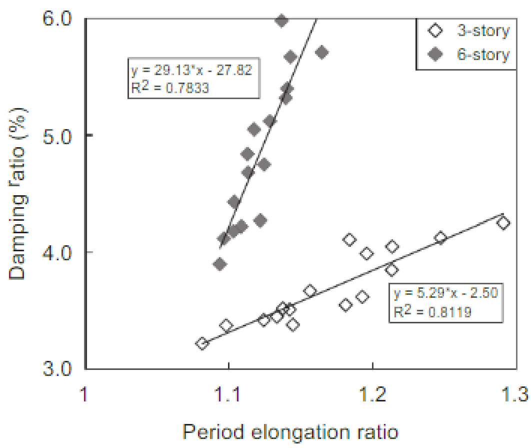

Figure 2.9: Relationship between damping and period elongation ofstructure–foundation systems [34]

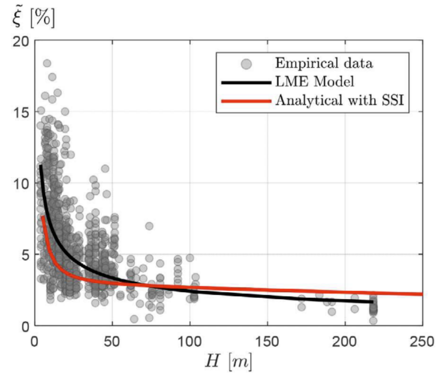

(a) Variation of the effective damping ratio of the fundamental mode with the building height and comparison with empirical data from Cruz and Miranda [9]

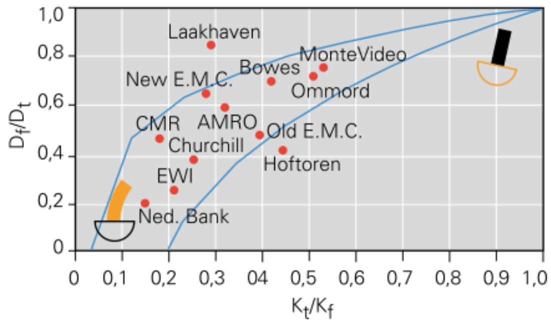

(b) Ratio of damping from foundation over total foundation (D_f/D_t against total stiffness over foundation stiffness (K_t/K_f). Taken from [3]

Figure 2.10: Several indications of the importance of SSI on damping.

2.2.5. Relevance of damping modification for wind-induced vibrations

For the case of wind-induced vibrations, Gomez et al. [26] performed model calculations and found that damping ratio is independent of structural velocity, meaning that unlike earthquake induced vibrations, wind-induced vibrations can therefore be described using linear models. In addition, Gomez et al. [26] found that for wind-induced vibrations, foundation damping is contributing as much as 50% to the overall damping, regardless of the values of the admissible parameters in his model. Other evidence of the importance of SSI, especially in the Netherlands where soft soils are predominant, was presented by Gomez [27] in another paper, where he plotted the ratio of foundation damping to total damping (D_f / D_t) against the ratio of total stiffness to foundation stiffness (K_t / K_f) for various high-rise buildings in the Netherlands (see figure 2.10). From this graph, it appeared that when the foundation stiffness is relatively high compared to the total stiffness, most damping is coming from the building instead of the foundation and vice versa. This could mean that the discrepancy found by Bronkhorst et al. [2] between predicted and measured values is caused by SSI, since Dutch buildings are often built on softer soils with low stiffness, meaning foundation damping would be higher.

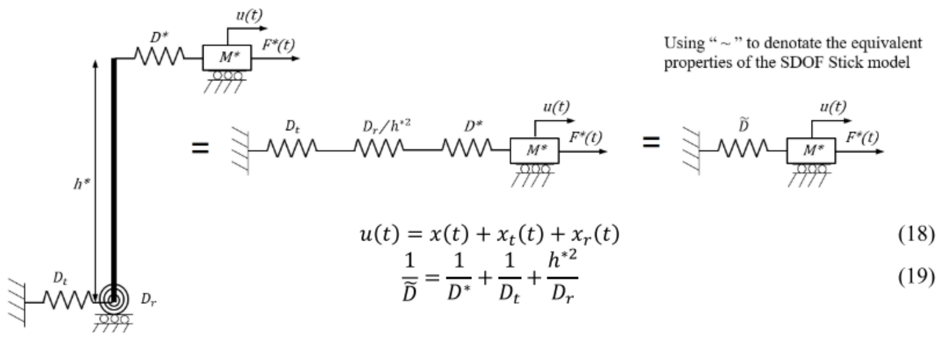

Figure 2.11: SDOF stick model by Carranza [4] and equivalent SDOF model with dynamic impedance (D_r, D_t and $D*$.

2.2.6. Applicability of modified damping ratio in wind-induced vibrations

Carranza [4] investigated the applicability of the SDOF model as proposed by the National Institute of Standards and Technology (NIST) for wind-induced vibrations. He set up a SDOF stick-model with translational and rotational dynamic impedance springs representing the soil translation and rocking motion stiffness and damping. The model can be seen in figure 2.11. In a case study, Carranza compared measurements of damping ratio of the fundamental mode of the New Orleans, a building in the Netherlands founded on soft soils, to the modified modal damping ratio determined with the SDOF stick model. The values from this model Carranza compared results for damping, natural frequency and peak accelerations found using the eurocode, numerical simulations and the SDOF stick model to the results of full-scale measurements. Table 2.2 shows the results, which suggested a much more accurate result is achieved for the overall damping ratio of the New Orleans using the SDOF stick model compared to the Eurocode model.

Model	Estimated damping ζ [%]	Error w.r.t measurement (%)
Measurements	0.842	-
HF model	0.802	- 5 %
NIST model	0.910	8%
EC model	1.6	90 %

Table 2.2: Comparison of results from [4].

2.3. Research gap: need for period lengthening estimation

As stated in the problem statement of the introduction, it is necessary to investigate the assumptions leading to the promising results by Carranza et al. [4] , Cruz and Miranda [9] and Gomez et al. [26]. Similar within these studies, is their use of a modified overall damping ratio based on the period lengthening of the buildings investigated, using equation (2.2). Despite this similarity however, all of the studies use a different approach to determine the foundation and building damping (ζ_f and ζ_b). Several different models and assumptions are behind this determination. More information on these different models and assumptions can be found in appendix A. To date, there has been no evaluation of these differing assumptions, and it remains unclear which approach yields the most accurate results for modified damping in wind-induced vibrations. It is necessary to analyze a large dataset of buildings to identify the values for ζ_f and ζ_b that result in the most accurate overall damping estimates. Therefore, the period lengthening of each of these buildings should be estimated first.

Two problems exist however, that prevent one from determining the period lengthening of buildings to investigate the damping assumptions. The first problem is that the period lengthening is a theoretical value, since only one situation, with a flexible base, exists. Therefore, it cannot be directly measured, and needs to be determined through modelling of the building in question. If the properties of the building and foundation are modelled such that they resemble the in-situ situation well enough, both the period with a flexible base and the period on a fixed base can be determined. This brings us to the second problem: lack of precise structural and foundation properties of buildings, prevent an accurate estimation of the period lengthening.

This research tries to address both problems. First, it makes use of a small scale steel model that is placed on different foundation types. Therefore, the period lengthening can be directly determined from experiments. Secondly, it proposes a methodology aimed at determining the period lengthening through model updating. Through model updating, in-situ structural and foundation properties can be estimated. The process of model updating is further explained in section 2.4.

2.4. Model updating

Model updating is a technique that has been developed to address this challenge by estimating in-situ structural properties from vibration measurements [20]. The process involves creating a structural model, typically a finite element model (FEM), and iteratively adjusting its parameters to minimize the differences between the modal properties (such as natural frequencies and mode shapes) of the model and those obtained from actual measurements. This minimization problem is typically framed as a constrained or unconstrained optimization task, with a cost or loss function representing the difference between the measured and modeled modal properties. The goal is to find the global minimum of this cost function, thereby ensuring that the model closely replicates the real-world behavior of the structure. Numerous studies have successfully applied model updating to improve the accuracy of structural models. For instance, Wu and Li [36] applied model updating to a FE model of a 310-meter-tall TV tower to create a more accurate model for assessing the wind-induced response. This was particularly important after it was observed that measured wind-induced accelerations exceeded comfort limits due to inaccurate initial estimates of the natural frequencies. Similarly, Kaynardag and Soyöz [15]

used model updating on an existing tall building's FE model to better evaluate its seismic performance. A comparable approach was undertaken by Torres et al. [31] to assess the resistance of the Cathedral of Santiago to extreme seismic loads.
In the case of Moretti et al. [20], model updating was performed using an Euler-Bernoulli beam model to determine the structural properties of the New Orleans building in Rotterdam. This approach, like others, sought to estimate the structural properties by minimizing the difference between the modal characteristics of the model and those measured on-site. The study found that the uniform beam model was effective in accurately describing up to two bending modes. However, the estimation of foundation stiffness proved more challenging, highlighting a common difficulty in model updating: while the structural properties of the building can be estimated with reasonable accuracy, foundation-related parameters are often less straightforward to quantify.

2.4.1. Model updating to estimate the period lengthening

A difficulty in determining structural properties based on measured dynamic properties arises from the fact that natural frequencies depend on the ratio of stiffness to mass. For example, in a single degree of freedom (SDOF) system, the natural frequency is given by $\omega_n = \sqrt{\frac{k}{m}}$, where k is the stiffness and m is the mass. This means that a system with a certain mass and stiffness can have the same natural frequency as another system with double the mass and double the stiffness, as long as the ratio $\frac{k}{m}$ remains the same. This interdependence creates ambiguity in isolating the exact values of mass and stiffness, especially in complex structures with multiple modes of vibration. However, period lengthening, which primarily depends on the distribution and ratio of stiffness rather than mass, can be estimated more accurately because it reflects changes in stiffness directly, making it a more reliable indicator for understanding how structural stiffness influences dynamic behavior.

3 Methodology

In this chapter, the methodology adopted to answer the research questions is presented. The chapter starts with a general description and justification of the approach applied, followed by a description of the small scale steel model and available data from the thesis by Marchelli [18]. Then, the various steps taken to use this data to update the properties of the FE model to better match the dynamic properties of the small-scale model will be described.

Model updating involves adjusting the parameters of a numerical model—in this case, a 2D FEM—to align with the measured dynamic behavior of a structure. The process comprises three main components: the collection of measurement data, the construction and refinement of the numerical model, and the application of an optimization algorithm to minimize discrepancies between the model's output and observed measurements.

For this thesis, a 2D FE model with multiple configurations was developed and updated using dynamic measurements from a small-scale steel building model previously studied by Marchelli [18]. The focus is on adjusting the model properties to capture period lengthening, a phenomenon where the fundamental period of a structure increases due to soil-structure interaction. Since period lengthening is essentially determined by the ratio of building stiffness and foundation stiffness (see section 2.2.3), this study emphasizes the identification of ratios between parameters—such as stiffness and mass—rather than the precise value of individual parameters, unlike traditional model updating research.

3.1. Experimental setup

In 2023, Marchelli [18] performed experimental modal analysis (EMA) on a small-scale steel building model (figure 3.1a). The model was lent from The Netherlands Organisation for Applied Scientific Research (TNO) and consisted of five stories with five floor plates connected by four columns at each story. The floors are connected to the columns through L-shaped steel bolted connectors (figure 3.1b).

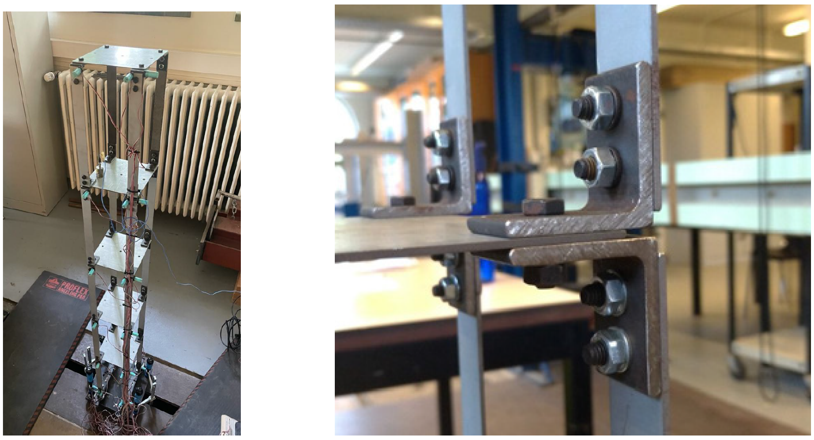

(a) Test setup **(b)** L-shaped steel connectors

Figure 3.1: Picture of the test setup and connections (taken from Marchelli's thesis [18]).

3.1.1. experimental modal analysis

Marchelli [18]studied seven different building configurations with various base conditions. The different setups (i.e., base condition/configuration combination) will be discussed in section 3.1.2. Each setup was excited with an impact hammer in both x and y directions at the top floor. The hits were placed not along the symmetry axes to allow for the identification of the torsional modes. The response of the structure was measured through twenty-five PCB 333A structural accelerometers. Three accelerometers per floor measured accelerations in the x-direction and one accelerometer per floor measured acceleration in the y-direction. On the ground floor, more accelerometers were placed, with four in both the x- and y-directions, and four additional sensors measuring accelerations in the z-direction. In figure 3.2, the placement of the accelerometers is shown.

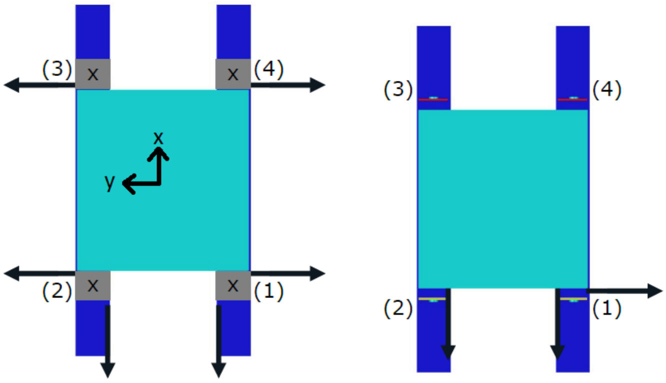

(a) Ground floor **(b)** Floor 2-5

Figure 3.2: Top view of the structure with (a) view on ground floor and (b)view on other floor levels. The location of the different sensors and their direction of measurement is clearly depicted by arrows or crosses (meaning an upward direction)

After the experiments, Marchelli [18] processed the resulting accelerations and force signals using Combined Subspace Identification as a technique of the EMAX. This way, for each of the setups, natural frequencies and modeshapes were determined. An overview of all setups can be found in appendix B. For a more extensive description of data acquisition and handling, it is recommended to consult the thesis of Marchelli [18].

3.1.2. Building configurations and base conditions

Marchelli studied seven different building configurations, each featuring a varying number of columns with different thicknesses. Specifically, some columns were 1.5 mm thick, while others were 2 mm thick. The thickness of the columns varied depending on their location within each configuration. A picture of one of these test structure configurations is shown in figure 3.1a and an overview of all column configurations is provided in figure 3.3. In this overview, the 1.5 mm thick columns are highlighted in red and the 2 mm thick columns are shown in yellow. For the configuration labeled as C7, all tests were performed twice to ensure the consistency of the experimental method. As a result, a total of 30 different setups were examined. A comprehensive list of all setups can be found in appendix B.

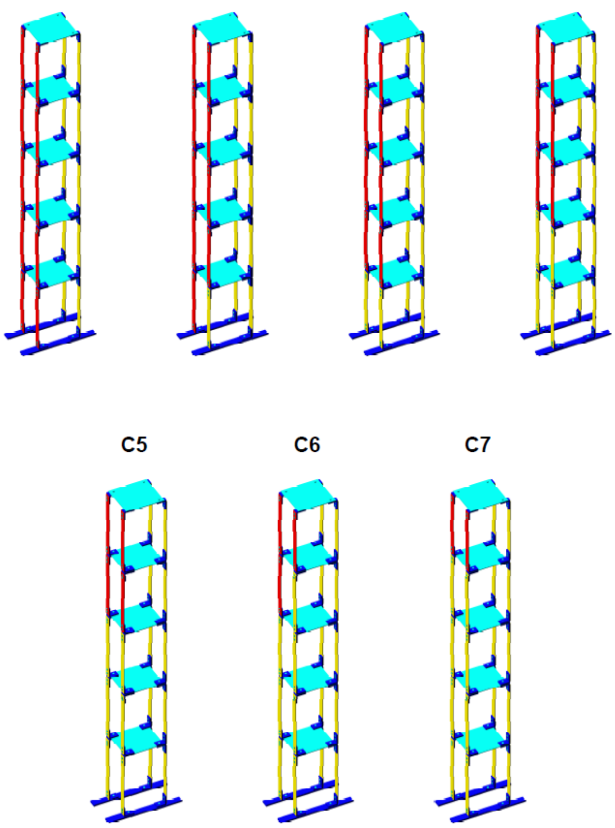

Figure 3.3: Axonometric view of configurations from C1 to C7 represented by 1.5-mm-thickness columns colored red and 2-mm-thickness columns colored yellow. Realised with AutoCAD (taken from Marchelli's thesis [18]).

For three of the configurations (C5, C6, and C7), the base conditions were also varied. Marchelli mounted them on three different types of support: (1) a thick steel plate, representing a fixed base, (2) four neoprene springs of type 4035VV25, representing a soft support, and (3) four neoprene spring of type 5020VV25, representing a stiff support. Specifics about the spring stiffness and dimensions can be found in figure 3.4.

4035VV25 - soft

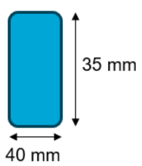

Properties soft spring		
Axial stiffness	12.7	kg/mm
Shear stiffness	2.4	kg/mm

5020VV25 - stiff

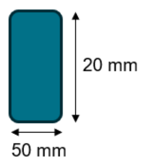

Properties stiff spring		
Axial stiffness	580	kg/mm
Shear stiffness	133	kg/mm

Figure 3.4: Dimensions and material properties of the soft and stiff springs, taken from the manufacturers' manual [7].

3.2. Development of a 2D FE model

3.2.1. Model type and dimensions

The model set up for updating based on the dynamic properties of the small-scale steel model was a 2D FE model. It was constructed in Python using the open-source PyJive library [6], developed by the Computational Mechanics group at TU Delft. The model type chosen was a 'frame model,' consisting of Timoshenko beam elements. This model type was chosen since the columns are quite thick in the strong y direction, so shear behaviour could affect the results. Each member of the model, columns, and plates were assigned dimensions corresponding to measurements and physical properties based on general properties of steel. An overview can be found in figure 3.5. Since the model was a 2D FE model, the cross-sectional area (A) was double the area of one column. The shear modulus of the steel was calculated based on the defined E-modulus using the following equation based on the Poisson's ratio of steel (ν):

$$G = \frac{E}{2(1+\nu)} \tag{3.1}$$

Since the elements of the FEM-model were Timoshenko elements, a reduction factor was used for a rectangular area, reducing the shear modulus to $0.85G$.

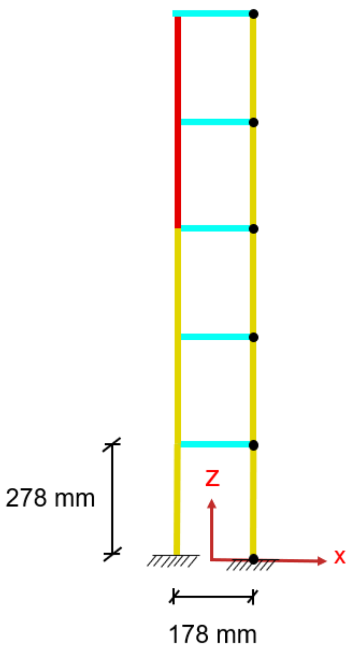

Columns 2 mm [dimensions]	
t [mm]	1.95
b [mm]	25.13
A [m²]	7.54E-05
I [m⁴]	1.41E-11

Columns 2 mm [physical properties]	
E [Pa]	210E9
ρ [kg/m²]	7840

Columns 1.5 mm [dimensions]	
t [mm]	1.56
b [mm]	25.31
A [m²]	9.8E-05
I [m⁴]	3.11E-11

Columns 1.5 mm [physical properties]	
E [Pa]	210E9
ρ [kg/m²]	7840

Floor plates [dimensions]	
t [mm]	1.95
b [mm]	150.105
A [m²]	0.000293
I [m⁴]	9.29E-11

Floor plates [physical properties]	
E [Pa]	210E9
ρ [kg/m²]	7840

Figure 3.5: Schematization of the 2D FE model used for the updating of configuration C5. Assumed dimensions, as well as initial assumed physical properties are displayed in the tables on the right. The colors of the tables correspond to the colors of the FE model on the left.

3.2.2. Connections

The columns of the steel building model were connected to the floor plates through bolted L-shaped connectors, as can be seen in figure 3.1b. In the model, the mass and stiffness added by these connectors was left out of consideration and not included. Instead, column-floor connections were assumed rigid with no rotation. Mass added by the sensors and connected wires, placed near the column/floorplate connection points, were not considered either.

3.2.3. Base conditions

The fixed base condition (steel model mounted on a thick steel plate) was modeled by assuming a clamped connection of the columns to the floor, with no rotation or displacement ($\phi(z=0)=0$, $u(z=0)=0$). For the soft and stiff base conditions, the springs were modelled by adding two members at the bottom of the FE model. The dimensions and material properties for these members were taken from the springs manufacturers' manual [7]. In the manual, axial and shear stiffness were defined in kg/mm (see figure 3.4). For the FE model, an equivalent stiffness was then calculated using the axial stiffness from the manual:

$$EA = k_{axial} l \tag{3.2}$$

where:
EA = axial rigidity of the spring [N]
k_{axial}= Axial stiffness of the spring [N/m]
l = height of spring [m]

Again, due to the reduction of dimensions from 3 to 2, only 2 members were representing 4 springs, so the cross-sectional area of the springs was doubled per member in the FEM-model. Axial stiffness of these members was calculated using equation (3.2). The shear stiffness of the steel was calculated using equation (3.3):

$$G = \frac{E}{2(1+\nu)} \tag{3.3}$$

where:
G = Shear stiffness of the spring elements [N/m]
ν= Axial stiffness of the spring elements [N/m]

A reduction factor for the area (k) of 0.85 was applied to calculate the modified shear stiffness (GA_s). A Poisson-ratio of 0.5 and a mass density (ρ) of 0 kg/m^3, to leave the mass of the springs out of consideration. In table 3.1, all material properties assigned to the spring elements in the FEM-model are depicted.

Table 3.1: Properties of Soft and Stiff Spring Elements (FEM)

	Soft Spring Elements	Stiff Spring Elements	Units
EA	8721.09	568980000	N
GA_s	2470.98	161211000	N

3.2.4. Mode matching

After performing modal analysis on the FEM-model, several modes appear with dominant vertical motion. Since only pure bending modes in x direction are considered in this thesis, the modes with dominant vertical motion should be discarded. Since this had to be done repeatedly for all building configuration in combination with different base conditions, the selection was done by calculating a displacement factor (R) of each mode using the following equation:

$$R = \frac{\sum_{i=1}^{N} dx_i^2}{\sum dy_i^2} \tag{3.4}$$

where dx_i^2 and dy_i^2 represent the displacement in x and y direction of each degree of freedom i. If $R >$ 50, the mode was identified as a bending mode with predominant horizontal displacements. The factor was determined based on visual inspection of some of the modeshapes.

3.2.5. Convergence analysis

A convergence analysis was performed based on the first four computed natural frequencies of the FE model with fixed base, to ensure that the computed natural frequencies are accurate and not dependent on the discretization level of the model. The analysis verified that the mesh is refined (i.e., as the number of elements increases) to such a level that the solution approaches a stable value. This value is stable when the difference in frequency when adding one additional node per member is less than 0.2%. In figure 3.6, the outcome for the fourth natural frequency is shown on the y-axis, against the number of elements on the x-axis. From this graph, it was concluded that 10 elements were satisfactory.

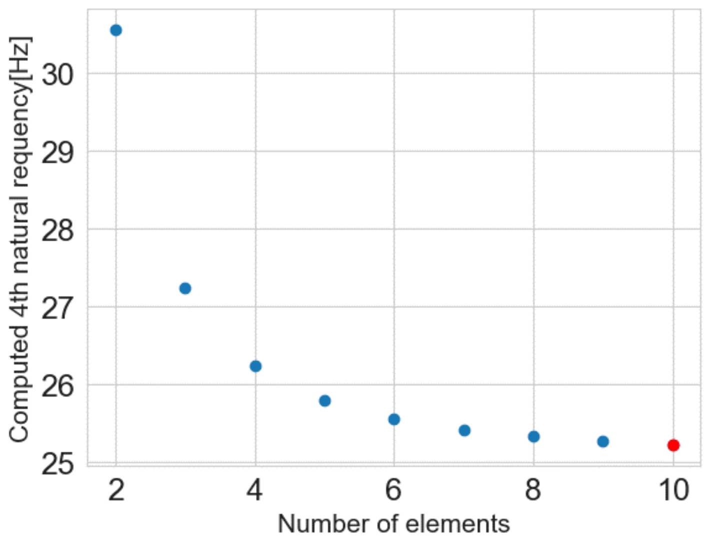

Figure 3.6: Plot showing the convergence of the fourth natural frequency against the number of elements.

3.3. Model updating

The FE model in figure 3.5 is a schematization of one building configuration, on a fixed base. In total, nine FE models were built, based on the three building configurations and three base conditions per configuration. In this study, the structural properties of the various FE models were altered through an iterative procedure for vibration-based model updating, based on a previous study by Moretti et al. [20].

3.3.1. Cost function

The model updating procedure is designed to adjust the input parameters (the structural properties assigned to the FE model) so that the computed output frequencies ($f_{n,i}$) and modeshapes ($\phi_{n,i}$) closely match the experimental natural frequencies and modeshapes determined by Marchelli [18], denoted as $\hat{f}_{n,i}$ and $\hat{\phi}_i$, where the subscript i refers to the mode number. This adjustment is achieved by minimizing the cost function J, which is defined as:

$$J = \sum_{i=1}^{N} \frac{\left| f_{n,i} - \hat{f}_{n,i} \right|}{\hat{f}_{n,i}} + \sum_{i=1}^{N} \left(1 - \text{MAC} \left(\phi_i, \hat{\phi}_i \right) \right) \tag{3.5}$$

where,

$$\text{MAC} \left(\phi_i, \hat{\phi}_i \right) = \frac{\left| \phi_i \cdot \hat{\phi}_i \right|^2}{\left(\phi_i \cdot \phi_i \right) \left(\hat{\phi}_i \cdot \hat{\phi}_i \right)} \tag{3.6}$$

This optimization process is implemented in Python. Due to the nonlinear nature of the objective function, the iterative process can converge to a local rather than the global minimum. Thus, to increase the likelihood of reaching the global minimum, multiple starting values were selected for each of the structural properties. These starting points were randomly selected by drawing samples from a uniform distribution within a specified domain. All the domain specified for the structural properties form the constrains for the optimization. Therefore, this update is called a constrained optimization. The selected structural properties, number of starting points and constraints for each of the update, are defined based on different studies that will be discussed in section 3.4.

3.3.2. Optimization algorithm

The mismatch in computed and measured dymamic properties is minimized using an optimization algorithm known as Sequential Least Squares Quadratic Programming (SLSQP). In a study by Ritfeld [24], the use of SLSQP was compared to Particle Swarm Optimization (PSO) and Differential Evolution (DE), for the model updating of a Timoshenko beam model. Ritfeld concluded that SLSQP was most effective for this type of problems. SLSQP is an individual-based optimization algorithm that uses the gradient of the objective function to guide its search within the solution space. In this process, the algorithm follows these steps:

1. Initial solution: the algorithm starts with one candidate solution.
2. Gradient evaluation: it calculates the gradient of the objective function at the current solution point.
3. Solution adjustment: based on the gradient information, the solution is adjusted to move towards minimizing the objective function.
4. Iteration: the updated solution is then evaluated, and the process is repeated until the objective function reaches its minimum or the algorithm converges.

Individual-based algorithms, like SLSQP, require fewer function evaluations than population based algorithms, making them advantageous when evaluations are computationally expensive. However, they are prone to premature convergence, particularly in complex, multidimensional problems, which can lead to suboptimal solutions [24].

3.4. Research design

To select parameters to be updated and define the settings for each of the model updating procedures, the research was divided into three main phases. These phases were designed to progressively build the framework and methodology required for the effective application of model updating. In this section, the activities in each phase and how they aim to answer to the research questions are discussed. The first two phases focused on gaining an understanding of the model behavior, identifying critical parameters, and refining the updating process. The third phase implemented the refined updating procedure across various structural configurations to validate its generalizability. In this phase, a reflection will take place by comparing obtained values for period lengthening from this procedure to experimentally obtained values.

3.4.1. Phase 1: Model Updating with Synthetic Data

In this phase, synthetic data is used to investigate and verify the model updating procedure in a controlled environment, free from real-world uncertainties. Synthetic data is generated by a reference FE model, and its dynamic properties are then used to update the structural properties of another FE model. The use of synthetic data provides an opportunity to study the model updating process in an environment without uncertainties, thereby providing a benchmark for the application using real data. Three components of the output were investigated in order to verify the correct procedure: (1) the obtained updated structural properties, (2) the dynamic properties in terms of mode shapes and natural frequencies, (3) the period lengthening values obtained. This approach helps address the first research question, 'What parameters play a large role when estimating the period lengthening of a structure by model'. It also provides insights into the optimal setup for the model updating procedure, contributing to the second research question.

Model

For this update, the FE model of configuration C5 on soft springs was used. As stated before, two models were created, the test model and the reference model. The initial values for the reference FEM parameters were based on general steel properties, as shown in figure 3.5. These base parameters represent the original properties assigned to the finite element models (FEM), and were derived from standard material properties for steel, as seen in figure 3.5. The test FE model was created by applying scalars to the structural properties of the reference FE model. These scalars, as well as initial properties of the reference and test FE model can be found in table 3.2.

	Reference model	Test model		
Parameters	**Value**	**Scalar applied**	**Value**	**Error [%]**
E_{steel} **[Pa]**	2.10E+11	1	2.10E+11	0.0
ρ **[kg/m^3]**	7850	1.5	1.18E+04	50.0
E_{spring} **[N/m]**	6.94E+06	0.8	5.55E+06	-20.0

Table 3.2: Parameter comparison between the reference model and test model. The test model was created by applying a scalar to the properties of the reference model.

Choice of Parameters to Update

The parameters selected for updating included the Young's modulus of the steel thin plates (E_{steel}), the density (ρ), and the spring stiffness (E_{spring}). These parameters were chosen based on the results of sensitivity studies, which can be found in section 4.2.

Update objectives

The FE model with the initial values corresponding to steel properties, was used as the reference model. Its dynamic pr operties (natural frequencies and modeshapes) were used as the objectives for the updating of the test FE model.

	Reference model	Test model
f_1	3.01	2.35
f_2	10.73	7.86
f_3	18.47	13.53

Table 3.3: Objectives for the update of the test FE model

Initial values and constraints

The solution space, which is defined as all possible combinations of the parameters, is constrained by setting limits for the optimization. The constraints applied during this update process are shown in table 3.6. For instance, the Young's modulus of steel, E_{steel}, had a range of [0.1, 10], meaning that the parameter value can vary up to ten times higher or lower than the initial value. It's important to note that the initial values are only used to establish the bounds for these constraints, and are not directly used as the starting point in the optimization process.

Table 3.4: Constraints for model updating parameters

Parameter	Initial value test model	Bounds	Lower Bound	Upper Bound
Young's Modulus E_{steel}	2.10E+11	[0.1, 10]	2.10E+10	2.10E+12
Density ρ	1.18E+04	[0.1, 10]	1.18E+03	1.18E+05
Spring Stiffness E_{spring}	5.55E+06	[0.1, 10]	5.55E+05	5.55E+07

Selection of starting points

The optimization algorithm (section 3.3.2) is gradient-based, meaning it may find local minima instead of the global minimum. To address this, multiple starting points within the solution space (i.e., all possible combinations of parameter values) are used. These starting points are randomly selected by drawing samples from a uniform distribution based on the defined constraints. After the starting points have been selected, these are individually updated, based on the gradient of the cost function, as described in section 3.3.

3.4.2. Phase 2: Model Updating with vibration measurements

In the second phase, the dynamic properties of the small-scale steel model, as determined from experiments by Marchelli [18], were used as objectives for the model updating procedure. This is done to compare results of updating with experimental data as input to results from updating where synthetic data was used as input.

Model

For this update, the FE model of configuration C5 on soft springs was used again.

Choice of Parameters to Update

The parameters selected for updating included the Young's modulus of the thin steel members (E_{steel}), the density (ρ), and the spring stiffness (E_{spring}). These parameters were chosen based on the results of sensitivity studies, which can be found in section 4.2. They are the same as the parameters in phase 1.

Update objectives

For this phase, the objectives for the update were experimental and consisted of three mode shapes and natural frequencies that were identified from experiments by Marchelli [18]. Specifically, the data of experimental setup 19 was used, corresponding to small-scale steel model configuration 5 on soft springs. The natural frequencies from this experiment can be found in section 3.4.2.

	Reference model
f_1	3.33
f_2	12.05
f_3	20.45

Table 3.5: Objectives for the update of the test FE model

Initial values and constraints

The solution space, defined as all possible combinations of the parameters, is constrained by setting limits for the optimization. The constraints applied during this update process are shown in table 3.6. It's important to note that the initial values are only used to establish the bounds for these constraints, and are not directly used as the starting point in the optimization process.

Table 3.6: Constraints for model updating parameters

Parameter	**Initial value FE model**	**Bounds**	**Lower Bound**	**Upper Bound**
Young's Modulus E_{steel}	2.10E+11	[0.1, 10]	2.10E+10	2.10E+12
Density ρ	7840	[0.1, 10]	784	78400
Spring Stiffness E_{spring}	6.90E+04	[0.1, 10]	6.90E+03	6.90E+05

Selection of starting points

The optimization algorithm (section 3.3.2) is gradient-based, meaning it may find local minima instead of the global minimum. To address this, multiple starting points within the solution space (i.e., all possible combinations of parameter values) are used. These starting points are randomly selected by drawing samples from a uniform distribution based on the defined constraints. After the starting points have been selected, these are individually updated, based on the gradient of the cost function, as described in section 3.3

Phase 3: Comparison with Experimental Data

In the final phase, the updating procedure was adjusted based on the findings of the first two phases, and then will be applied to all configurations and base conditions. The goal of this phase is to address research question 3 *How well do period lengthening values computed through model updating of a 2D FE model align with experimental values?*

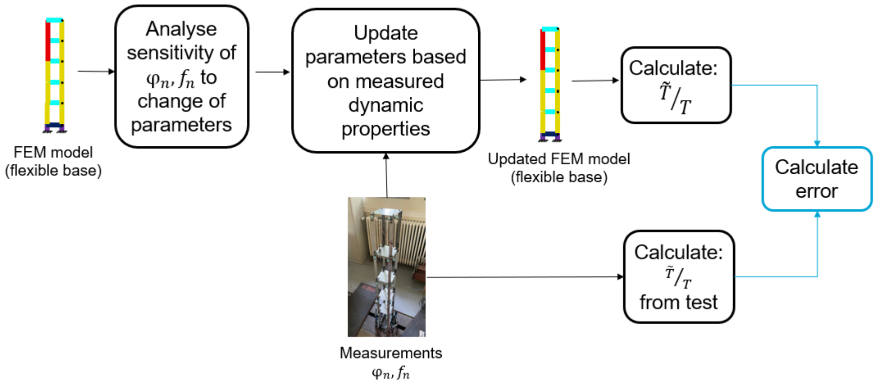

Figure 3.7: Overview of the updating procedure, which updates all mass and stiffness parameters at once.

The computed period lengthening values are compared with experimental results to evaluate the method's accuracy and reliability. This phase provides a validation of the entire model updating process, allowing for a final comparison between the model's outputs and real-world observations. A reflection will be made on the potential of the model updating method to determine the period lengthening.

Data used

For the model updating procedure, only the setups with configuration C5, C6 or C7 that were excitated in x direction by the impact hammer were used for this thesis, since only these configurations were tested under different base conditions and since the FEM-model set up for this thesis only describes bending modes in x direction. An overview of the several setups of which the data was used in this thesis can be found in table 3.7.

Table 3.7: Setups with excitation in x-direction. The modal data obtained from the EMA by Marchelli [18] was directly used in this thesis as input for the model updating procedure explained in section 3.3.

	Foundation condition		
Configuration	Fixed	Soft	Stiff
C5	09	19	27
C6	11	17	25
C7	13	16	23

4

Properties of the FE model

This chapter presents the dynamic properties of the FE model that was set up. For brevity, only the dynamic properties of the FE model representing configuration 5 is discussed. A comparison will be made to the dynamic properties and period lengthening from measurements, providing insights into the model's accuracy before the updating procedure. In addition, a sensitivity analysis is presented that investigates the influence of different parameters on the dynamic properties. These sensitivity analyses are necessary to determine which parameters are chosen to be updated and will help to understand the outcome of the updating pocedure.

4.1. Dynamic properties FEM-model

Through modal analysis, the dynamic properties of the 2D FEM-model used to model the small-scale steel model could be determined. Both the natural frequencies and the modeshapes were determined, for configuration C5 till C7 on all foundation types. In appendix D.1.3, two examples are displayed of modeshapes determined with the FE model with initial parameters.

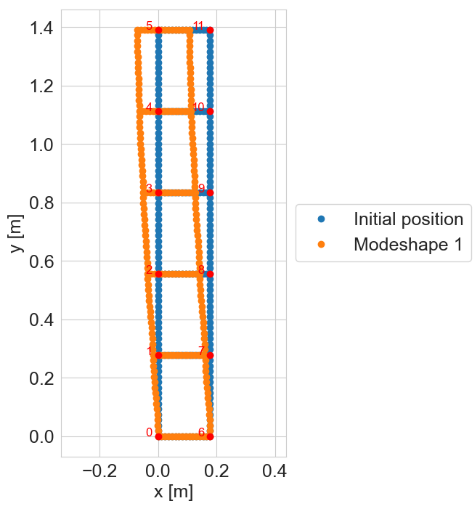

(a) Modeshape of configuration 5 on a fixed base, computed by the FE model

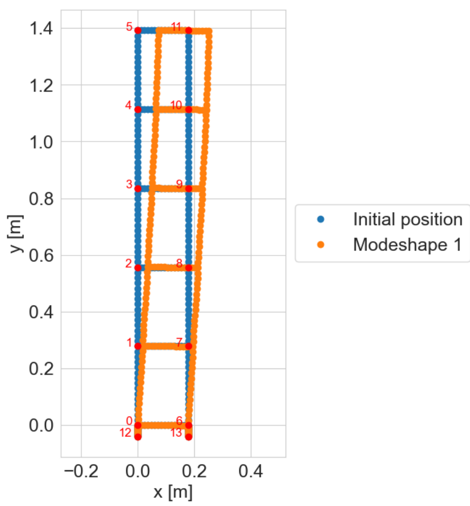

(b) Modeshape of configuration 5 on a soft base, computed by the FE model

Figure 4.1: Modeshapes computed by the FE model containing all displacements of all nodes.

4.1.1. Natural frequencies before update

In table 4.1, the first three natural frequencies are displayed for building C5 on different base conditions. These frequencies are compared to the measured natural frequencies from the experiments form Marchelli [18]. It can be seen that most frequencies are off with about 10 %. This could be because of the simplifications that have been assumed when setting up the FE model. For example, additional mass and stiffness from corner connectors, sensors and wires are ignored. Furthermore, the 2D approximation of the 3D structure might also have an effect.

	Fixed base			**Stiff Spring**			**Soft Spring**		
	Numerical Result (FEM)	**Test Result**	**Error**	**Numerical Result (FEM)**	**Test Result**	**Error**	**Numerical Result (FEM)**	**Test Result**	**Error**
f_1	3.85	4.35	-11.5%	3.85	4.25	-9.41%	3.09	3.33	-7.21%
f_2	10.91	12.39	-11.9%	10.91	12.33	-11.52%	10.70	12.05	-11.20%
f_3	18.73	20.92	-10.5%	18.73	20.79	-9.91%	18.41	20.45	-9.98%

Table 4.1: Natural frequencies of configuration 5 computed by the FE model compared to natural frequencies determined by experiments of Marchelli (2023)[18]

In section 4.1.1, a comparison is made between the natural frequencies of configuration 5 on a fixed base with results from a similar 2D model Marchelli updated in her thesis. Important to point out is that the 2D FE model by Marchelli is based on a fixed base condition, and she assumed infinitely stiff floor plates, while in the 2D FE model of this thesis, these floor plates were assigned general properties of steel (see section 3.2).

	FE model	**Thesis Eliza**	**Difference [%]**
f_1	3.85	3.677	4.49%
f_2	10.91	10.834	0.70%
f_3	18.73	17.335	7.44%

Table 4.2: Comparison between natural frequencies from the FE model and natural frequencies obtained from the 2D shear model from the thesis of Eliza, along with the percentage differences.

4.1.2. Mode shapes before update

From the FE model, the mode shapes can be obtained. These mode shapes consist of three times the amount of nodes, since three degrees of freedom per node are defined (x displacement, z displacement, and rotation). The mode shapes in figure D.6 contains lots of nodes (10 per member). The experimental mode shapes that were determined however, do not contain that much information, since they were determined from the sensors, which provide limited displacement information. For example, the sensor at each of the floor plates measured only horizontal displacement (with the exception of the base sensor, which also measured horizontal displacement). Therefore, the experimental mode shapes contained only 7 degrees of freedom. For the update procedure, this meant only 7 DOF's could be compared. For the comparison, only 6 horizontal displacements and 1 vertical displacement were taken from the numerically computed mode shapes. These displacements corresponded to the nodes at the sensor heights.

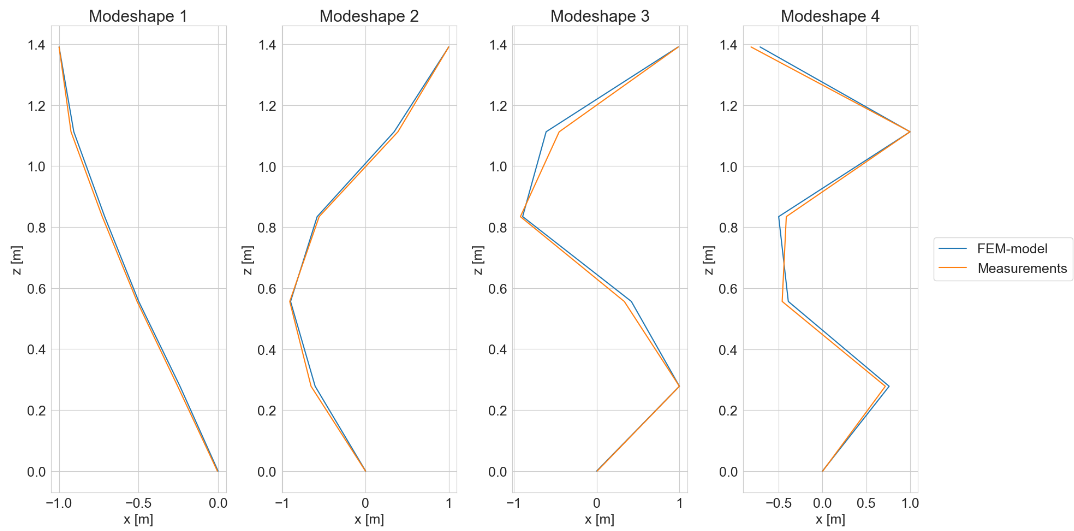

Figure 4.2: First four modes plotted for configuration 5 with a fixed boundary condition at the bottom. The orange line shows the mode shapes resulting from OMA performed in the thesis of Marchelli, while the blue line represents the mode shapes computed by the FE model. However, only the horizontal displacements at the heights of the sensors are extracted from the FEM-calculation.

In figure 4.2, the first four mode shapes of configuration 5 on a fixed foundation are displayed. Even before updating, there is already a strong alignment between the experimental and FE model mode shapes. This is further supported by the Modal Assurance Criterion (MAC). As shown in figure 4.3, the MAC values for the first four modes of C5 were computed to compare the experimental data to the FE model results. Across all base conditions, the MAC values are very high, indicating an excellent match between the experimental measurements and the model predictions.

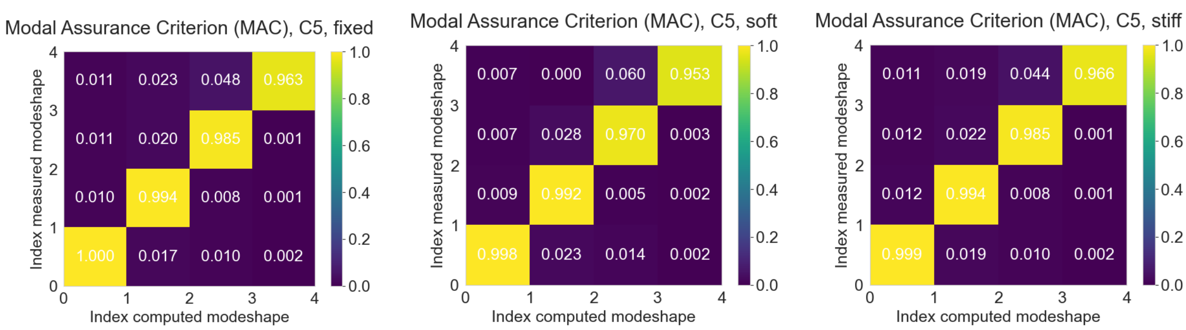

(a) MAC values for C5 on a fixed foundation **(b)** MAC values for C5 on a soft foundation **(c)** Plot 3

Figure 4.3: MAC values for C5 on a stiff foundation

4.1.3. Period lengthening before update

Both the experimental and modeled period lengthening were determined for each configuration under two base conditions: stiff springs and soft springs. Table 4.3 presents the period lengthening values obtained from the tests performed by Marchelli's, alongside those computed using the non-updated FE model, as well as the corresponding percentage error. It appears that the FE model captures the period lengthening reasonably well already. However, there are a few reasons why an update is necessary for updating. Firstly, the aim is to estimate the period lengthening under conditions of high parameter uncertainty. In this case, the parameter uncertainty is relatively small, which is why the discrepancies between the model and experimental results are minor. For real buildings, which are composed of more complex materials and structures, this level of certainty is rarely achievable. Additionally, period lengthening is a highly sensitive parameter, typically falling within a narrow range (between 1 and 2). As such, an error of 5% can be considered significant. An objective of this thesis is to explore whether accurate estimates of period lengthening can still be made under greater uncertainty in the parameters.

	Stiff spring			Soft spring		
Configurations	**Period lengthening (FEM)**	**Period lengthening (Test)**	**Error**	**Period lengthening (FEM)**	**Period lengthening (Test)**	**Error**
C5	1.00003	1.02376	-2.32	1.24442	1.30568	-4.69
C6	1.00003	1.02205	-2.15	1.24667	1.31103	-4.91
C7	1.00003	1.02026	-1.98	1.24956	1.31460	-4.95

Table 4.3: Experimental and FE model period lengthening values, along with the percentage error, for stiff and soft spring base conditions.

4.1.4. Conclusion on properties FE model before update

In conclusion, the initial evaluation of the dynamic properties of the FE model for configuration 5 demonstrates that, while the model captures the general behavior of the system, there are discrepancies between the FE results and the experimental measurements, particularly in terms of natural frequencies and period lengthening. The simplifications in the FE model, such as ignoring additional mass and stiffness contributions, likely contribute to these differences. However, the mode shapes show a strong alignment with the experimental data, as indicated by the high MAC values, suggesting that the model structure is accurate enough.

4.2. Sensitivity analysis

To identify which input parameters required updating, a sensitivity analysis was conducted on the dynamic properties of the FE model, which depend on mass and stiffness. The analysis focused on the influence of mass density (ρ), E-modulus (E), and modified shear modulus (kG). Initially, standard values for steel were used. These values can be found in figure 3.5 in the methodology chapter.

4.2.1. Sensitivity fixed base model

The sensitivity analysis was performed in two stages. The first one looks at the sensitivity of the dynamic properties (mode shapes and natural frequencies) to changes in structural properties. The parameters investigated were ρ_{steel}, E_{steel}, E_{spring} and ν (since the shear stiffness is calculated using equation (3.2)). Each parameter was individually varied for all members to evaluate the impact on the natural frequencies and mode shapes.

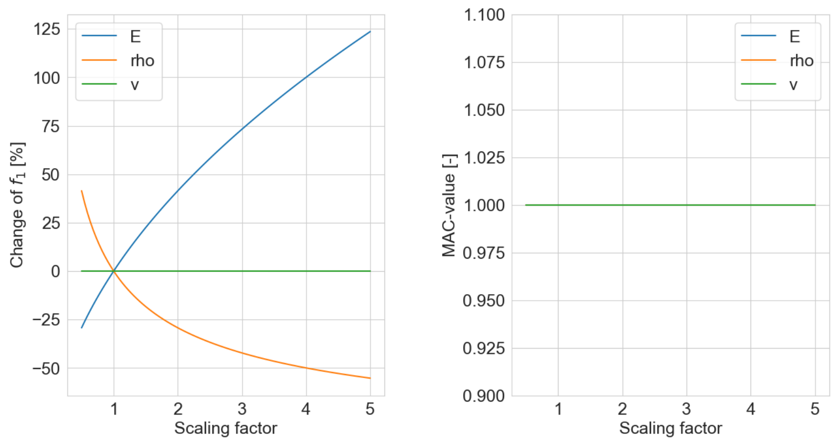

Figure 4.4: Percentual change in the first natural frequency, f_1, as a function of scaling the parameters E, ρ, and ν individually. The x-axis represents the scaling factor applied to each parameter, while the y-axis indicates the corresponding percentage change in f_1. The results for the second and third natural frequencies, f_2 and f_3, show similar trends, and therefore only the graph for f_1 is presented.

In figure D.2, the sensitivity of the first mode's natural frequency and mode shape to changes in Young's modulus (E_{steel}), mass density (ρ), and Poisson's ratio (ν) is shown. For these graphs, a fixed base condition was assumed. It demonstrates how the natural frequency is affected by the stiffness (E_{steel}) and mass (ρ) of the steel, which are the most important parameters defining the dynamic properties. In contrast, the graph shows that the Poisson's ratio (ν) has a negligible effect on the natural frequency, probably since the thin beams and columns mainly show bending behaviour. The graph only shows the effect on the first mode for brevity, since the second and third mode show exactly the same dependencies.

In contrast to the frequencies, the MAC value of the first mode (as well as the second and third modes) is not affected by changes in these parameters. This is because, when a scaling factor is applied to the stiffness, the increased stiffness is uniformly distributed over the height of the structure, resulting in no change in the mode shape. Only when local changes in stiffness or mass are applied will the mode shape be affected.

4.2.2. Sensitivity flexible base model

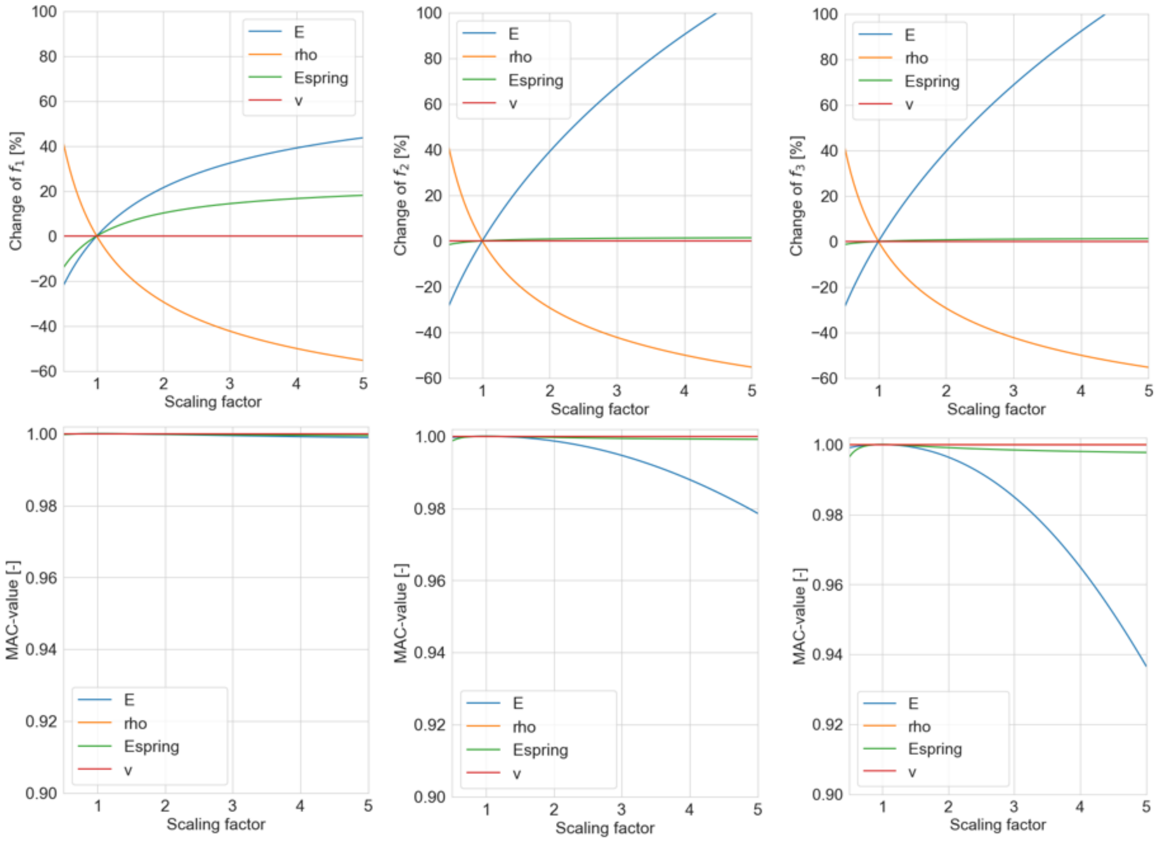

Figure 4.5: Percentual change of the natural frequencies, f_n, as a function of scaling the structural properties E_{steel}, E_{spring}, ρ, and ν. The x-axis represents the scaling factor applied to each parameter, while the y-axis indicates the corresponding percentage change in f_n.

In figure 4.5, the change of the natural frequencies and MAC due to variation in the structural properties is shown again, but now for the case of the small-scale steel model on soft springs. In these graphs, the influence of variety in the spring's E-modulus (E_{spring}) is also depicted. A few things are interesting to mention. The effect of the added spring stiffness mostly has an effect on the first natural frequency: this frequency is now affected by a combination of E_{steel} and E_{spring}. This is important, since the first natural frequency is directly determining the period lengthening. For higher modes, the influence of E_{spring} is low to negligible. The dependency of these natural frequencies does not change much compared to the fixed base situation, and mainly depend on the contribution of E_{steel} and ρ.

Since the stiffness of the springs now introduces a localized change in stiffness, the modeshapes are now affected by the variation of the structural properties. The higher the modes, the more effect can be seen from the parameters. Variation in E_{steel} has the largest effect. A variation of E_{spring} has very little effect. The MAC is not affected by the choice for ρ, since no relative change in ρ is applied.

5

Model updating using synthetic data

This chapter presents the results of the model updating approach with synthetic data as input. Synthetic data means that the output of a reference FE model (in terms of dynamic properties) was used to update the structural parameters of another FE model. A study with synthetic data provides insight into the way the updating code operates under conditions where there is no model error. In addition, it verifies that the code works properly, if it is able to obtain the structural and dynamical properties of the reference model. The study was performed for configuration 5 on both soft and stiff springs. The results for both of these base conditions will be discussed and compared. The chapter has been divided into three main components, that were investigated in order to verify the correct procedure. Section 5.2 will discuss the dynamic properties in terms of mode shapes and natural frequencies, while section 5.3 will focus on the updated structural properties. Finally, section 5.3.3 will examine the period lengthening values obtained.

5.1. Study overview

An overview of the update is shown in figure 5.1. Two updates were carried out, both using configuration 5, but with the structure placed on either soft or stiff springs. The results from the configurations with both of these base conditions will be presented and compared in this chapter.

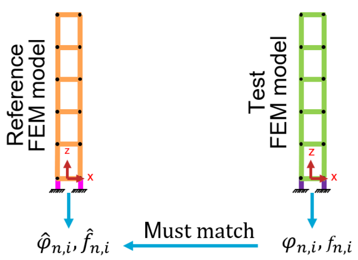

Configuration	C5, flexible base C5, stiff base
Parameters updated	E_{steel}, ρ_{steel}, E_{spring}
Bounds (equal for each parameter)	[0.1, 10]
Objective	3 $\hat{f}_{n,i}$ =[3.09, 10.73, 18.47] 3 $\hat{\varphi}_{n,i}$
Starting values	100, random

Figure 5.1: Overview of the update settings for the update with synthetic data. E, ρ, and E_{spring} of the test FE model of configuration 5 were updated using the procedure explained in section 3.3. To account for the nonlinearity of the cost function in equation (3.5), 100 starting points were randomly selected from a uniform distribution for the test model, within the specified bounds.

5.2. Results - Dynamic properties

This section presents a detailed comparison of the dynamic properties before and after the model update, specifically focusing on the natural frequencies and MAC values. The comparison is performed for the configuration on both stiff and soft springs. First, the solution with the lowest cost function is discussed to demonstrate the effectiveness of the model updating process. Subsequently, the errors across various solutions are discussed. This broader analysis is necessary because the optimization process may converge to different solutions depending on starting points, local minima, or constraints encountered during the iterations. Studying the distribution of errors provides insights into the consistency and robustness of the optimization process, revealing any systematic trends or challenges in accurately capturing the system's dynamic behavior.

5.2.1. Optimal solution

In table 5.1 and table 5.2, an overview of the dynamic properties of the system before and after the update are presented for the configuration on soft and stiff springs respectively. The table lists the natural frequencies and Modal Assurance Criteria (MAC) values corresponding to the solution with the lowest cost function. The lowest cost function had a value of 3.72e-06 for the soft springs case and 1.47e-06 for the stiff springs case. Values for the first three modes for both the reference and test models are compared.

For the soft spring situation, table 5.1 shows that after the update, the errors are reduced to zero for all dynamic properties, indicating a successful execution of the updating code.

For the stiff spring situation, table 5.2 shows that after the update, the errors are also reduced almost to zero for all natural frequencies. However, the error in the first natural frequency is slightly higher than the error in other natural frequencies.

With regard to the MAC values, it can be seen in table 5.2 that the MAC before the update was already equal to 1 for the stiff spring case. Apparently, the MAC is very insensitive to a change of $E_{springs}$ when the spring stiffness is already high.

	Reference model	Test model (before update)	Test model (after update)	Error before update[%]	Error after update[%]
fn [Hz]	3.01	2.35	3.01	-21.9	0.0
	10.73	7.86	10.73	-26.7	0.0
	18.47	13.53	18.47	-26.7	0.0
MAC [-]	1	0.99998	1	0.0019	0.0
	1	0.99995	1	0.0051	0.0
	1	0.99987	1	0.0134	0.0

Table 5.1: Comparison of natural frequencies (fn) and MAC values between the reference model, test model (before and after update), and the percentage errors before and after the update.The table shows the solution with the lowest cost function for the configuration mounted to soft springs.

	Reference model	Test model (before update)	Test model (after update)	Error before update[%]	Error after update[%]
fn [Hz]	3.86	2.81	3.86	-27.20	0.00011
	10.94	7.98	10.94	-27.06	0.000008
	18.79	13.73	18.79	-33.96	-0.000029
MAC [-]	1	1	1	0.0	0.0
	1	1	1	0.0	0.0
	1	1	1	0.0	0.0

Table 5.2: Comparison of natural frequencies (fn) and MAC values between the reference model, test model (before and after update), and the percentage errors before and after the update. The table shows the solution with the lowest cost function for the configuration mounted to stiff springs.

5.2.2. Errors in estimated natural frequencies

Not all solutions generated by the algorithm represent optimal or correct outcomes. This can occur for several reasons: the algorithm may converge to a local minimum, it may terminate upon reaching a boundary constraint or it may halt after exceeding the maximum number of iterations. Therefore, it is helpful to look at the distribution of errors. This analysis provides valuable insight into the overall effectiveness of the optimization procedure in achieving its intended objectives.

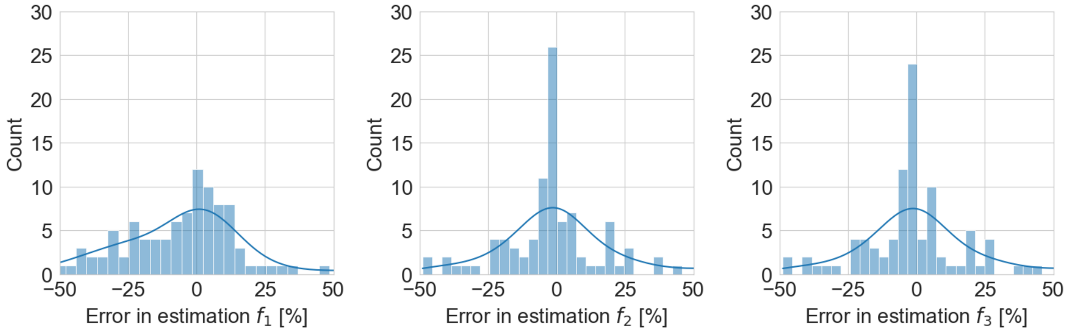

(a) Error distribution for the first three natural frequencies for the soft spring case..

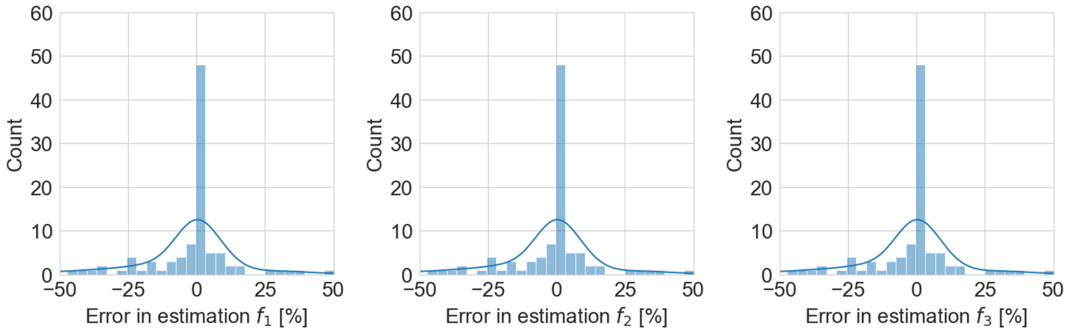

(b) Error distribution for the first three natural frequencies for the stiff spring case.

Figure 5.2: Errors in estimation natural frequencies. Each histograms shows the distribution of errors across 100 obtained solutions.

Figure 5.2a and figure 5.2b show the error distribution of the solutions' natural frequencies compared to the reference model.

For the soft spring case in figure 5.2a, most errors are low for the second and third natural frequencies: a large peak at zero error can be seen. For the first natural frequency however, the error is generally higher. Of all solutions, the percentage with an estimated first natural frequency with an error below 1% was 7%, whereas this percentage was 21% and 19% respectively for the second and third natural frequency. It could be that a correct E_{steel}/ρ leads to low errors in the second and third natural frequency, but that the parameter $E_{springs}$, which has a more significant influence on the first natural frequency (see section 4.2.1), is estimated correctly for less cases, causing higher errors. This is supported by figure 5.3, where a correlation is shown between the error of the first natural frequency and the value of the E_{steel}/E_{spring} ratio. In this graph, we see that even for solutions with a high error in this ratio, the second and third natural frequencies are generally not affected. The dots in this plot that are located off the line are affected by the value of the E_{steel}/ρ ratio.

For the stiff spring case, a different behavior can be observed compared to the update with soft springs. Figure 5.2b shows the error distribution for the first three natural frequencies obtained from 100 starting points for the stiff spring case. All three histograms in this figure are nearly identical, indicating that in this case for the optimization algoritm it is not harder to estimate the first natural freqeuncy correctly. Specifically, for all of the three natural frequencies, 44% of the solutions had errors within 1% from the frequencies of the reference model.

SinceFigure 5.2a and figure 5.2b do not provide insight in the errors obtained within one solution, two plots were made that connect the errors obtained for the first three natural frequencies within one solution. Figure 5.4a and Figure 5.4b show the results in terms of error of the natural frequencies per solution, for configuration 5 on soft and stiff springs respectively. For each solution, the errors of the

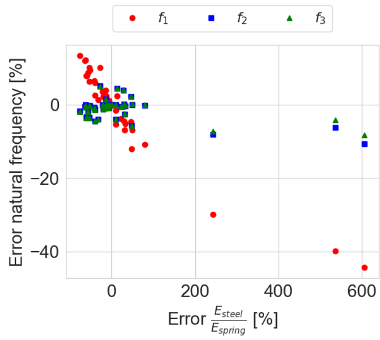

Figure 5.3: Errors in the natural frequencies obtained plotted against the error in ratio of E_{steel}/E_{spring}.

three corresponding frequencies are connected. In figure 5.4a, for the configuration on soft springs, it can be seen that the lines connecting the second and third natural frequencies are almost entirely horizontal, but the line connecting the first natural frequency has a different slope. This is caused by the fact that the second and third natural frequencies are equally affected by the E_{steel}/ρ ratio, but the first natural frequency is also affected by the E_{steel}/E_{spring} ratio. In figure 5.4b, for the configuration on stiff springs, again a clear difference can be seen. In contrast to the soft spring case, the errors for all natural frequencies in a given solution are now nearly equal, as indicated by the almost horizontal lines. This confirms that the influence of the E_{steel}/E_{spring} ratio is minimal when the springs are very stiff, since in the sensitivity study and the update of the soft spring case, it was concluded that the E_{spring} parameter was mainly affecting the first natural frequency. Therefore, the system's frequencies — and their errors — are now being primarily governed by the E_{steel}/ρ ratio.

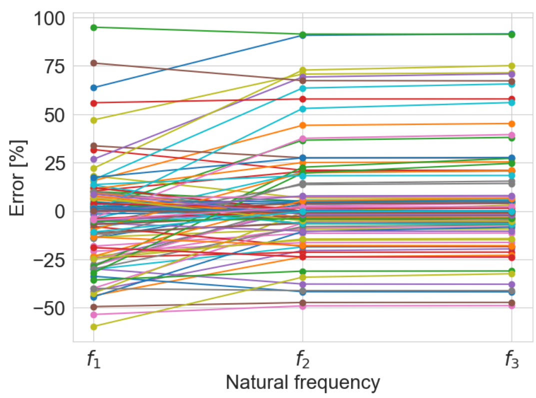

(a) Errors in natural frequencies obtained. The connected dots together represent a solution.

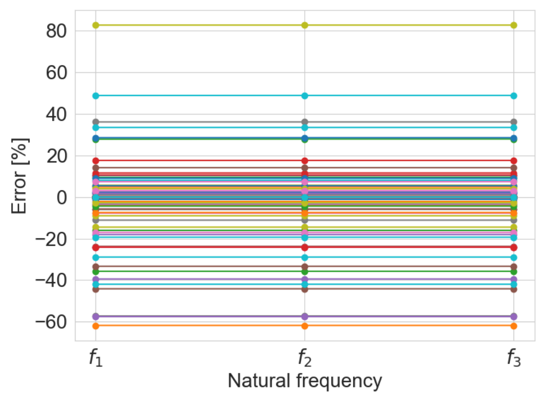

(b) Errors in the first three natural frequencies for the update of the stiff spring case.

Figure 5.4: Errors in natural frequencies across solutions for configuration 5 on soft base (a) and stiff base (b).

5.2.3. Errors in modeshapes

For the configuration on soft springs, figure 5.5a presents three histograms showing the distribution of MAC values for the first three modes across 100 solutions obtained. It can be seen that the error in MAC value is generally higher for higher modes. In the sensitivity study (figure 4.5), we saw that mode shapes are not dependent on the mass density (ρ), and E_{steel} and E_{spring} have more effect on higher modes. This could explain why the error in MAC value is generally higher for higher modes. This is also supported by figure 5.6. In this graph, the error in E_{steel}/E_{spring} ratio is plotted against the MAC-value of each of the 100 solutions of the soft springs case. Since the update was performed using synthetic data as input, the error in estimated E_{steel}/E_{spring} ratio was known. Figure 5.6 shows that an error of the E_{steel}/E_{spring} ratio clearly leads to larger errors in higher modes. In addition, it is clear that the MAC values are not affected by the mass density (ρ), since in that case there would be points located above other points.

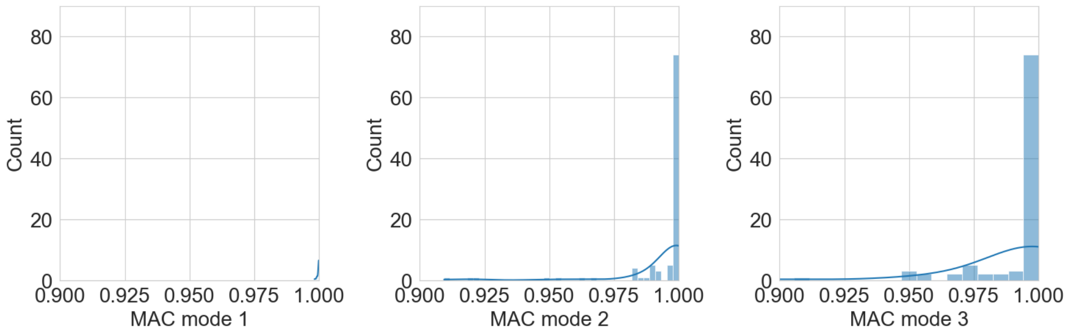

(a) MAC values for the first three mode shapes obtained from the updating procedure compared to those of the reference model.

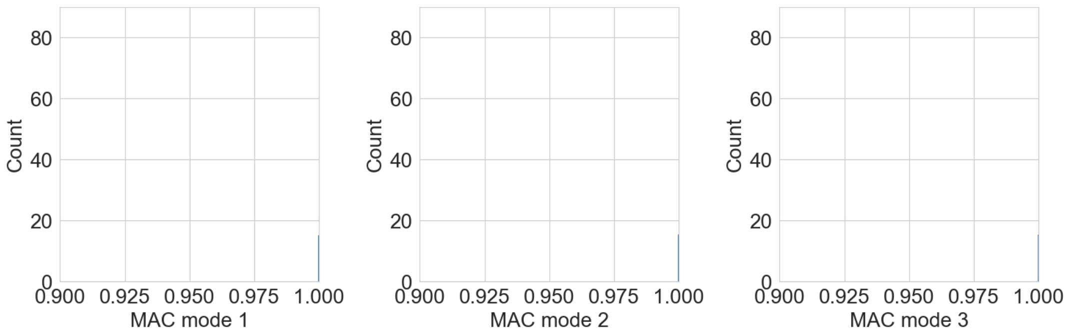

(b) MAC values for the first three mode shapes obtained from the updating procedure compared to those of the reference model.

Figure 5.5: Errors in estimation of dynamic properties for configuration 5 on a stiff base, updated with measurements from Marchelli [18].

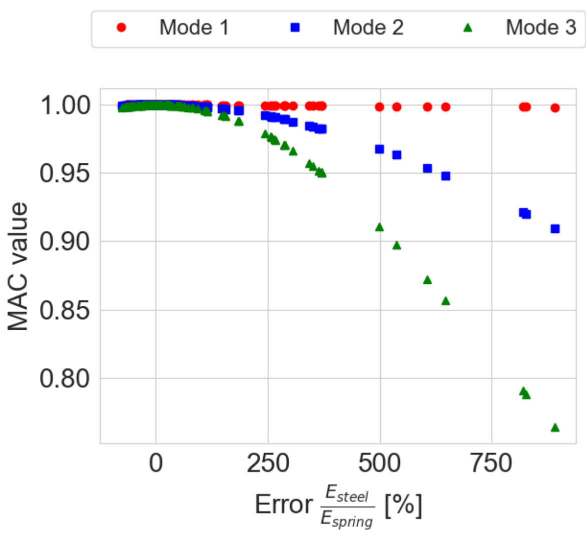

Figure 5.6: Errors in the MAC values obtained plotted against the error in ratio of E_{steel}/E_{spring}. In this graph, it can be seen that there is no influence of the E_{steel}/ρ ratio on the error of the MAC.

For the case on stiff springs, the errors are significantly lower across all modes compared to the soft spring case, as seen in figure 5.5b. In the latter, the error was generally higher for higher modes. However, with the stiff springs, the errors are low for all modes, with the lowest MAC value even being as high as 0.9999994. Apparently, the spring stiffness compared to the building stiffness (E_{steel}/E_{spring} ratio) is already so low, that a variation in $E_{steel}E_{spring}$ within the given bounds won't change the MAC.

5.3. Results - Structural properties

In this section, the obtained structural properties for the update of configuration 5 on both soft and stiff spring conditions will be discussed.

5.3.1. Optimal solution

In table 5.3 and table 5.4, the initial and updated values of three structural parameters are presented, for the soft and stiff spring respectively. The tables show the results with the lowest cost function, after running the optimization algorithm 100 times.

For the soft spring case, in table 5.3, it can be seen that all individual structural parameters have a large error of 200%. A derivation in appendix C, demonstrates how these ratios between dynamic properties dictate the dynamic characteristics of the system. Consequently, the optimized values obtained do not represent physical properties; rather, it is the ratios between these properties that matter (Specifically, the ratios of stiffness and mass: $\frac{E_{steel}}{\rho}$ and $\frac{E_{steel}}{E_{spring}}$). Therefore, as long as these ratios are accurately determined, the system's dynamic properties can be correctly derived, regardless of the individual values of the properties themselves. This indicates that scaling all structural properties by the same scalar leads to identical dynamic properties.

Parameters	Reference model	Test model (before update)			Test model (after update)		
	Value	Scalar applied to reference model	Value	Error [%]	Bounds for update	Updated value	Error [%]
E_{steel} [Pa]	2.10E+11	1	2.10E+11	0.00	[0.3, 3]	6.30E+11	200.00
ρ [kg/m^3]	7.85E+03	1.5	1.18E+04	50.00	[0.3, 3]	2.35E+04	200.00
E_{spring} [N/m]	6.94E+06	0.8	5.55E+06	-20.00	[0.3, 3]	2.08E+07	200.00
E_{steel}/ρ [m^2/s^2]	2.68E+07	0.67	1.80E+07	33.00	[0.1, 10]	2.68E+07	0.00
E_{steel}/E_{spring} [-]	3.03E+04	1.25	3.78E+04	25.00	[0.1, 10]	3.03E+04	0.00

Table 5.3: Parameter comparison between the reference model, test model, and optimized test model. The values of the updated test model correspond to the solution obtained with the lowest cost function. The bounds of the ratios follow from the bounds of the individual parameters.

For the stiff spring case, in table 5.4, the initial and updated values of three structural parameters are presented for the solution with the lowest cost function. In contrast to the solution with the lowest cost function obtained for the soft spring, not all parameters are estimated with a similar error. Although E_{steel} and ρ are similar with an error of 448.97% and 448.27 %, the error of E_{spring} is larger (558.22 %). This, despite the very low cost function of order 10^{-6}. When it comes to ratios, it can be seen that for the stiff spring case, only the $\frac{E_{steel}}{\rho}$ is optimized very accurately. The $\frac{E_{steel}}{E_{spring}}$ ratio however, has an error of almost 17 %. Apparently, if the springs are very stiff, it is harder to optimize the $\frac{E_{steel}}{E_{spring}}$ ratio.

Parameters	Reference model	Test model (before update)			Test model (after update)		
	Value	Scalar applied to reference model	Value	Error [%]	Bounds for update	Updated value	Error [%]
E_{steel} [Pa]	2.10E+11	1	2.10E+11	0.00	[0.1, 10]	1.15E+12	448.97
ρ [kg/m^3]	7.85E+03	1.5	1.18E+04	50.00	[0.1, 10]	4.30E+04	448.27
E_{spring} [N/m]	2.90E+11	0.8	2.90E+11	-20.00	[0.1, 10]	1.91E+12	558.22
E_{steel}/ρ [m^2/s^2]	2.68E+07	0.67	1.80E+07	33.00	[0.01, 100]	2.68E+07	0.13
E_{steel}/E_{spring} [-]	0.72	1.25	3.78E+04	25.00	[0.01, 100]	0.60	-16.59

Table 5.4: Parameter comparison between the reference model, test model, and optimized test model. The values of the updated test model correspond to the solution obtained with the lowest cost function. The bounds of the ratios follow from the bounds of the individual parameters.

5.3.2. Optimization of ratios

When investigating the ratios between structural parameters, specifically $\frac{E_{steel}}{\rho}$ and $\frac{E_{steel}}{E_{spring}}$, rather than the individual parameters, a clear convergence can be observed in the cost function. Figure 5.7 shows these ratios for both the stiff and soft spring cases, obtained across the 100 solutions. It is evident that the minimum value for the cost function decreases as the ratio approaches its optimal value.

A clear difference can be observed between the stiff and soft spring cases. For the soft spring case, both ratios appear to converge towards the optimum. However, in the stiff spring case, the system's behavior is primarily governed by the $\frac{E_{steel}}{\rho}$ ratio. As a result, the convergence for this ratio is even more pronounced, with figure 5.7c showing an almost perfect V-shaped curve. In contrast, figure 5.7d shows that for the $\frac{E_{steel}}{E_{spring}}$ ratio, the convergence is harder to discern, as the behavior is asymptotic: the E_{spring} value becomes very large, approaching a fixed base scenario.

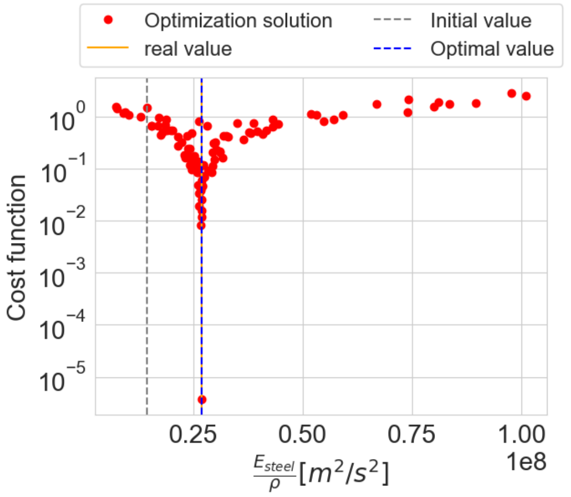

(a) Plot of the $\frac{E_{steel}}{\rho}$ ratios across the 100 solutions from the optimization algorithm. Dashed lines indicate value of the actual ratio (of the reference model) and optimal value obtained from the optimization.

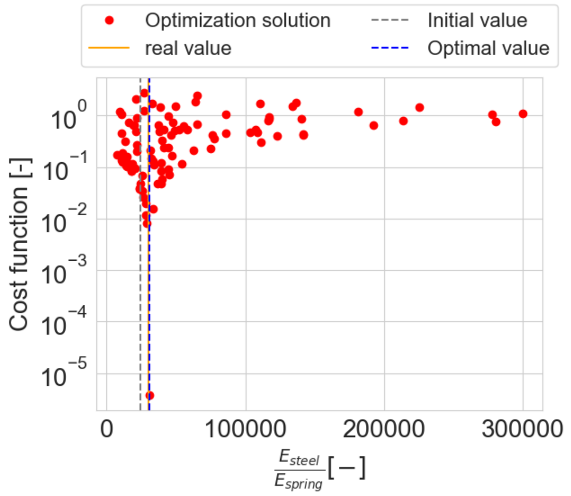

(b) Plot of the $\frac{E_{steel}}{E_{spring}}$ ratios across the 100 solutions from the optimization algorithm. Dashed lines indicate value of the actual ratio (of the reference model) and optimal value obtained from the optimization.

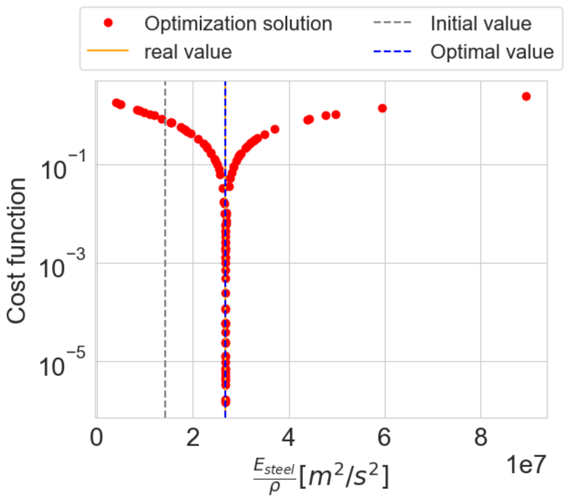

(c) Plot of the $\frac{E_{steel}}{\rho}$ ratios across the 100 solutions from the optimization algorithm. Dashed lines indicate value of the actual ratio (of the reference model) and optimal value obtained from the optimization.

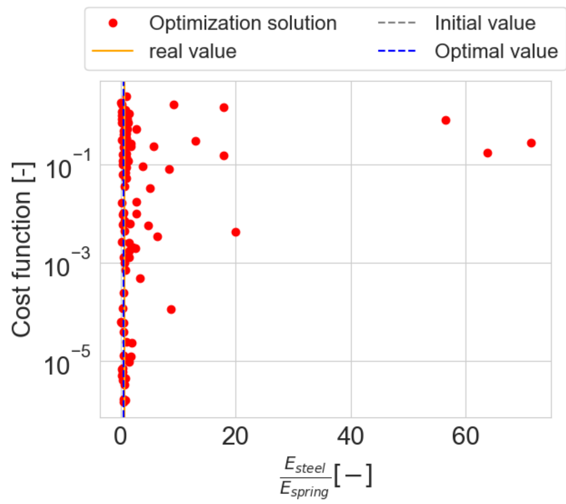

(d) Plot of the $\frac{E_{steel}}{E_{spring}}$ ratios across the 100 solutions from the optimization algorithm. Dashed lines indicate value of the actual ratio (of the reference model) and optimal value obtained from the optimization.

Figure 5.7: Plots comparing the $\frac{E_{steel}}{\rho}$ and $\frac{E_{steel}}{E_{spring}}$ ratios across 100 solutions from the optimization algorithm, for both soft and fixed configurations.

5.3.3. Results - Period Lengthening Values

The period lengthening is the key parameter in this study, and figure 5.8a and figure 5.8b present histograms depicting the distribution of all 100 period-lengthening values obtained for the soft and stiff base condition.

For the soft springs case, the percentage of solutions that gave a period lengthening value within 1% error was only 3.00%. This value is relatively low compared to the errors of the natural frequencies, and it is interesting to understand the reason for this. In figure 5.9a, it can be seen that the error in period lengthening estimated is directly related to the error of the E_{steel}/E_{spring} ratio. If E_{steel}/ρ would affect the period lengthening, not all solutions would be on a line. and it is independent of the E_{steel}/ρ ratio. Therefore, it can be concluded that period lengthening is independent of the density ρ. This observation is further supported by the analytical derivation of period lengthening in equation (2.1), in which the parameter ρ is not present.

For the stiff spring case, figure 5.8b shows a much more shallow distribution. In fact, 100% of the solutions were within 1% error of the actual period lengthening value. Similar to the soft spring case, the E_{steel}/E_{spring} ratio remains the dominant factor influencing period lengthening. However, as seen in figure 5.9b, large overestimation of the E_{spring}/E_{steel} ratio lead to only a very small underestimation of period lengthening, with errors on the order of 10^{-3}, behaving asymptotically as the period lengthening approaches 1. This explains the large error in the estimation of the E_{spring}/E_{steel} in table 5.4. When the E_{spring}/E_{steel} ratio is low, the resulting errors are relatively minor, staying below 1%.

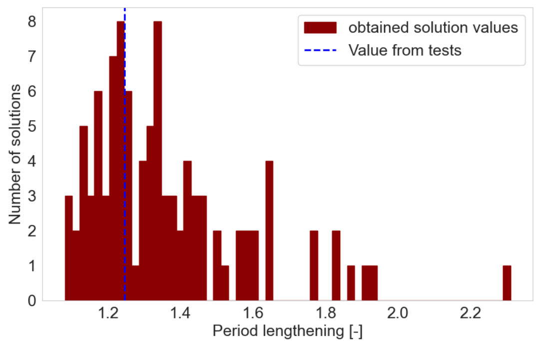

(a) Histogram of the obtained $\tilde{T}/T$ values (soft springs).

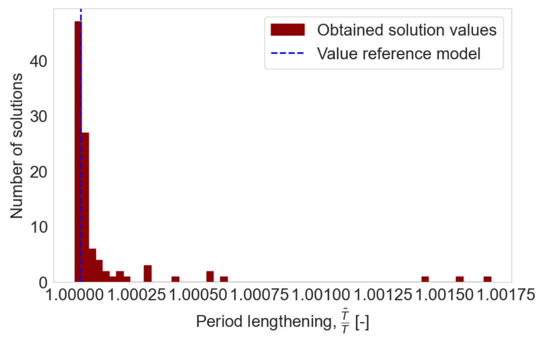

(b) Errors in $\tilde{T}/T$ vs. E_{steel}/E_{spring} ratio (soft springs).

Figure 5.8: Comparison of $\tilde{T}/T$ values for soft and stiff springs.

The results demonstrate that period lengthening is generally more accurately estimated in the stiff spring configuration, where the optimization yields values consistently within 1% error. This improved accuracy can be attributed to the higher sensitivity of period lengthening to the E_{steel}/E_{spring} ratio in the stiff spring case, while the soft spring case shows a greater variation due to the lower sensitivity of this ratio.

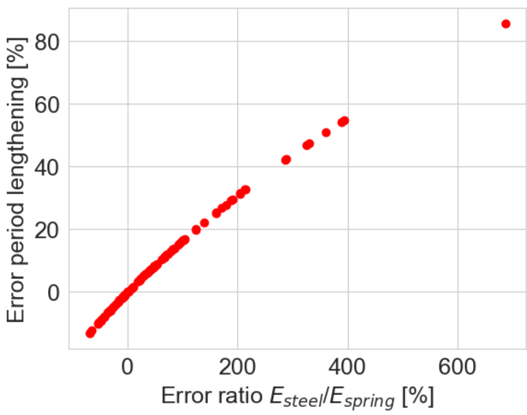

(a) Errors in $\tilde{T}/T$ estimated against errors in E_{steel}/E_{spring} ratio from 100 solutions of the optimization algorithm for the soft spring case. The graph shows the period lengthening is not affected by ρ, as the E_{steel}/E_{spring} ratio dictates the period lengthening.

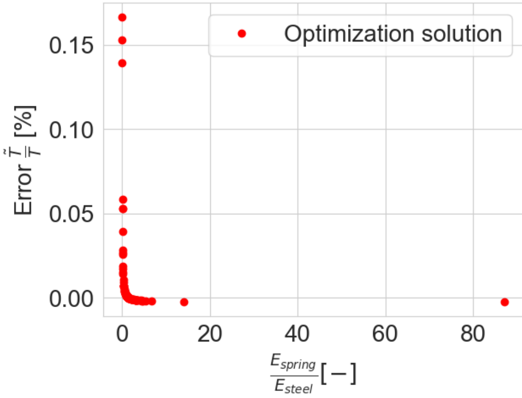

(b) Errors in $\tilde{T}/T$ vs. E_{steel}/E_{spring} ratio for stiff springs.

Figure 5.9: Comparison of errors in $\tilde{T}/T$ against E_{steel}/E_{spring} ratio for stiff springs.

When plotting the period lengthening against the cost function, a clear convergence is observed, similar to the convergence seen when plotting the ratios. The plots in figure 5.10a and figure 5.10b closely resemble the shape of the E_{steel}/E_{spring} ratio plotted against the cost function. Although the convergence in figure 5.10b is less pronounced and does not form a clear V-shape, the period lengthening values fall within a much narrower range, as previously indicated by the histograms. This suggests that, despite the less distinct convergence pattern, the period lengthening estimates are still highly consistent.

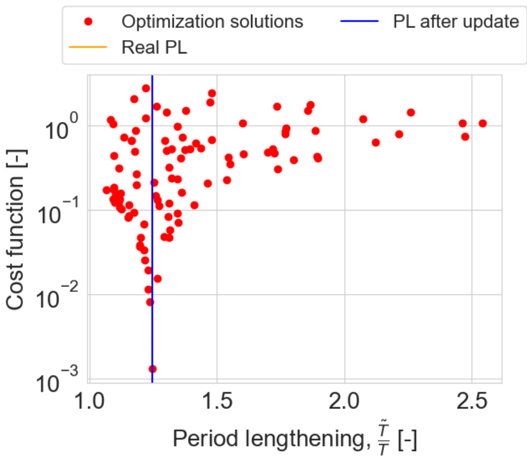

(a) $\tilde{T}/T$ values obtained for the soft spring situation plotted against the cost function.

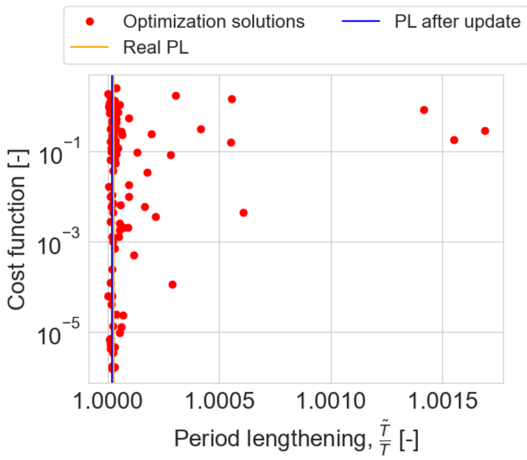

(b) $\tilde{T}/T$ values obtained for the stiff spring situation plotted against the cost function.

Figure 5.10: Comparison of $\tilde{T}/T$ values obtained for the stiff and soft springs situation.

5.4. Conclusion

This chapter presented a detailed analysis of the model updating process using synthetic data. The synthetic data was used to simulate an ideal case without any model or measurement errors. The main focus was on updating an FE (finite element) model for configuration 5, using the dynamic properties (natural frequencies and mode shapes) of a reference FE model. Two different scenarios were considered: one where configuration 5 was mounted on soft springs, and another where it was mounted on stiff springs, to understand how spring stiffness affects the model updating.

The results of the model updating procedure applied demonstrated significant improvements in the accuracy of dynamic property predictions. In general, the test FE model was able to be updated such that the dynamic properties of the reference FE model were matched exactly.

A key observation from the study is that the current approach is unable to accurately estimate individual stiffness and mass properties. Instead, the optimization algorithm focuses on achieving accurate ratios between these properties. In both the soft and stiff spring cases, the dynamic properties of the reference model were matched very well, with errors in the order of 10^{-3}%. However, the individual parameters—like E_{spring}, E_{steel}, and ρ_{steel}—showed large errors, reaching up to 200%. Despite this, the ratios between the properties, $\frac{E_{\text{steel}}}{E_{\text{spring}}}$ and $\frac{E_{\text{steel}}}{E_{\rho}}$, were very accurately estimated, showing that the method updates these ratios more effectively than individual parameters.

Each update cycle began with 100 randomly selected starting points within specific bounds, generating 100 updated sets of structural properties, each with its associated cost function value. By plotting the ratios of the structural properties against the cost function, a clear convergence toward an optimal solution was observed, with the cost function decreasing up to a certain point.

The comparison between soft and stiff springs revealed interesting differences. Since the spring stiffness was already high, the system's behaviour closely resembled a fixed-base situation, where dynamic properties were governed by the $\frac{E_{\text{steel}}}{E_{\rho}}$ ratio. A change in spring stiffness in this case, had very little effect on the dynamic properties of the model. Therefore the period lengthening predicted was in more cases accurate, since a change in the $\frac{E_{\text{steel}}}{E_{\text{spring}}}$ ratio simply didn't affect the dynamic behaviour much and therefore also not the period lengthening. For the soft spring, the dynamic properties and therefore also the period lengthening were much more sensitive to a change in $\frac{E_{\text{steel}}}{E_{\text{spring}}}$ ratio. Therefore, errors were much higher for the solutions obtained from this update, especially for the first natural frequency. In terms of period lengthening—the main parameter being estimated in this thesis—the optimization procedure worked well, with small errors (below 1%). Accurate estimation of the period lengthening was only possible when both property ratios were successfully estimated, with the $\frac{E_{\text{steel}}}{E_{\text{spring}}}$ ratio being especially critical.

There was a clear distinction between the stiff and soft spring cases. The optimization process was much more successful for the stiff springs, as all solutions yielded a period lengthening within 1% of the actual value. In contrast, only 3% of the solutions for the soft springs achieved this level of accuracy. This difference was due to the large overestimation of the $\frac{E_{\text{spring}}}{E_{\text{steel}}}$ ratio, which had only a minor impact on the period lengthening, as it is asymptotic ($\frac{\tilde{T}}{T}$ cannot be less than 1).

In summary, this chapter demonstrated that the current model updating approach can match dynamic properties well, but struggles with accurately estimating individual stiffness and mass parameters. Instead, the process focuses on the ratios between these properties. The study showed that spring stiffness plays a critical role, with soft springs being more sensitive to the $\frac{E_{\text{steel}}}{E_{\text{spring}}}$ ratio, while stiff springs are more influenced by the $\frac{E_{\text{steel}}}{E_{\rho}}$ ratio. Ultimately, the optimization process was more effective for stiff springs, especially in accurately estimating period lengthening.

6
Model updating using experimental data

This chapter presents the results of the model updating procedure applied to various 2D FE models, based on dynamic properties measurements from Marchelli's thesis [18]. These dynamic properties were used as objectives for the optimization. As explained in the methodology chapter (chapter 3), the structural properties of three configurations (C5, C6 and C7) of the small-scale steel model were updated. These configurations were mounted to either soft or stiff springs at the base. All configurations, boundary conditions, and update settings are summarized in section 6.1. In this chapter, results for period lengthening values obtained will be discussed, but first, an in-depth analysis will be provided only for configuration C5 for the sake of brevity. In sections section 6.2, section 6.3 and section 6.4 , this analysis will be discussed, following the same structure as chapter 5, starting with the dynamic properties obtained from the updated FE model, followed by the updated structural properties, and concluding with the period lengthening values, which are the main objective of this thesis. In section 6.1, a summary will be provided for the results of the update procedure applied to all selected test setups.

6.1. Study overview

An overview of the updates performed in this chapter is shown in figure 6.1. Important to note is that sections section 6.2, section 6.3 and section 6.4 only present detailed results for configuration 5 on both stiff and soft springs, for the sake of brevity. In section section 6.7, a comparison will be made for results across all configurations.

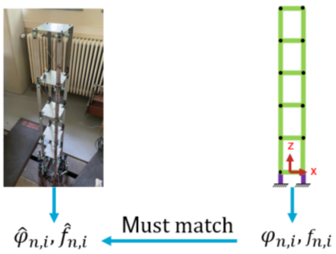

Configuration	C5 & C6 & C7, soft and stiff base
Parameters updated	E_{steel}, rho_{steel}, E_{spring}
Bounds (equal for each parameter)	Round 1: [0.1, 10] Round 2: [0.9, 1.1]
Objective	$3\ \hat{f}_{n,i}$ $3\ \hat{\varphi}_{n,i}$
Starting values	100, random

Figure 6.1: Overview of the FE model, its objectives, and update settings. The update was applied in two steps, with 100 starting points per step, to all configurations with different base conditions.

The optimization was initialized with 100 starting points, each leading to a different solution. The starting points were generated by multiplying the initial parameters by a scalar randomly selected from in between the specified bounds (0.1 and 10). For a detailed description of the update process, refer to chapter 3

6.2. Dynamic Properties

The FE model is updated based on natural frequencies and mode shapes obtained from measurements by Marchelli [18]. This section investigates how well the updated FE model is able to replicate these measurements. To investigate this, only results of the update of configuration 5 on both stiff and soft springs are discussed in detail.

6.2.1. Optimal solution

In table 6.1 and table 6.2, an overview of the dynamic properties (natural frequencies and modeshapes) of the FE model before and after the update are presented. In addition, it shows how the error with respect to the measurements improves by performing the optimization. The solutions shown in the tables correspond to the the solutions with the lowest cost function, of all 100 solutions.

For both the soft and stiff spring cases, a significant improvement is seen in the FEM model's predictions of natural frequencies. In the soft spring case (table 6.1), the error for the first natural frequency dropped from -6.91% to 0.00%, for the second from -10.95% to -0.99%, and for the third from -9.68% to 0.44%. For the stiff spring configuration, the update also shows improvement, though the second natural frequency after update is overestimated by 1.79%, which is higher than the errors for f_1 (0.47%) and f_3 (-0.05%). While these errors are low, they remain higher than those obtained with synthetic data.

For the MAC values, the differences between the soft and stiff springs configurations are less pronounced. In both cases, the errors before the update were relatively small, and the improvements after the update were marginal. For example, for the soft spring case, the MAC values for the first mode increased slightly (from 0.99875 to 0.99964), while the second mode remained nearly constant (from 0.99793 to 0.99805) and the third mode saw a slight decline (from 0.99318 to 0.99209). For the stiff springs case, the MAC values were even more constant for all modes.

	Measurements	FE model (before update)	FE model (after update)	Error before update [%]	Error after update [%]
fn [Hz]	3.33	3.10	3.33	-6.91	0.00
	12.05	10.73	11.93	-10.95	-0.99
	20.45	18.47	20.54	-9.68	0.44
MAC [-]	1	0.99875	0.99964	-0.13	-0.04
	1	0.99793	0.99805	-0.21	-0.20
	1	0.99318	0.99209	-0.68	-0.79

Table 6.1: Comparison of measured values with FE model predictions before and after the update for configuration 5 on soft springs.

	Measurements	FE model (before update)	FE model (after update)	Error before update [%]	Error after update [%]
fn [Hz]	4.25	3.86	4.27	-9.18	0.47
	12.32	10.94	12.10	-11.20	-1.79
	20.79	18.79	20.78	-9.62	-0.05
MAC [-]	1	0.99988	0.99988	-0.012	-0.012
	1	0.99860	0.99860	-0.14	-0.14
	1	0.99308	0.99307	-0.69	-0.69

Table 6.2: Comparison of measured values with FE model predictions before and after the update for configuration 5 on stiff springs.

6.2.2. Errors in estimated natural frequencies across solutions

Figure 6.2a and figure 6.2b show histograms with the errors in the first three natural frequencies.

For the soft springs case, similar trends are observed when compared to the results from synthetic data in previous chapter. The algorithm is more successful in estimating the second and third natural frequencies than the first. The percentage of solutions with an error within 1% is 7.00% for f_1, 11.00% for f_2, and 21.00% for f_3.

For the stiff springs case, the distribution of errors in the natural frequencies shown in figure 6.2b closely resembles the pattern observed in the synthetic data results. The histograms for all three natural frequencies display minimal variation, suggesting that the algorithm faces a similar level of difficulty when optimizing each frequency. In the synthetic case, 44% of the obtained solutions had an error smaller than 1%, and this was consistent across all natural frequencies. In contrast, the current results show that the percentage of solutions with an error within 1% is 35% for f_1, 8% for f_2, and 38% for f_3. It seems that when the algorithm optimizes the natural frequencies, it fits the first and third frequencies well, but this comes at the cost of a larger error for the second frequency. This is supported by figure 6.3, which shows that fitting the first and third natural frequency results in a larger error for the second natural frequency. This fact that the errors cannot be minimized further, can be attributed to either the model error or measurement errors, that prevent the model from being able to fit the measurements exactly.

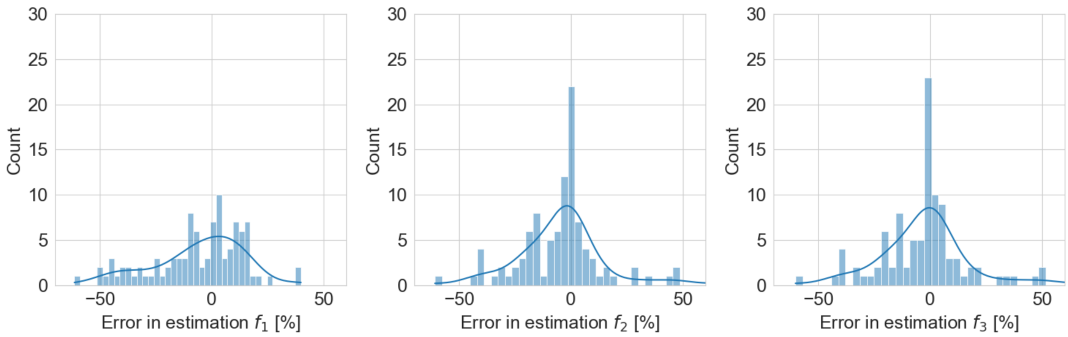

(a) Error distribution for the first three natural frequencies for the soft spring case..

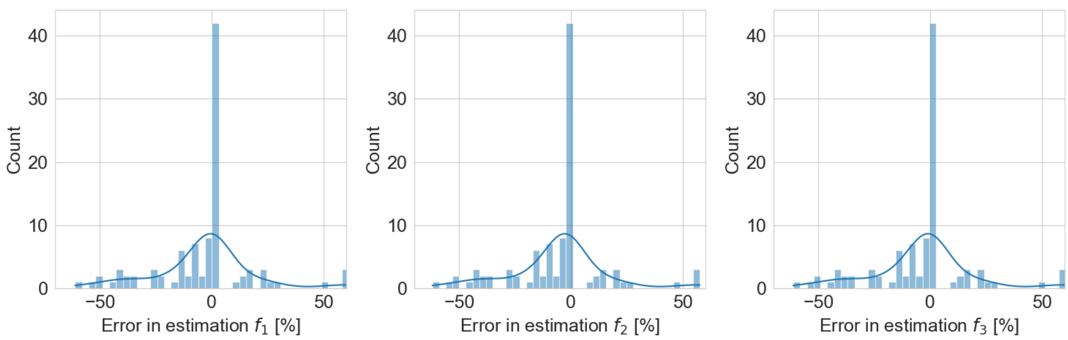

(b) Error distribution for the first three natural frequencies for the stiff spring case.

Figure 6.2: Errors in estimation natural frequencies. Each histograms shows the distribution of errors across 100 obtained solutions.

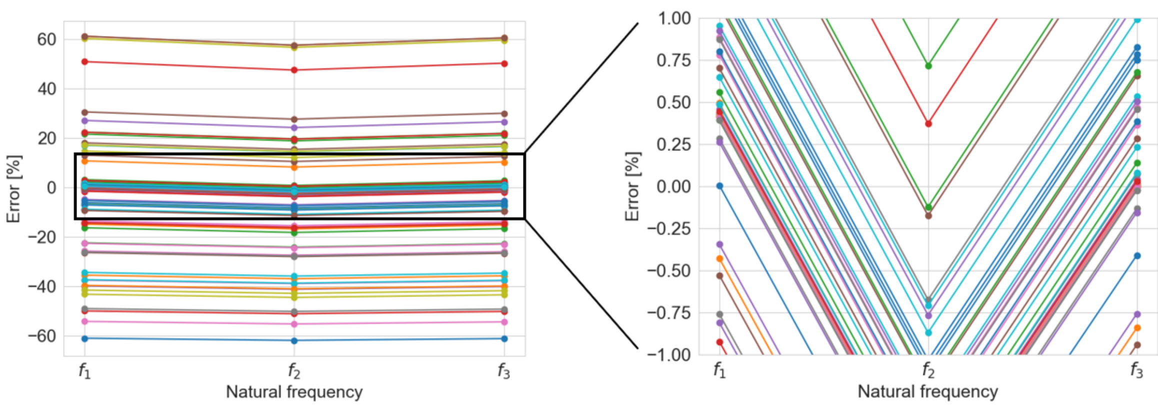

Figure 6.3: Errors in the natural frequencies obtained. The lines connect points corresponding to one obtained solution. It can be seen that there is a consistent difference in error between f_1, f_2 and f_3 and the algorithm cannot fit all three.

6.2.3. Errors in MAC-values

For the soft spring case, the mode shapes of higher modes are generally more challenging to capture accurately, which is similar to the results with synthetic data. As shown in figure 6.4a, this is evident from the wider distribution of obtained MAC values for the higher modes. For the stiff spring case (figure 6.4b), there is very low variability in obtained MAC values. A very steep spike can be seen for all modes, similar to the synthetic case. This is caused by the fact that the MAC for the stiff spring case is very insensitive to variety in E_{spring} and E_{steel}. With the applied ranges of [0,10] for both variables, no clear change in the MAC is achieved. A difference however with the synthetic data is that for the update with synthetic data, the distribution of obtained MAC values is located very close to 1 for all modes, but for the update with experimental data, this spike is centered around lower MAC values for higher modes. This means that with the current settings, it is not possible to achieve a better result in terms of MAC for the third mode. This phenomenon could also be explained by model errors and errors in the measurements.

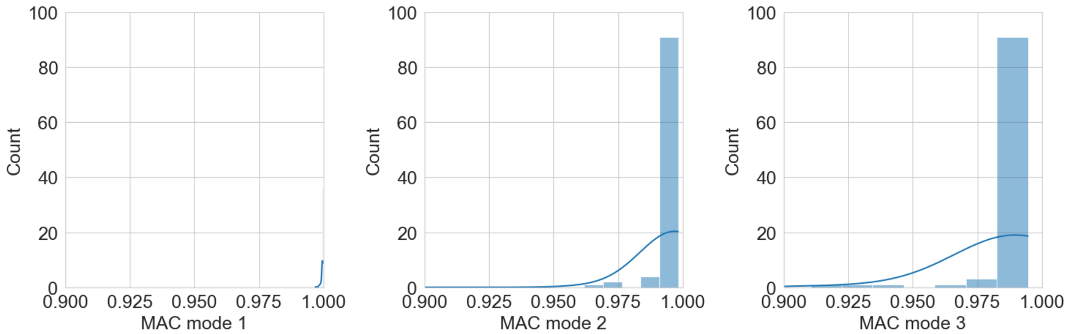

(a) MAC values of the first three modes, for the soft spring case.

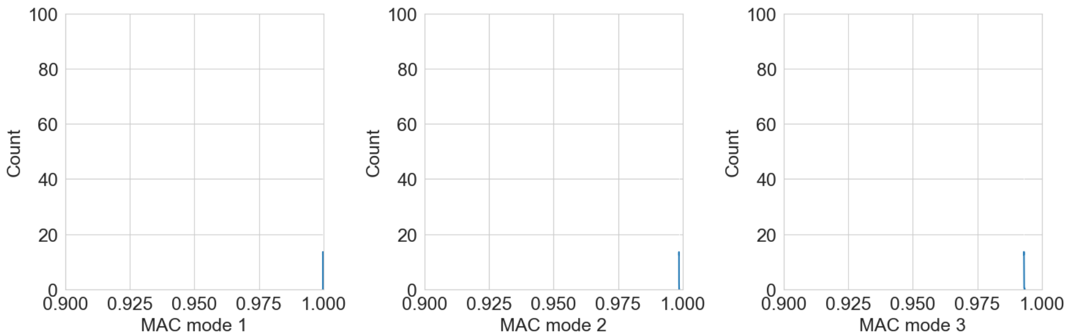

(b) MAC values of the first three modes, for the stiff spring case.

Figure 6.4: MAC values for configuration 5 on a soft and stiff base, updated with measurements from Marchelli [18].

6.3. Structural Properties

In table 6.3 and table 6.4, the initial and updated values of the three structural parameters for the soft and stiff spring case are presented in two tables. The values in these two tables correspond to the solutions with the lowest cost functions.

When using experimental data, it is again the ratios that are optimized, rather than the individual parameter values. For both the soft and stiff spring cases, it can be seen that E_{spring}, E_{steel} and ρ are multiplied by large scalars, and therefore, the updated values are unrealistically large. For example, the E-modulus of steel being 4.51 times higher than the actual E-modulus for the soft spring case (table 6.3). However, when looking at the ratios $\frac{E_{steel}}{\rho}$ and $\frac{E_{steel}}{E_{spring}}$, more reasonable scalars are obtained. For example, as shown in table 6.3, the initial $\frac{E_{steel}}{\rho}$ ratio for the soft spring case is 2.68×10^7, and after optimization, this value increases to 3.33×10^7. This reflects a 24.57% increase in stiffness relative to mass, that could be explained by the fact that certain features of the small-scale steel model, such as the mass contributed by corner connections, bolts, and sensors, were not included in the FE model. Additionally, the stiffness increase may be due to corner connections. The FE model assumes rigid, monolithic connections between the column and floor plates, while in reality, these connections significantly increase the stiffness of the columns over a greater length than just at the connection points.

When comparing the $\frac{E_{steel}}{\rho}$ ratio in both tables, the scalar applied in the soft spring case was 1.24, while it was 1.22 in the stiff spring case. Since the ratio reflects only the properties of the small-scale steel structure, which remains unchanged in both scenarios, it is expected that the $\frac{E_{steel}}{\rho}$ values would be nearly identical. Indeed, the value for the solution with the lowest cost function in the soft spring case was 33,333,809.2, compared to 32,764,166.4 in the stiff spring case, a difference of only 1.71%.

	Starting model	**Updated model (lowest cost)**		
Parameters	**Value**	**Bounds for update**	**Scalar applied**	**Updated value**
E_{steel} [Pa]	2.10E+11	[0.1, 10]	4.51	9.47E+11
ρ [kg/m^3]	7850	[0.1, 10]	3.62	2.84E+04
E_{spring} [Pa]	6.94E+06	[0.1, 10]	3.71	2.58E+07
E_{steel}/E_{spring} [-]	3.03E+04	[0.01, 100]	1.21	3.67E+04
E_{steel}/ρ [m^2/s^2]	2.68E+07	[0.01, 100]	1.24	3.33E+07

Table 6.3: Comparison of the starting model parameters and the updated model with the lowest cost function for the soft spring case. The scalar applied to each parameter in the optimization process is also indicated, including the parameter ratios.

	Starting model	**Updated model (lowest cost)**		
Parameters	**Value**	**Bounds for update**	**Scalar applied**	**Updated value**
E_{steel} [Pa]	2.10E+11	[0.1, 10]	1.60	335092499535.59
ρ [kg/m^3]	7850	[0.1, 10]	1.30	10227.41
E_{spring} [Pa]	6.94E+06	[0.1, 10]	2.59	749278471899.11
E_{steel}/E_{spring} [-]	0.72	[0.01, 100]	0.63	0.45
E_{steel}/ρ [m^2/s^2]	2.68E+07	[0.01, 100]	1.23	3.28E+07

Table 6.4: Comparison of the starting model parameters and the updated model for the stiff spring case with the lowest cost function. The scalar applied to each parameter in the optimization process is also indicated, including the parameter ratios.

6.3.1. Optimization of ratios

When investigating the results of all 100 obtained solutions in both cases, one can see that no relation between the individual parameter values and the cost function exists. For example, Figure 6.6b plots the parameter values alongside the cost function- for the soft spring situation. It shows that the optimized values are all over the place.

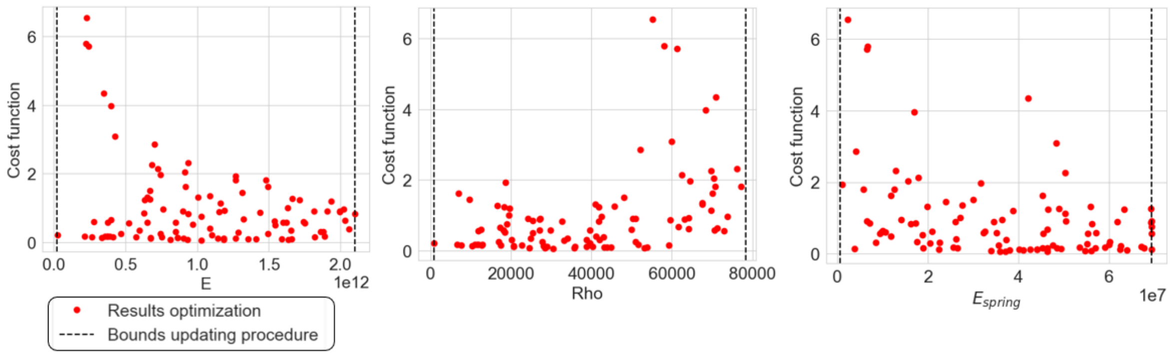

Figure 6.5: Individual structural parameters across 100 solutions plotted against the cost function.

However, when focusing on the ratios between structural parameters, specifically $\frac{E_{steel}}{\rho}$ and $\frac{E_{steel}}{E_{spring}}$, rather than the individual parameters, a clear convergence can be seen. Figure 6.6 shows for both the stiff and soft spring case these ratios obtained across the 100 solutions. Clearly, it shows that given a certain ratio, there is a minimum value for the cost function that can be obtained. This minimum value decreases up to the optimal value for the ratio. This pattern can be seen in all four plots and is consistent with the results with synthetic data. Only for the stiff spring, in figure 6.6d one can see that for the $\frac{E_{steel}}{E_{spring}}$, it is harder to find the optimal value. At the same time, in figure 6.6c, it can be seen that the pattern becomes much more clear for the $\frac{E_{steel}}{\rho}$ ratio. This behaviour was also observed in the results with the synthetic data, indicating that since the springs are already quite stiff, a change in stiffness is very hard to estimate, and an overestimation in spring stiffness only leads to very small errors since the $\frac{E_{steel}}{\rho}$ ratio is governing the dynamic behaviour.

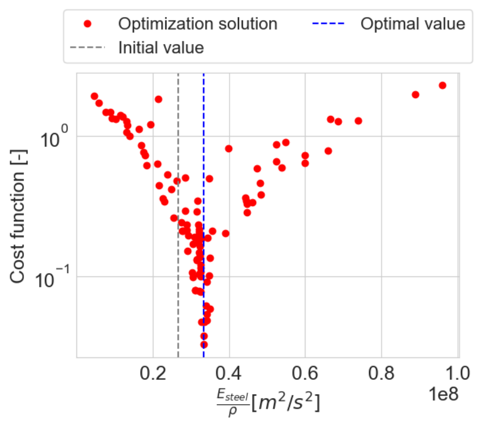

(a) Plot of the $\frac{E_{steel}}{\rho}$ ratios across the 100 solutions from the optimization of configuration 5 on soft springs . Dashed lines indicate value of the ratio before the update and the optimal value obtained after the optimization.

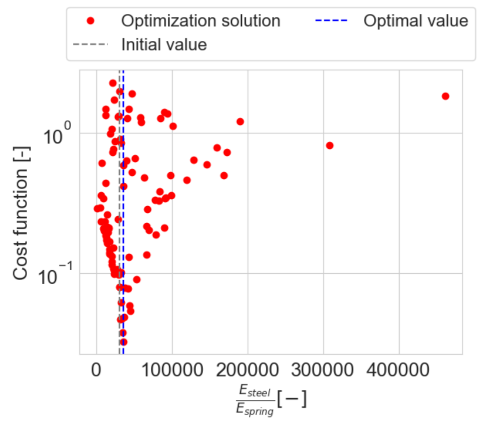

(b) Plot of the $\frac{E_{steel}}{E_{spring}}$ ratios across the 100 solutions from the optimization of configuration 5 on soft springs . Dashed lines indicate value of the ratio before the update and the optimal value obtained after the optimization.

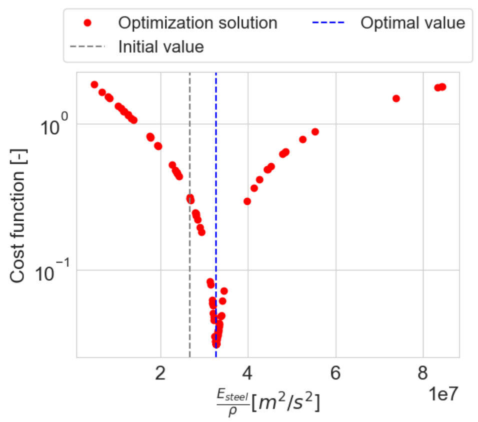

(c) Plot of the $\frac{E_{steel}}{\rho}$ ratios across the 100 solutions from the optimization of configuration 5 on stiff springs . Dashed lines indicate value of the actual ratio (of the reference model) and optimal value obtained from the optimization.

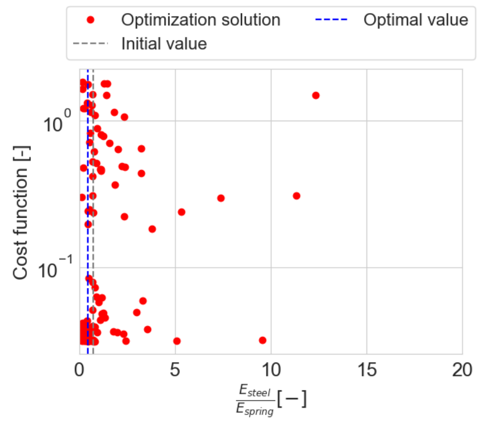

(d) Plot of the $\frac{E_{steel}}{E_{spring}}$ ratios across the 100 solutions from the optimization of configuration 5 on soft springs. Dashed lines indicate value of the actual ratio (of the reference model) and optimal value obtained from the optimization.

Figure 6.6: Plots comparing the $\frac{E_{steel}}{\rho}$ and $\frac{E_{steel}}{E_{spring}}$ ratios across 100 solutions from the optimization algorithm, for both soft and fixed configurations.

In figure 6.7, the $\frac{E_{steel}}{\rho}$ and $\frac{E_{steel}}{E_{spring}}$ ratios are plotted in a 3D plot for the soft spring case, against the cost function. It can be seen that a surface forms, showing the lowest obtainable cost function for a certain ratio.

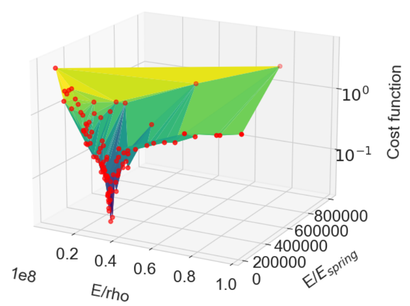

Figure 6.7: The two ratios plotted against the cost function for the soft spring case. The cost function clearly converges towards a minimum value.

6.4. Period lengthening values

In this section, the period lengthening values obtained from the updating procedure are analyzed. First, the results of the updating of the FE model of configuration C5 on a soft and stiff springs base will be presented in detail. Finally, in section 6.7, the results for period lengthening when the procedure is applied to all configurations are discussed.

6.4.1. Distribution across solutions

The distribution of period lengthening values across the 100 solutions is shown in figure 6.8a for the soft spring case and in figure 6.8b for the stiff spring case. It is clear that the distribution for the stiff spring case is significantly narrower. This is especially evident when considering the difference in the x-axis scales between the two graphs. The difference in scaling is intentional, as adjusting the axes to be identical would cause the sharp peak in figure 6.8b to disappear.

The obtained values were compared to those determined from the experiments of Marchelli [18] rather than the true values. It was found that in the soft spring case, 3% of all solutions had errors of less than 1%, while for the stiff spring case, none of the solutions fell below this threshold (compared to 100% in the synthetic data update). However, this does not imply that the period lengthening estimates are significantly inaccurate. When the error threshold was increased to 2.26%, 100% of the obtained values had errors below this limit. This discrepancy can be attributed to the presence of model and measurement errors introduced in the experimental setup.

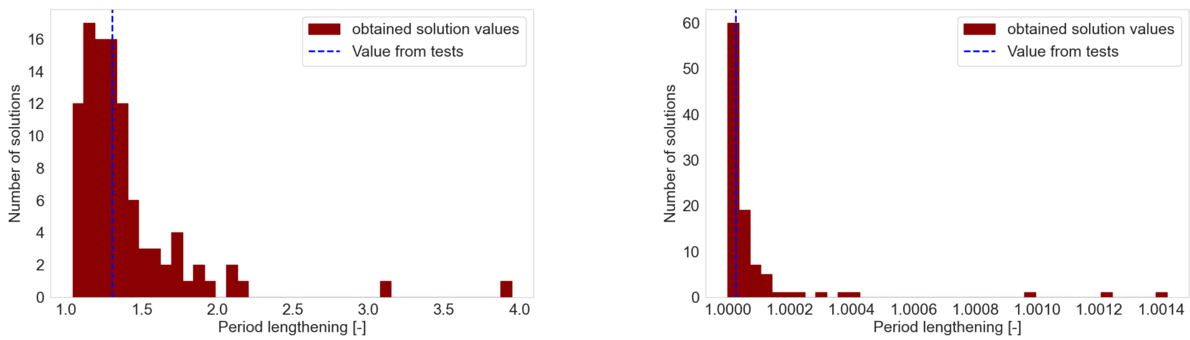

(a) Histogram of the obtained $\tilde{T}/T$ values (soft springs).

(b) Histogram of the obtained $\tilde{T}/T$ values (stiff springs).

Figure 6.8: Comparison of the obtained $\tilde{T}/T$ values for configuration 5 on soft springs (a) and stiff springs (b).

In figure 6.9a and figure 6.9b, the relationship between the obtained period lengthening values and the corresponding optimization cost function across the 100 solutions is plotted for both the stiff and soft spring conditions. A notable difference can be observed between the two cases, which mirrors the results from the synthetic data study. In the soft spring case, there appears to be a clear V-shaped convergence of the cost function towards a specific period lengthening value, as shown in figure 6.9a.

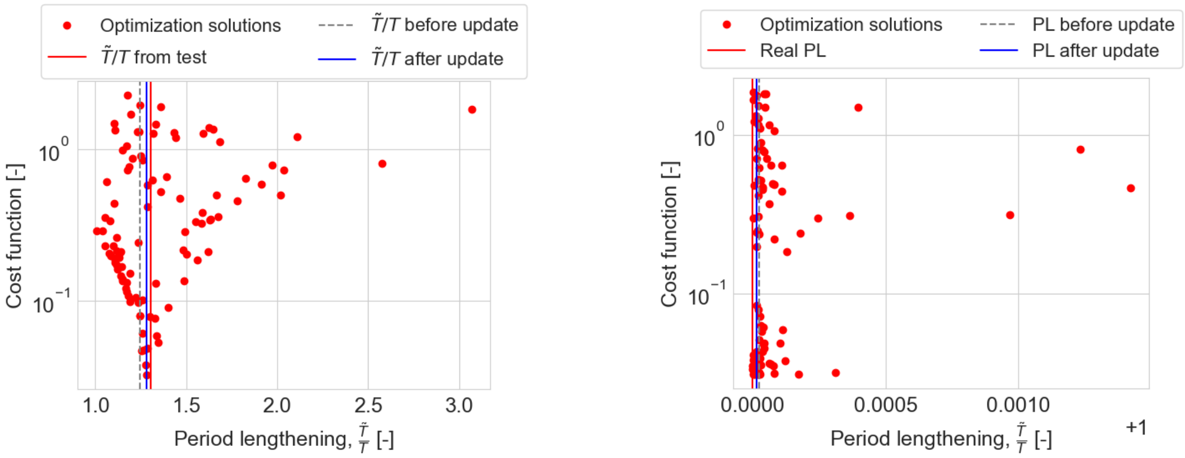

(a) Period lengthening ($\tilde{T}/T$) values of each of the 100 solutions plotted against the corresponding cost function for configuration 5 on soft springs.

(b) Period lengthening ($\tilde{T}/T$) values of each of the 100 solutions plotted against the corresponding cost function for configuration 5 on soft springs.

Figure 6.9: Comparison of the obtained $\tilde{T}/T$ values for configuration 5 on soft springs (a) and stiff springs (b).

6.5. Consistency of results

In the update procedure, 100 initial solutions were generated to explore the optimization space. To assess whether this sample size was sufficient, the process was repeated with another set of 100 solutions. The results of the period lengthening from both optimization runs are shown in figure 6.15a. The graph reveals that the second run produced a solution with a higher cost function, resulting in a period lengthening of 1.281, compared to 1.292 from the first run. Moreover, the error relative to the measured period lengthening (1.306) was significantly larger in the second run—1.92% compared to 1.07% in the first run. This suggests that the first optimization run provided a better approximation of the measured period lengthening and that the procedure does not return a stable, converged value yet.

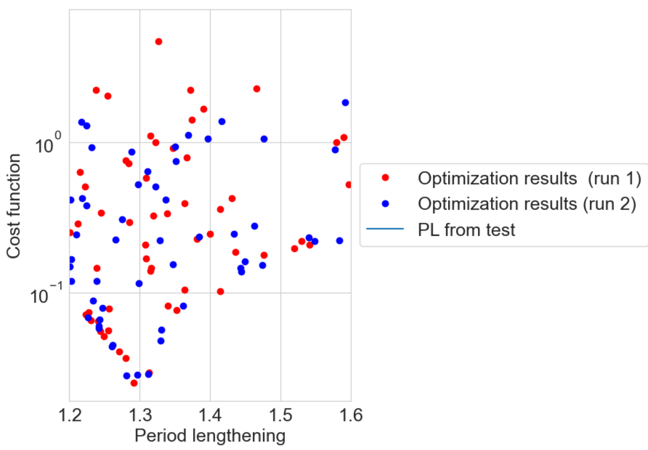

Figure 6.10: Two solution sets obtained by running the optimization procedure twice with 100 starting values. The graph shows that the current amount of starting values does not lead to a completely converged value of $\tilde{T}/T$.

6.5.1. Sensitivity to number of starting points

To further investigate the variability in period lengthening values across different runs, the updating procedure was executed 100 times using various numbers of starting points. This analysis was limited to the soft spring case, as the variability in period lengthening for the stiff spring case was minimal (see figure 6.8b). Figure 6.11 presents three histograms, each showing the distribution of $\tilde{T}/T$ values corresponding to the optimal result (i.e., the lowest cost function) obtained after running the update procedure 100 times, with 50, 100, and 200 starting points.

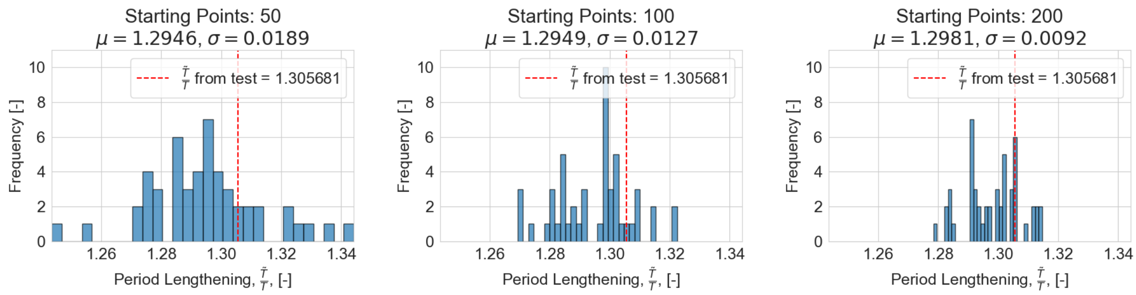

(a) 50 starting points. The coëefficient of variation CV = 1.5%

(b) 100 starting points. The coëefficient of variation CV = 0.98%

(c) 200 starting points. The coëefficient of variation CV = 0.71%

Figure 6.11: Histograms showing the distribution of $\tilde{T}/T$ values corresponding to the optimal results (lowest cost function) for 50, 100, and 200 starting points after running the update procedure 50 times.

The histograms in figure 6.11 suggest that while the initial sample size of 100 starting points provided a reasonable estimate of the period lengthening, the optimal solution had not yet been fully identified. Increasing the number of starting points to 200 reduced the standard deviation of the obtained values, indicating that further increasing the number of starting points might eventually lead to a stable period lengthening value.

However, when the cost function is taken into consideration, this perspective changes. In figure 6.12, three plots display the obtained $\frac{\tilde{T}}{T}$ values against the cost function for runs with 50, 100, and 200 starting points. Only the values corresponding to the lowest cost function from each of the 100 runs are plotted. While the same convergence toward a specific period lengthening value is observed, there is a key difference: the period lengthening values do not converge to a single optimum. Instead, multiple solutions with nearly identical cost functions emerge, creating a 'horizontal' plateau—an area where further improvement of the solution seems to not be possible.
at the measured value.

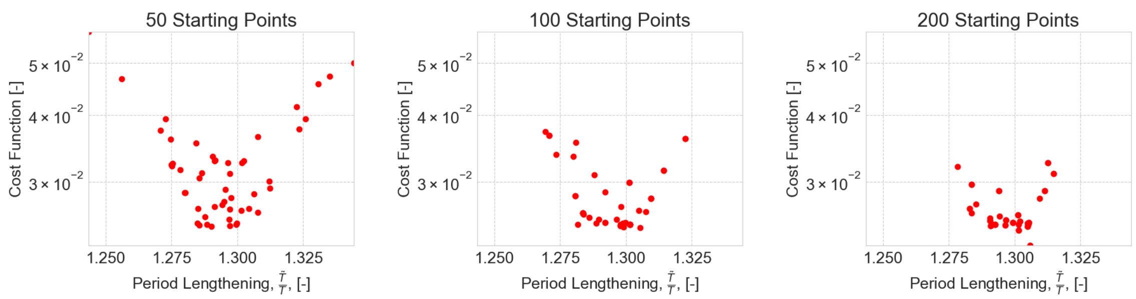

(a) 50 starting points

(b) 100 starting points

(c) 200 starting points

Figure 6.12: Scatter plots showing the relationship between period lengthening ($\tilde{T}/T$) and cost function values for 50, 100, and 200 starting points after running the update procedure 50 times.

It's important to note that this plateau was not observed in the update procedure using synthetic data (section 5.3.3), where a much steeper and more distinct convergence was achieved with cost function values reaching order 10^{-6}. Additionally, the presence of this plateau is consistent across all plots in figure 6.12, even as the number of optimal solutions increases. Only one point in figure 6.12c , the plot showing the results for the optimization with 200 starting points, is reaching lower than the plateau. This point has a cost function that is 0.001836 lower- than the point. Interestingly, the point is almost exactly In figure 6.13, three histograms illustrate the distribution of cost function values for the optimal solutions obtained after running the optimization 100 times with 50, 100, and 200 starting points. As the number of starting points increases, the distribution of values becomes progressively narrower. However, it is noticeable that the lowest cost function value achieved does not really decrease, despite the increased number of starting points. This is indicative of this observed plateau.

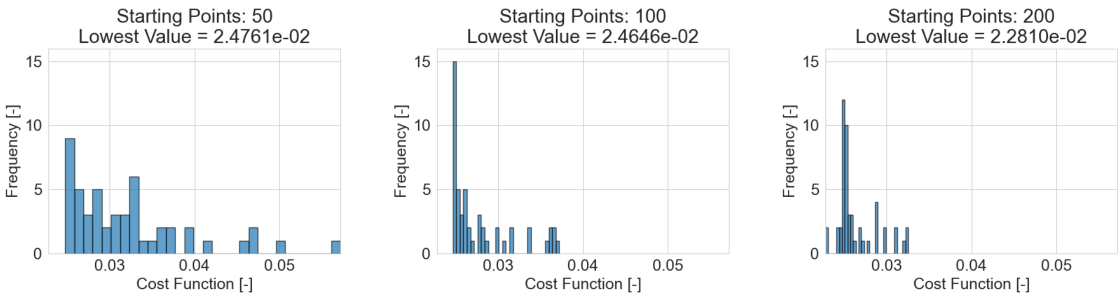

(a) 50 starting points **(b)** 100 starting points **(c)** 200 starting points

Figure 6.13: Histograms showing the distribution of cost function values corresponding to the optimal results for 50, 100, and 200 starting points after running the update procedure 50 times.

6.6. Updating with refined solution space

Given that running the code with multiple starting points over many iterations is time-consuming, an alternative approach was tested to optimize the process. In this approach, the FE model is first updated using 200 starting points only one time. After the initial run, the values of E_{steel}, $E_{springs}$, and ρ that corresponded to the lowest cost function were selected as new starting points for a second step of optimization. In this second step, the solution space was then refined by lowering bounds (initially set at [0.1, 10]) specified for the parameters, allowing the optimization to concentrate more effectively. Focusing on a refined solution space is more effective than simply increasing the number of starting values, as it reduces the search area and increases the likelihood of converging to a global optimum.

The new bounds were based on the results of section 6.5.1. In figure 6.14, two histograms are depicted, showing the distributions of the E_{steel}/ρ and $E_{steel}/E_{springs}$ ratios corresponding to the lowest cost function after 100 runs with 200 starting points.
For the E_{steel}/ρ ratio, the values fell between 3.30e+07 and 3.41e+07, or 0.98 and 1.01 times the median value of 33689381.12. For the $E_{steel}/E_{springs}$ ratio, the values ranged between 2.50e-05 and 2.87e-05, or 0.94 and 1.08 times the median value of all the solutions.

Since bounds can only be applied to the individual parameters (E_{steel}, ρ, and $E_{springs}$), a range of [0.92, 1.1] was selected for these parameters. This results in bounds of approximately [0.84, 1.20] for the E_{steel}/ρ and $E_{steel}/E_{springs}$ ratios, given by the calculation [(0.92/1.1) - (1.1/0.92)].

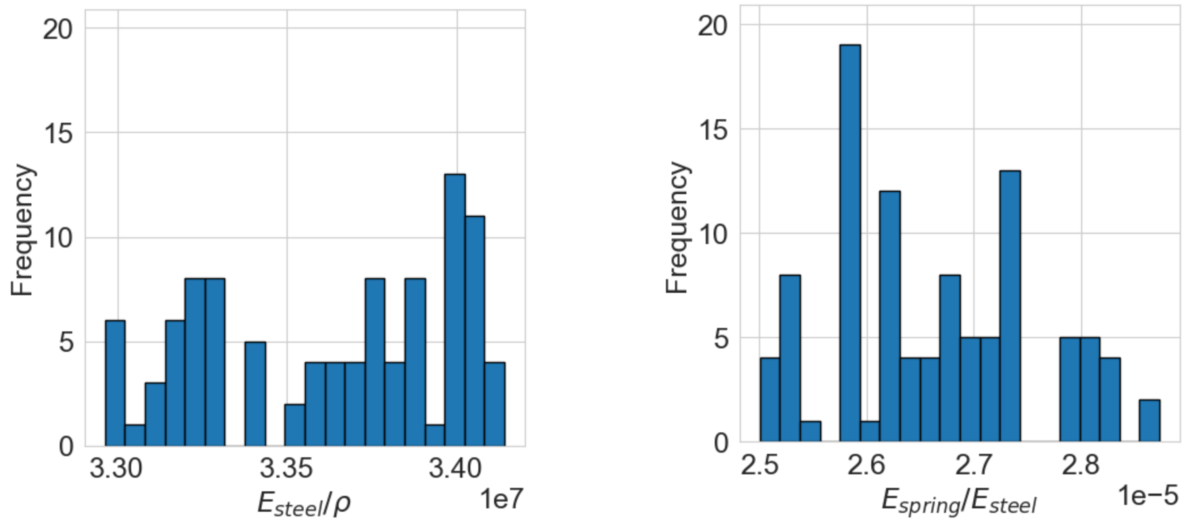

(a) Histogram of all E/ρ ratios obtained by running the updating procedure 100 times.

(b) Histogram of all E/E_{spring} ratios obtained by running the updating procedure 100 times.

Figure 6.14: Comparison of the E/ρ and E/E_{spring} ratios from 100 runs of the updating procedure with 200 starting points.

In figure 6.15, the results of an update of C5, soft springs, after a refinement of the bounds and two steps of the optimization are shown. Now, almost all solutions have low cost functions (all of them are below 0.07). The same plateau as in figure 6.12 can be observed.

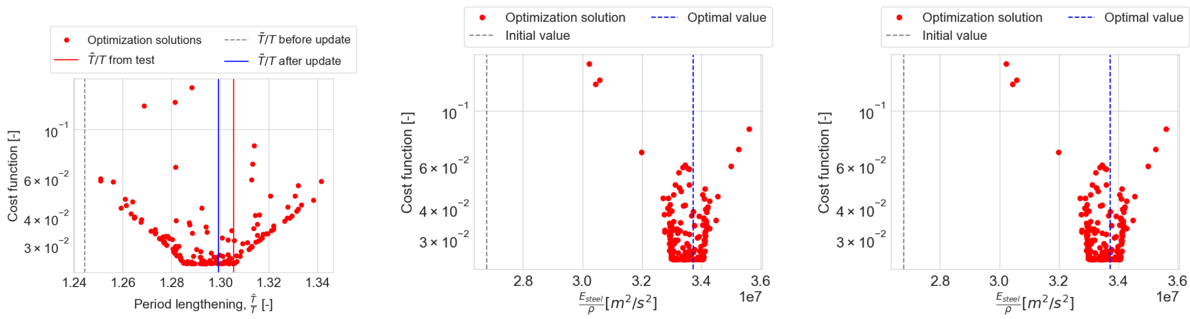

(a) Period Lengthening: $\tilde{T}/T$ solutions after redefining bounds.

(b) E/ρ values after running with smaller parameter bounds.

(c) E_{steel}/E_{spring} values with smaller parameter bounds.

Figure 6.15: Comparison of period lengthening, E/ρ, and E/E_{spring} ratios from 30 runs of the updating procedure.

The plateau exists due to a combination of modeling and measurement errors. Since the model cannot fully capture the dynamic behavior of the real structure, it is inherently unable to perfectly match the measured natural frequencies and mode shapes. Furthermore, errors in measurements and uncertainties add another layer of complexity, making it even harder to achieve an exact fit. As a result, fitting the natural frequencies and mode shapes becomes a trade-off: solutions with similar cost functions, as shown in figure 6.16a and figure 6.16b, exist because some solutions may achieve a very good fit for the first natural frequency but a poorer fit for the second, while others might have the opposite result. Consequently, even though the cost functions are nearly identical, the solutions themselves differ. This trade-off is illustrated in figure 6.16, where two plots display the obtained natural frequencies and mode shapes. The color of each line, which connects values of a specific solution, represents the cost function value. In figure 6.16a, it is evident that as the error for the second natural frequency decreases, the error for the third natural frequency increases.

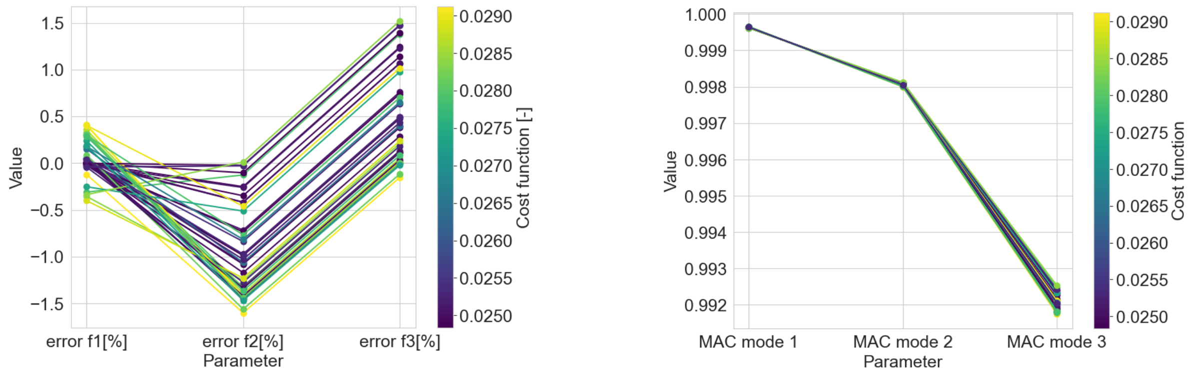

(a) Natural frequencies of the first three modes of the solutions obtained from the update with modified bounds. In this plot, only solutions with a cost function lower than 0.035 are shown.

(b) MAC values of the first three modes of the solutions obtained from the update with modified bounds. In this plot, only solutions with a cost function lower than 0.035 are shown.

Figure 6.16: Values for dynamic properties, obtained from running the optimization in two steps with refined bounds

6.7. Application to all configurations

The two-step approach explained in section 6.6 was applied to all configurations, C5, C6 and C7 on soft and stiff springs. In table 6.5 and table 6.6, an overview is given on the period lengthening values obtained for the different configurations on the two spring types.

Configurations	Stiff spring				
	Period lengthening (measurements)	Period lengthening (FE model)	Period lengthening (updated FE model)	Error before update [%]	Error after update [%]
C5	1.02376	1.00003	1.00002	2.32%	2.32%
C6	1.02205	1.00003	1.00031	2.15%	2.13%
C7	1.02026	1.00003	1.00058	1.98%	1.93%

Table 6.5: Overview of the period lengthening values for the stiff spring, obtained from measurements, FE model, and updated FE model.

Configurations	Soft spring				
	Period lengthening (measurements)	Period lengthening (FE model)	Period lengthening (updated FE model)	Error before update [%]	Error after update [%]
C5	1.30568	1.24442	1.29933	4.69%	0.49%
C6	1.31103	1.24667	1.31403	4.91%	0.23%
C7	1.31460	1.24956	1.31861	4.64%	0.31%

Table 6.6: Overview of the period lengthening values for the soft spring, obtained from measurements, FE model, and updated FE model.

For the soft spring cases, it can be seen that the period lengthening significantly improves for all configurations, going from above 4 % error to lower than 0.5 % error. In figure 6.17 an overview of the obtained period lengthening values is depicted for all configurations. The range over which the plateau is observed is also indicated.

For the stiff spring, a less pronounced effect can be seen. The values obtained after optimization only improve slightly with some per cent points. This can be due to the fact that since the stiffness of the springs is very high and the period lengthening is already close to one (fixed base situation) and therefore, errors of the model are more pronounced. Another reason can be that since the model is so insensitive to the spring stiffness, the cost function becomes very flat and it is not possible to improve.

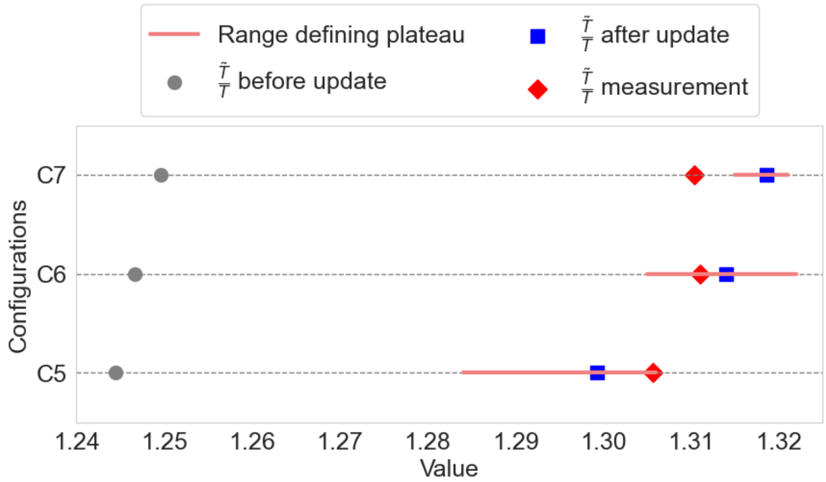

Figure 6.17: $\tilde{T}/T$ before and after the update, compared to the values from measurements by Marchelli [18]. The light-red line indicates the area of the plateau, meaning the area where the cost function value does not improve much as the model is unable to fit all natural frequencies

6.8. Conclusion

This chapter applied the model updating process to various 2D finite element (FE) models using experimental data from Marchelli's thesis as input. The dynamic properties measured in the experiments were used as the optimization targets. The model updating focused on three configurations (C5, C6, and C7), each mounted on either soft or stiff springs at the base. Detailed results for configuration 5 on both soft and stiff springs were discussed in this chapter, along with an overview of the performance for all configurations.

The updated FE model showed improved predictions of the natural frequencies compared to the initial model. Similar trends were observed when compared to the update using synthetic data; for instance, in the soft spring case, the error for f_1 was generally larger. However, the update based on experimental data introduced additional differences due to model and measurement errors. For example, in the stiff spring case, the second natural frequency consistently exhibited a slightly larger error (though still minor), suggesting a trade-off between fitting different frequencies. In contrast, with the synthetic data update, the errors were more uniform across all frequencies.

With regard to the mode shapes, represented by MAC values, the updated FE model showed only marginal improvements. These improvements were more significant in the update with synthetic data, where the exact mode shapes could be matched. However, for the update with experimental data, achieving a MAC value of 1 was not possible, indicating that the model could not fully replicate the dynamic behavior, regardless of the structural properties chosen. This limitation is likely due to uncertainties arising from either the model or measurement errors.

In terms of structural properties, similar patterns were observed as when using synthetic data. The optimization process primarily adjusted the ratios between stiffness and mass properties, rather than the individual parameters. The updated values for E_{spring}, E_{steel}, and ρ were unrealistically large, but the ratios $\frac{E_{\text{steel}}}{E_{\text{spring}}}$ and $\frac{E_{\text{steel}}}{E_{\rho}}$ were optimized to more reasonable values. This behavior suggests that the optimization algorithm is effective in matching the dynamic behavior of the system, even though the individual parameter estimates remain inaccurate.

Regarding period lengthening, the obtained values were compared to those derived from Marchelli's experimental data [18], rather than the true values. The study clearly demonstrated that both model and measurement errors had a significant impact on the results. For the soft spring case, only 3% of the solutions had errors of less than 1%, indicating accurate period lengthening values for $\frac{\tilde{T}}{T}$., similarly to the results with synthetic data. In contrast, for the stiff spring case, none of the solutions had errors below 1%, whereas 100% of the solutions in the synthetic data update reached this level of accuracy. Nevertheless, 100% of the stiff spring solutions had errors below 2.26%, indicating that while the accuracy of the model updating procedure was impacted by the presence of model or measurement errors, the overall precision remained consistent.

An important aspect of this study involved investigating the consistency of results. The optimization process was repeated to assess the variability of the period lengthening values. For the soft spring configuration, there was significant variability across the 100 solutions, indicating that the optimization process had not fully converged. When the optimization was repeated over 100 runs, the distribution of period lengthening values continued to show variability for the soft spring case. Increasing the number of starting points reduced this variability, but was very time inefficient. In addition, even with these refinements, the cost function could not be minimized further for all natural frequencies, suggesting that either model errors or measurement inaccuracies limited the optimization's potential. Another approach, overcoming the time inefficiency, was refining the bounds for a second update step. This also led to improved consistency, with more solutions converging to lower cost functions. However, the same plateau was observed, where the cost function did not improve.

Finally, when comparing period lengthening values across all configurations, the results showed significant improvement for configurations mounted on soft springs. The error in period lengthening predictions dropped from above 4% to below 1%. For the stiff springs, the improvement was less pronounced, as the initial errors were already quite small. This can be explained by the fact that, with period lengthening values close to 1, changes in spring stiffness had a less significant impact, making the system less sensitive to updates in the $E_{\text{spring}}/E_{\text{steel}}$ ratio.

In conclusion, the model updating procedure applied to experimental data provided similar insights as those obtained from synthetic data. While the dynamic properties were matched effectively, the optimization primarily focused on achieving accurate ratios between stiffness and mass properties. The study highlighted that the model updating process was more effective for stiff spring configurations, with more consistent period lengthening predictions and a better overall fit to the experimental data. For the soft spring case, model and measurement errors made it not possible for the algorithm to come to one solution of the period lengthening.

7

Discussion and Conclusion

This research investigated the possibility of determining the period lenghtening ($\tilde{T}/T$) for a structure through model updating. The period lengthening of a structure is the elongation of the first natural frequency due to a change in the boundary condition, namely the addition of a flexible base. Period lengthening, i.e. as a measure of the ratio between stiffnesses of superstructure and foundation, is fundamental to SSI. The main research question of this thesis was the following:

"How can the period lengthening of a structure be estimated reliably using vibration measurements?"

The hypothesis when starting this research was that since the period lengthening reflects the stiffness ratio between structure and foundation, this property could be determined more accurate than individual structural properties through model updating based on vibration measurements. To understand the procedure, two FE models, representing a small-scale steel model on a soft and a stiff spring foundation, were updated first using synthetically generated modal data, extracted from other reference FE models.

Of this this small-scale steel model, vibration measurements had been conducted in the past, and dynamic properties such as mode shapes and natural frequencies were known. Some factors were excluded from the FE model, such as the influence of the L-shaped connections, the measurement equipment, and the effect of bolts on the mass and stiffness of the system. Despite these omissions, the model was able to reasonably predict the dynamic behavior of the structure even before the update, with errors around 10%. The results were also compared with those obtained from Marchelli's model, where the differences were similarly small (differences up to 7.44%) but also a few slightly different assumptions were made. This demonstrates that the FE model was set up correctly.

The 2D FE model, consisting of Timoshenko beam elements, was given initial structural properties, which lead to a mismatch between dynamic properties measured and numerically calculated. This mismatch was then minimized by updating the structural properties of the FE model using a Sequential Least Squares Quadratic Programming (SLSQP) algorithm. After updating the structural properties, the period lengthening could be determined for the FE model and compared to period lengthening values calculated from the vibration measurements.

The results from the update using synthetic data show that the model can be updated to produce the exact same dynamic properties as the reference model (zero error for both natural frequencies and mode shapes). This confirms that the optimization process proceeds correctly, without being affected by errors in the code. The results of the update with synthetic data demonstrated that the algorithm primarily resolves the ratios between mass and stiffness parameters, specifically $\frac{E_{steel}}{\rho}$ and $\frac{E_{steel}}{E_{spring}}$, to replicate the reference model's behavior and correctly determine the period lengthening. While the individual properties themselves were not accurately determined—their values deviated significantly—the ratios $\frac{E_{steel}}{\rho}$ and $\frac{E_{steel}}{E_{spring}}$ were updated with 0.0% and 0.0% error respectively for the soft spring case and 0.0 and 16.6 % error for the stiff spring case.

A comparison between soft and stiff springs shows clear differences. For stiff springs, the system acted like the building was fixed at the bottom, due to the high spring stiffness. As a result, the dynamic properties were mainly controlled by the $\frac{E_{\text{steel}}}{\rho}$ ratio, and changes in spring stiffness had little effect. This made the range in predicted period lengthening much more narrow around the actual value: 100 % of all $\tilde{T}/T$ obtained across 100 solutions were within an error of 1 % of the actual value. For soft springs, however, the dynamic properties and period lengthening were much more sensitive to changes in the $\frac{E_{\text{steel}}}{E_{\text{spring}}}$ ratio. This caused larger errors across the solutions obtained, especially for the first natural frequency. For only 3 % of solutions, the error of $\tilde{T}/T$ was lower than 1 %.
In the second phase of this research, the same FE models (on soft and stiff springs) were updated, this time using measurement data. The goal was twofold: (1) to investigate the differences compared to the update based on synthetic data, and (2) to identify the optimization settings necessary to achieve stable, converged results.

Regarding (1), the update based on measurement data showed some similarities to the update using synthetic data in terms of how well the objectives (dynamic properties) were met. Again, the first natural frequency and the third mode shape proved to be the most difficult to fit accurately for the soft spring case. For the stiff spring, the spring stiffness was large and therefore the system had a period lengthening very close to one. In contrast to the update with synthetic data, the error with respect to period lengthening could not be lower than 2% (compared to the value of measurements), due to model and measurement errors. Additionally, the optimization process again focused on optimizing the ratios $\frac{E_{steel}}{\rho}$ and $\frac{E_{steel}}{E_{spring}}$, with the cost function clearly converging toward specific values for both ratios.

However, the results were not fully consistent: running the optimization multiple times with 100 initial values produced slightly different period lengthening results each time. To address this, and answer to (2), the number of starting points picked was varied. This decreased the variation of period lengthening values (lower standard deviation): a standard deviation of 0.019 for 50 starting points, 0.0127 for 100 starting points and 0.0092 for 200 starting points. However, the lowest cost function observed was not decreasing much: A ”plateau” in the cost function was observed near the measured period lengthening values, where further improvements in the cost function were minimal. This phenomenon was not present in the synthetic data. It appeared to result from the FE model's inability to fit all natural frequencies accurately. Some solutions within this plateau fitted the first natural frequency almost perfectly but diverged significantly for the higher natural frequencies. Similarly, different solutions exhibited varying accuracy for the MAC values. As a result, although the cost function values for these solutions were approximately the same, the material properties—and therefore the period lengthening—differed, because the optimization prioritized different natural frequencies and mode shapes.

Since the running with many starting points was time consuming, another approach was also adopted, with a second round of optimization after one with 200 starting values, but then starting from the optimized values obtained in the first round and reducing the bounds for the individual parameters to [0.9, 1.1]. Again, the plateau was observed, this time more clearly than previous method. Finally, this two-step procedure was applied to all building configurations, on two foundation types per configuration. for all configurations, the plateau could be observed, but for each a different width was obtained. When comparing to the measurements, it could be seen that the measured values of period lenghtening all fell within the plateau.
The results showed a significant improvement of the period lengthening values compared to the initial values found using the FE model for the case of the soft spring foundation, and only a slight improvement for the stiff spring foundation. This shows that model updating is a promising way to determine the period lengthening, but model and measurement uncertainties play a large role in the accuracy of the results. Therefore, more research is necessary to investigate these uncertainties, before a generalized approach can be adopted for real-life high rise buildings.

8 Recommendations

The findings of this research offer valuable insights that can guide future studies aimed at estimating period lengthening $\left(\frac{\tilde{T}}{T}\right)$ through model updating, a method optimizing structural properties based on dynamic characteristics. The period lengthening values estimated for real buildings may help develop more accurate damping predictors that incorporate soil-structure interaction (SSI) effects. Building on the results and challenges encountered in this study, several recommendations are proposed to support future research efforts.

In the discussion chapter, several factors were identified that negatively affect the reliability of the period lengthening values estimated in this research. Specifically, three sources of error and uncertainty were noted: (1) modeling inaccuracies, (2) measurement data errors, and (3) uncertainties within the optimization method. This chapter outlines several steps to better understand and mitigate these uncertainties. The recommendations chapter is organized into two sections: the first proposes ways to refine the current model to enhance its accuracy in predicting the dynamic behavior of the small-scale steel model, and the second section deals with recommendations that can be used to translate this research to applications for real-sized high-rise buildings.

8.1. Improving the current model

In this research, several implications arose when updates were performed using experimental data. For example, the cost function could not reach the low levels seen with synthetic data because the model was unable to match all measured frequencies and mode shapes simultaneously. One reason for this is model error: the inability of the model to exactly replicate the behavior of the real-life system. In addition, the non-linearity of the cost function created challenges in finding the optimal solution that best fit the data. This section proposes improvements to the current model that could result in better period lengthening estimates for the small-scale steel model.

8.1.1. Model errors

In this research, a 2D FE model consisting of Timoshenko beam elements was updated. When using measurement data rather than synthetic data as objectives for the optimization, several observations suggested model error. Improving the model's ability to predict dynamic behavior could reduce model error and improve convergence towards a stable period lengthening value. Some specific proposals to improve model accuracy include:

- Accounting for mass and stiffness added by corner connections, sensors, and other elements of the small-scale steel structure. This could be done for example by defining elements modeling these connectors.
- Modeling the springs in a different way to better capture the behavior of the rubber material.
- Extending the FEM model to 3D to include for example torsional modes.

Alternative model types may also be worth investigating. However, it is crucial that these models replicate the behavior of the system accurately. For example, an Euler Bernoulli-beam model might fit the natural frequencies and mode shapes of a high-rise building well, but it may not produce frequencies and mode shapes suitable for the small-scale steel model, which primarily exhibits shear-dominated behavior. Examples of model types that could be effective for the small-scale steel model include:

- Lumped parameter models
- Shear beam models
- Timoshenko beam models

8.1.2. Measurement errors

The second recommendation addresses errors and uncertainties in measurement data, particularly those associated with vibration measurements used to estimate natural frequencies and mode shapes. Measurement errors can introduce significant variability in results, especially in period lengthening estimates, which are highly sensitive to these dynamic properties.
To improve the accuracy of future model updates and reduce uncertainties arising from measurement errors, several strategies can be considered. First, efforts should be made to enhance the quality and quantity of measurement data to improve overall reliability and mitigate local inaccuracies. Future research could focus on the following methods to reduce measurement uncertainties:

- **Deploy additional sensors:** Add more sensors to the structure to capture additional data points across mode shapes, especially in directions not previously measured. This can provide more accurate and robust measurements by reducing the influence of individual sensor errors.
- **Expand measurement directions:** Capture measurements in a wider range of directions, allowing for a more complete representation of the structure's mode shapes and dynamic behavior. Currently, displacements in the vertical direction are only measured at the foundation, where errors in this sensor have a large effect.

8.1.3. Improving optimization approach

The third recommendation focuses on uncertainties associated with the optimization method itself. Quantifying the impact of the chosen optimization approach is important for improving the consistency, accuracy, and reliability of results. Several factors contribute to the effectiveness of the optimization process, including the specific algorithm used, the size and boundaries of the solution space, the number of optimization iterations, and the number of starting points sampled within the solution space.
To address these uncertainties, future work could involve:

- Implementing adaptive or multi-scale optimization techniques, where the solution space is refined based on intermediate results to focus on areas most likely to contain the optimal solution. This is more effective than simply increasing the number of starting points.
- Investigating the influence of varying the number of optimization steps and determining optimal stopping criteria that balance accuracy with computational efficiency.
- One component that does affect the results is the selection of the starting points, that operates on the basis of random selection of values. Therefore, results obtained in terms of solutions with lowest cost function might be slightly different. A more straight forward selection, not depending on a random selection, could ensure that repeating the work would yield the same results. Exploring strategies for selecting starting points, such as random sampling, clustering, or targeted sampling in regions with higher potential for optimal solutions.

8.2. Application to real high-rise buildings

This research aimed to determine period lengthening $\left(\frac{\tilde{T}}{T}\right)$ through model updating based on natural frequencies and mode shapes. To extend this approach to a broader set of buildings, potentially using measurements of natural frequencies and mode shapes, a clear framework is necessary to address the various issues and uncertainties associated with this method.

For applications to high-rise buildings, it is critical to understand and quantify the magnitude of model and measurement errors and their effect on period lengthening estimation. In real buildings, it is not feasible to extract period lengthening directly from measurements, as was possible with the small-scale steel model. Therefore, the approach cannot be directly applied by comparing estimated period lengthening values to actual measurements in a real-building context.

Using the small-scale steel model, a study should be designed to quantify the effect of measurement uncertainty. Specifically, the following approaches could be used to assess the influence of measurement errors:

- Applying random errors to the natural frequencies and mode shapes, similarly to the synthetic data approach in Chapter 5, to examine how these errors affect optimization results and to assess the significance of their impact.
- Following the method of Moretti et al. [21] by systematically excluding data from specific sensors to simulate the effect of missing or inaccurate measurements. This approach can help reveal the impact of incomplete measurement data on the optimization process and its outcomes.

The next step toward applying this method to real high-rise buildings is to select a model that can accurately predict the dynamic behavior of various buildings. An Euler-Bernoulli beam model, for example, might be suitable for buildings with significant bending behavior. A study should be conducted to identify which types of buildings are best modeled by an Euler-Bernoulli beam. Alternatively, other models, such as a Timoshenko beam model, could be considered. The selected model for updating should capture the dynamic behavior of the buildings accurately, and an argument for the model's general accuracy should be provided.

The third step is to investigate the effect of different model variables on the outcomes related to dynamic properties, such as the effects of variations in mass and stiffness. In this study, dimensions were assumed constant, with stiffness modeled as the product of Young's modulus (E) and the moment of inertia (I). However, Ritfeld [24] has shown that estimating the moment of inertia for real buildings is challenging, as floor-column connections significantly affect stiffness.

Another method to address these issues is to modify the optimization's objective function by placing greater emphasis on more reliable or important natural frequencies or mode shapes. By prioritizing data with higher accuracy or greater impact on period lengthening in the optimization process, the influence of measurement errors on the final results can be minimized. For example, the first natural frequency, which can often be estimated more accurately, provides valuable information about foundation stiffness (as it is more sensitive to this parameter).

References

[1] BESIX. *Exploring the Vibration Behaviour of Skyscrapers in the Netherlands*. Accessed on April 29, 2024. 2022. URL: `https://www.besix.com/en/news/besix-nl-exploring-the-vibration-behaviour-of-skyscrapers-in-the-netherlands` (visited on 04/29/2024).

[2] A. J. Bronkhorst, C. A. Van Bentum, and S. Sanchez Gomez. *Wind-induced Vibrations and Damping in High-Rise Buildings*. Tech. rep. 2018 R10644. TNO, 2018.

[3] A. J. Bronkhorst and C. P. W. Geurts. “Slappe ondergrond dempt trillingen van hoogbouw”. In: *Bouwen met Staal* 266 (2018), pp. 40–44.

[4] Carranza. “Wind-Induced Dynamic Response of High-Rise Buildings: The Effects of Soil-Structure Interaction and a Comparison with the Eurocode Approach”. MA thesis. TU Delft, 2022.

[5] A Carranza et al. “Simple soil-structure interaction model for wind-induced vibrations in high-rise buildings”. In: Oct. 2023.

[6] Computational Mechanics group at CEG. *Pyjive*. 2024. URL: `https://gitlab.tudelft.nl/cm/CIEM5110`.

[7] *CIRCOLARI tipo VV - BOBBINS type VV*. Standard production specifications for antivibration bobbins and mounts. Unnamed Manufacturer. 2024.

[8] Cristian Cruz and Eduardo Miranda. “Evaluation of Soil-Structure Interaction Effects on the Damping Ratios of Buildings Subjected to Earthquakes”. In: *Soil Dynamics and Earthquake Engineering* 101 (2017). Received 17 November 2016; Received in revised form 25 May 2017; Accepted 29 May 2017, pp. 206–215. ISSN: 0267-7261. DOI: `10.1016/j.soildyn.2017.05.034`. URL: `http://dx.doi.org/10.1016/j.soildyn.2017.05.034`.

[9] Cristian Cruz and Eduardo Miranda. “Insights into damping ratios in buildings”. In: *Earthquake Engineering Structural Dynamics* 50 (Oct. 2020), pp. 1–19. DOI: `10.1002/eqe.3356`.

[10] A. Davenport and P. Hill-Caroll. “Damping in Tall Buildings: Its Variability and Treatment in Design”. In: *Building Motion in Wind: Proceedings of a Session, in conjunction with the ASCE convention in Seattle*. Ed. by N. Isyumov. Vol. 1. ASCE. 1986.

[11] David Hamers. *Binnen- en buitenstedelijk bouwen in Nederland: een reflectie*. PBL-publicatienummer: 4309. Den Haag: Planbureau voor de Leefomgeving, 2020.

[12] *Hoog500 Grafieken*. https://hoog500.nl/grafieken. Accessed on Month Day, Year. Year Accessed.

[13] A. Jeary. *Designer’s Guide to the Dynamic Response of Structures*. First. The University Press, Cambridge, 1997.

[14] A. P. Jeary. “Damping in tall buildings-a mechanism and a predictor”. In: *Earthquake Engineering & Structural Dynamics* 14.5 (1986), pp. 733–750.

[15] K. Kaynardag and S. Soyöz. “Structural health monitoring of a tall building”. In: *Proceedings of the 2nd European Conference on Earthquake Engineering*. Istanbul, Turkey, 2014.

[16] S. Lagomarsino. “Forecast Models for Damping and Vibration Periods of Buildings”. In: *JWEIA* 48 (1993), p. 221.

[17] S. Lamb and K. C. S. Kwok. “Sopite syndrome in wind-excited buildings: productivity and well-being impacts”. In: *Building Research & Information* 45.3 (2017), pp. 347–358. DOI: `10.1080/09613218.2016.1190140`. eprint: `https://doi.org/10.1080/09613218.2016.1190140`. URL: `https://doi.org/10.1080/09613218.2016.1190140`.

[18] Elisa Marchelli. “Reducing the uncertainty in dynamic models of high-rise buildings by means of parameter identification”. Civil Engineering Master Degree Course LM-23, A.Y. 2022/2023. Master’s thesis. Genova, Italy: Università degli Studi di Genova, Polytechnic School, Civil and Environmental Engineering Department, 2023.

[19] Ministerie Volkhuisvesting, Ruimtelijke Ordening en Milieu. *Structuurvisie Randstad 2040 – naar een duurzame en concurrerende europese topregio*. Tech. rep. 2008.

[20] Davide Moretti, Aj Bronkhorst, and Chris Geurts. “Identification of the structural properties of a high-rise building”. In: May 2023.

[21] Davide Moretti, Aj Bronkhorst, and Chris Geurts. “Identification of the structural properties of a high-rise building”. In: May 2023.

[22] NEN. *NEN-EN 1990: Eurocode - Basis of structural design*. NEN Standard. Nederlands Normalisatie-instituut (NEN), 2002.

[23] NIST. *Soil-Structure Interaction for Building Structures*. U.S. Department of Commerce. Gaithersburg, MD 20899, 2012.

[24] Isa Sophie Ritfeld. “Identification of structural properties of high-rise buildings: Application of a model updating technique for estimating the structural properties of high-rise buildings”. Student Number: 4892534. Master’s thesis. Delft, The Netherlands: Technical University of Delft, 2024.

[25] Gemeente Rotterdam. *Hoogbouwvisie 2019*. Tech. rep. Rotterdam, Netherlands: Gemeente Rotterdam, 2019.

[26] Sergio Sanchez Gomez, Chris Geurts, and Andrei Metrikine. “On the importance of soil damping for tall buildings loaded by wind”. In: *Engineering Structures* 163 (May 2018), pp. 426–435. DOI: 10.1016/j.engstruct.2017.11.029.

[27] S. Sánchez Gómez. “Energy flux method for identification of damping in high-rise buildings subject to wind”. doctoral thesis. TU Delft Offshore Engineering, Mar. 2019. DOI: 10.4233/uuid:bc4fe937-2711-4ee0-95b7-baad7c5d234c. URL: https://doi.org/10.4233/uuid:bc4fe937-2711-4ee0-95b7-baad7c5d234c.

[28] R. Smith and M. Willford. “Damping in Tall Buildings – Uncertainties and Solutions”. In: January (2008), pp. 66–67.

[29] Y. Tamura, K. Suda, and A. Sasaki. “Damping in Buildings for Wind Resistant Design”. In: *Proc. Int. Symp. on Wind and Structures for the 21st Century*. Cheju, Korea, 2000, pp. 115–130.

[30] The European Union Regulation. *EN 1991-1-4 Eurocode 1: Actions on structures - Part 1-4: General actions - Wind actions*. Tech. rep. 2005. 2011.

[31] W. Torres et al. “Operational modal analysis and FE model updating of the Metropolitan Cathedral of Santiago, Chile”. In: *Engineering Structures* 143 (2017), pp. 169–188.

[32] A Tsouvalas. *Soil Structure Interaction*. Lecture slides. 2023.

[33] Anestis S. Veletsos and Jethro W. Meek. “Dynamic Behaviour of Building-Foundation Systems”. In: *Earthquake Engineering and Structural Dynamics* 3 (1974), pp. 121–138.

[34] B. Vivek and Prishati Raychowdhury. “Influence of SSI on Period and Damping of Buildings Supported by Shallow Foundations on Cohesionless Soil”. In: *Journal of Geotechnical and Geoenvironmental Engineering* 17.8 (2017), p. 04017030. DOI: 10.1061/(ASCE)GM.1943-5622.0000890.

[35] John P. Wolf. “Simple Physical Models for Foundation Dynamics”. In: *Proceedings of the Third International Conference on Recent Advances in Geotechnical Earthquake Engineering and Soil Dynamics* II (Apr. 1995), pp. –.

[36] J.R. Wu and Q.S. Li. “Finite element model updating for a high-rise structure based on ambient vibration measurements”. In: *Engineering Structures* 26 (2004), pp. 979–990.

A

Assumptions to determine foundation- and building-damping

In this chapter, a summary is provided on the various models and assumptions used by several researchers for the estimation of building- and foundation-damping, used to calculate a modified overall damping ratio of the fundamental mode, using equation:

$$\zeta_0 = \zeta_f + \frac{1}{\frac{\widetilde{T}}{T}^n}\zeta_b \tag{A.1}$$

A.0.1. Foundation damping

Foundation damping consists of damping in the form of energy radiating away (radiation damping) and energy loss in the form of deformation of the soil (hysteretic damping)[23]. Bronkhorst and Geurts [3] and Gomez et al. [26] assumed hystereric damping to be negligible and estimated radiation damping using Wolf's cone model [35]. This model assumes a a rigid disk on the surface of a homogeneous soil halfspace (so no embedment, which is often the case with foundations). The model prescribes equations for calculating the soil stiffness and damping properties. For foundation damping, the following equation is introduced:

$$\zeta_f = \frac{\left(\frac{\widetilde{T}}{T}\right)^2 - 1}{\left(\frac{\widetilde{T}}{T}\right)^2}\zeta_s + \frac{1}{\left(\frac{\widetilde{T}}{T_x}\right)^2}\zeta_x + \frac{1}{\left(\frac{\widetilde{T}}{T_r}\right)^2}\zeta_r \tag{A.2}$$

Where, ζ_s represents the hysteresis (or internal damping) of the ground, ζ_x and ζ_r are the damping values for radiation damping in the translation and rotation directions, respectively. T_x and T_r are fictitious vibration periods, calculated as if there were only vibration in the translation or rotation direction of the foundation. Bronkhorst and Geurts [3] concluded that the overall damping computed with the model was notably lower than the measured values in a case study. They identified the exclusion of hysteretic damping from the calculations as one of the possible contributing factors to this underestimation. In another study, Bronkhorst et al. [2] compared the results of Wolf's cone model to results computed with commercial software Dynapile, in order to assess the influence of the piled foundation. Dynapile is a 3D, Boundary Element Method (BEM) and Finite Element Method (FEM) model of the pile foundation and returns a dynamic stiffness matrix of which the real terms represent stiffness and the imaginary terms represent damping:

$$
\begin{aligned}
k_x &= \text{Re}\left[\widetilde{K}_{tt}\left(2\pi f_{n,EC}\right)\right] \\
k_{yy} &= \text{Re}\left[\widetilde{K}_{yy}\left(2\pi f_{n,EC}\right)\right] \\
\zeta_x &= \frac{\text{Im}\left[\widetilde{K}_{tt}\left(2\pi f_{n,EC}\right)\right]}{2\pi f_{n,EC}} \\
\zeta_{yy} &= \frac{\text{Im}\left[\widetilde{K}_{yy}\left(2\pi f_{n,EC}\right)\right]}{2\pi f_{n,EC}}
\end{aligned}
\tag{A.3}
$$

Important to note is that the imaginary part of the dynamic stiffness matrix, which represents damping, cannot be separated into a material and radiation damping. In addition, soil damping parameters are not computed but should be entered. For example, Carranza [4] used the Linear complex stress-strain model in Dynapile. This model requires the damping coefficient η, which Carranza assumed a value for. Cruz and Miranda [9] used a model introduced by Veletsos and Meek [33] which assumes a circular shallow foundation on an elastic halfspace. Veletsos and Meek did not describe material damping, but only assumed radiation damping. This can be seen in the following equation for overall damping:

$$
\tilde{\zeta} = \left| \left(\frac{\tilde{f}}{f}\right)^3 \left[\zeta + \frac{(2-\nu)\pi^4\delta}{2\sigma^3}\left(\frac{\beta_x}{\alpha_x\left(\alpha_x + ia_0\beta_x\right)}\frac{r^2}{h^2} + \frac{\beta_\theta}{\alpha_\theta\left(\alpha_\theta + ia_0\beta_\theta\right)}\right)\right]\right|
\tag{A.4}
$$

where ζ represents structural damping or D_s, the first term between brackets with β_x represents translational radiation damping and the third term with β_θ represents rocking motion radiation damping.α_x, α_θ, β_x, and β_{theta} are dimensionless factors which can be deduced from certain graphs [33].
For wind-induced vibrations however, radiation damping is very small to negligible, according to Malekjafarian et al. (2021), Venanzi et al. (2014) and Bronkhorst et al (2018). This could mean that the only factor influencing the damping of the foundation is hysteretic damping.

A.0.2. Building or structural damping

For structural damping, Bronkhorst and Geurts [3], Gomez et al. [26] and Carranza et al [5] use the empirical estimator by Jeary. This equation takes into account the reduction of damping with increased flexibility, but does not capture solely structural damping. It includes other forms of energy dissipation, also foundation damping, therefore it is a conservative value. Cruz and Miranda [9] simply assumed 2% as a value for structural damping, in order to match the value of the paper by Veletsos and Meek [33]. A more accurate estimation of building damping excluding foundation damping is therefore needed to make sure the SSI model accurately predicts dynamic behaviour.

B
Overview setups

In the table below, an overview of the experiments is given. Notice that 15 experiments involve excitation in the x direction and 15 experiments in the y direction.

Table B.1: Overview of the experiments

Direction of Excitation	Setup No.	% 1.5mm columns	Configuration	Base conditions
x	01	100	C1	Fixed
x	03	90	C2	Fixed
x	05	80	C3	Fixed
x	07	60	C4	Fixed
x	09	40	C5	Fixed
x	11	30	C6	Fixed
x	13	20	C7	Fixed
x	15	20	C7	Soft
x	17	30	C6	Soft
x	19	40	C5	Soft
x	21	20	C7	Soft
x	23	20	C7	Stiff
x	25	30	C6	Stiff
x	27	40	C5	Stiff
x	29	20	C7	Stiff
y	02	100	C1	Fixed
y	04	90	C2	Fixed
y	06	80	C3	Fixed
y	08	60	C4	Fixed
y	10	40	C5	Fixed
y	12	30	C6	Fixed
y	14	20	C7	Fixed

Table B.1: (continued)

Direction of Excitation	Setup No.	% 1.5mm columns	Configuration	Base conditions
y	16	20	C7	Soft
y	18	30	C6	Soft
y	20	40	C5	Soft
y	22	20	C7	Soft
y	24	20	C7	Stiff
y	26	30	C6	Stiff
y	28	40	C5	Stiff
y	30	20	C7	Stiff

Marchelli [18] saved the results of the operational modal analysis in text files, numbered `t_00aa`, where `aa` represents the file number. `t_0001` is the first file number, corresponding to setup 01 in the x direction. `t_0002` is the second file number, corresponding to setup 01 in the y direction. `t_0003` is the third file number, corresponding to setup 02 in the x direction, and so on...

The setups in x direction:

Table B.2: Setups in x direction

Configuration Foundation condition	Fixed	Soft	Stiff
C5	09	19	27
C6	11	17	25
C7	13	16	23

The setups in y direction:

Table B.3: Setups in y direction

Configuration Foundation condition	Fixed	Soft	Stiff
C5	10	20	28
C6	12	18	26
C7	14	22	30

So we have 6 combinations of a building configuration combined with 3 different soil types. We want to store the natural frequencies of each configuration-foundation combination and compare the period lengthening that is measured to the period lengthening that is estimated through model updating of a simple beam model. We will save the data in a nested dictionary.

C

Timoshenko Beam Elements

The equation of motion for the system can be expressed as:

$$\mathbf{M}\frac{d^2\mathbf{u}}{dt^2} + \mathbf{K}\mathbf{u} = \mathbf{F}(t) \tag{C.1}$$

Where:

- **M** is the mass matrix,
- **C** is the damping matrix,
- **K** is the stiffness matrix,
- **u** is the displacement vector,
- $\mathbf{F}(t)$ is the external force vector as a function of time,
- $\frac{d^2\mathbf{u}}{dt^2}$ is the acceleration vector,
- $\frac{d\mathbf{u}}{dt}$ is the velocity vector.

This equation governs the dynamic behavior of the system and can be used to analyze its response to various loading conditions. To obtain natural frequencies and mode shapes, the external force is set to zero:

$$\mathbf{M}\frac{d^2\mathbf{u}}{dt^2} + \mathbf{K}\mathbf{u} = 0 \tag{C.2}$$

C.0.1. Element Stiffness Matrices

The stiffness matrix for a Timoshenko beam element is given by:

$$\mathbf{K}_{\text{element}} = \begin{bmatrix} EA/L & 0 & 0 & -EA/L & 0 & 0 \\ 0 & 12EI/L^3 & 6EI/L^2 & 0 & -12EI/L^3 & 6EI/L^2 \\ 0 & 6EI/L^2 & 2kGA/L & 0 & -6EI/L^2 & kGA/L \\ -EA/L & 0 & 0 & EA/L & 0 & 0 \\ 0 & -12EI/L^3 & -6EI/L^2 & 0 & 12EI/L^3 & -6EI/L^2 \\ 0 & 6EI/L^2 & kGA/L & 0 & -6EI/L^2 & 2kGA/L \end{bmatrix} \tag{C.3}$$

We define G as:

$$G = \frac{E}{2(1+\nu)} \tag{C.4}$$

Substituting this into the stiffness matrix with shear deformation effects, we have:

$$\mathbf{K}_{\text{element}} = \begin{bmatrix} EA/L & 0 & 0 & -EA/L & 0 & 0 \\ 0 & 12EI/L^3 & 6EI/L^2 & 0 & -12EI/L^3 & 6EI/L^2 \\ 0 & 6EI/L^2 & 2k\frac{E}{2(1+\nu)}A/L & 0 & -6EI/L^2 & k\frac{E}{2(1+\nu)}A/L \\ -EA/L & 0 & 0 & EA/L & 0 & 0 \\ 0 & -12EI/L^3 & -6EI/L^2 & 0 & 12EI/L^3 & -6EI/L^2 \\ 0 & 6EI/L^2 & k\frac{E}{2(1+\nu)}A/L & 0 & -6EI/L^2 & 2k\frac{E}{2(1+\nu)}A/L \end{bmatrix} \tag{C.5}$$

Simplifying the shear terms, we get:

$$\mathbf{K}_{\text{element}} = \begin{bmatrix} EA/L & 0 & 0 & -EA/L & 0 & 0 \\ 0 & 12EI/L^3 & 6EI/L^2 & 0 & -12EI/L^3 & 6EI/L^2 \\ 0 & 6EI/L^2 & k\frac{EA}{1+\nu} & 0 & -6EI/L^2 & k\frac{EA}{1+\nu} \\ -EA/L & 0 & 0 & EA/L & 0 & 0 \\ 0 & -12EI/L^3 & -6EI/L^2 & 0 & 12EI/L^3 & -6EI/L^2 \\ 0 & 6EI/L^2 & k\frac{EA}{1+\nu} & 0 & -6EI/L^2 & 2k\frac{EA}{1+\nu} \end{bmatrix} \tag{C.6}$$

For the steel building mounted on springs, only two elements types are used. Their element stiffness matrices look like:

$$\mathbf{K}_{steel} = E_{steel} \begin{bmatrix} \frac{A}{L} & 0 & 0 & -\frac{A}{L} & 0 & 0 \\ 0 & \frac{12I}{L^3} & \frac{6I}{L^2} & 0 & -\frac{12I}{L^3} & \frac{6I}{L^2} \\ 0 & \frac{6I}{L^2} & \frac{kA}{1+\nu} & 0 & -\frac{6I}{L^2} & \frac{kA}{1+\nu} \\ -\frac{A}{L} & 0 & 0 & \frac{A}{L} & 0 & 0 \\ 0 & -\frac{12I}{L^3} & -\frac{6I}{L^2} & 0 & \frac{12I}{L^3} & -\frac{6I}{L^2} \\ 0 & \frac{6I}{L^2} & \frac{kA}{1+\nu} & 0 & -\frac{6I}{L^2} & 2\frac{kA}{1+\nu} \end{bmatrix} \tag{C.7}$$

and

$$\mathbf{K}_{springs} = E_{springs} \begin{bmatrix} \frac{A}{L} & 0 & 0 & -\frac{A}{L} & 0 & 0 \\ 0 & \frac{12I}{L^3} & \frac{6I}{L^2} & 0 & -\frac{12I}{L^3} & \frac{6I}{L^2} \\ 0 & \frac{6I}{L^2} & \frac{kA}{1+\nu} & 0 & -\frac{6I}{L^2} & \frac{kA}{1+\nu} \\ -\frac{A}{L} & 0 & 0 & \frac{A}{L} & 0 & 0 \\ 0 & -\frac{12I}{L^3} & -\frac{6I}{L^2} & 0 & \frac{12I}{L^3} & -\frac{6I}{L^2} \\ 0 & \frac{6I}{L^2} & \frac{kA}{1+\nu} & 0 & -\frac{6I}{L^2} & 2\frac{kA}{1+\nu} \end{bmatrix} \tag{C.8}$$

The E modulus is taken in front of these matrices since all other parameters are known and this variable is scaled equally for all members during the update. When the global stiffness matrix is assembled, it will have terms dependent on E_{steel}, some terms dependent on $E_{springs}$, and some terms dependent on the sum of E_{steel} and $E_{springs}$. A visual representation of this can be found in figure C.1.

C.0.2. Element mass Matrices

The element mass matrix for a Timoshenko beam element can be expressed as:

$$\mathbf{M}_{\text{element}} = \frac{\rho AL}{6} \begin{bmatrix} 2 & 0 & 0 & 1 & 0 & 0 \\ 0 & 12 & 6L & 0 & -12 & 6L \\ 0 & 6L & 4L^2 & 0 & -6L & 2L^2 \\ 1 & 0 & 0 & 2 & 0 & 0 \\ 0 & -12 & -6L & 0 & 12 & -6L \\ 0 & 6L & 2L^2 & 0 & -6L & 4L^2 \end{bmatrix} \tag{C.9}$$

Where:

- ρ = density of the material,
- A = cross-sectional area,
- L = length of the beam element.

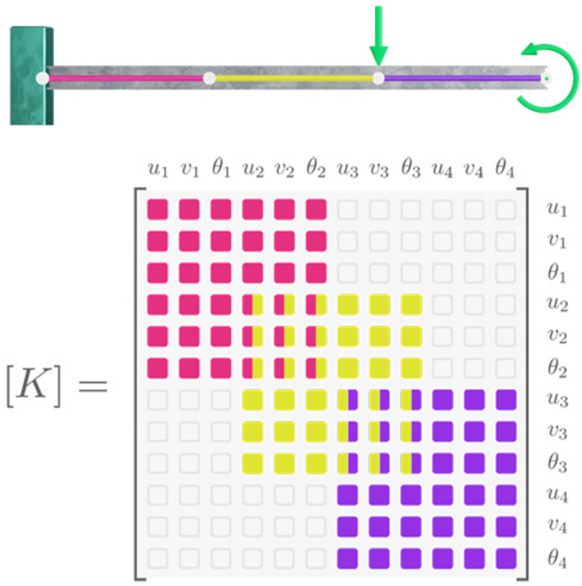

Figure C.1: Example of terms in a global stiffness matrix

This mass matrix accounts for both translational and rotational inertia in the Timoshenko beam element. Assuming all variables are constants, we can factor out ρ from the mass matrix:

$$\mathbf{M}_{\mathbf{element}} = \rho \begin{bmatrix} \frac{AL}{3} & 0 & 0 & \frac{AL}{6} & 0 & 0 \\ 0 & 12\frac{AL^3}{3} & 6\frac{AL^2}{3} & 0 & -12\frac{AL^3}{3} & 6\frac{AL^2}{3} \\ 0 & 6\frac{AL^2}{3} & 4\frac{AL^2}{3} & 0 & -6\frac{AL^2}{3} & 2\frac{AL^2}{3} \\ \frac{AL}{6} & 0 & 0 & \frac{AL}{3} & 0 & 0 \\ 0 & -12\frac{AL^3}{3} & -6\frac{AL^2}{3} & 0 & 12\frac{AL^3}{3} & -6\frac{AL^2}{3} \\ 0 & 6\frac{AL^2}{3} & 2\frac{AL^2}{3} & 0 & -6\frac{AL^2}{3} & 4\frac{AL^2}{3} \end{bmatrix} \tag{C.10}$$

Where:

- ρ = density of the material,
- A = cross-sectional area,
- L = length of the beam element.

The mass of the springs is set to zero, and therefore, all terms in the global stiffness matrix corresponding to the springs will also be set to zero.
The total system will now look like:

$$\rho\mathbf{A}\frac{d^2\mathbf{u}}{dt^2} + E_{steel}\mathbf{K}(\frac{E_{springs}}{E_{steel}})\mathbf{u} = 0 \tag{C.11}$$

where we have a purely geometric matrix $\boldsymbol{A}$, and the **K** matrix consisting only of $E_{springs}/E_{steel}$ terms. If we divide the system by ρ, we obtain:

$$\mathbf{A}\frac{d^2\mathbf{u}}{dt^2} + \frac{E_{steel}}{\rho}\mathbf{K}(\frac{E_{springs}}{E_{steel}})\mathbf{u} = 0 \tag{C.12}$$

So the only two ratios defining the system now are E_{steel}/ρ and $E_{springs}/E_{steel}$. If these ratios are kept the same, the system's dynamic properties (mode shapes and frequencies) will also remain the same.

C.1. Influence of ρ

From figure 5.9a, it can be concluded that period lengthening is independent of the density ρ. Consequently, not updating ρ during the optimization process may be advantageous, as the primary ratio that governs the period lengthening is $\frac{E_{steel}}{E_{spring}}$.

Interestingly, when the updating procedure is repeated with ρ fixed at 7840 kg/m^3, the errors in the natural frequencies increase significantly. In figure C.2a, errors up to 200 % can be seen. There is however still a small peak around zero error. The percentage of f_1 solutions within 1% error was 1.00%, while for f_2 solutions it is 17.00%, and for f_3 solutions it is 15.00%.

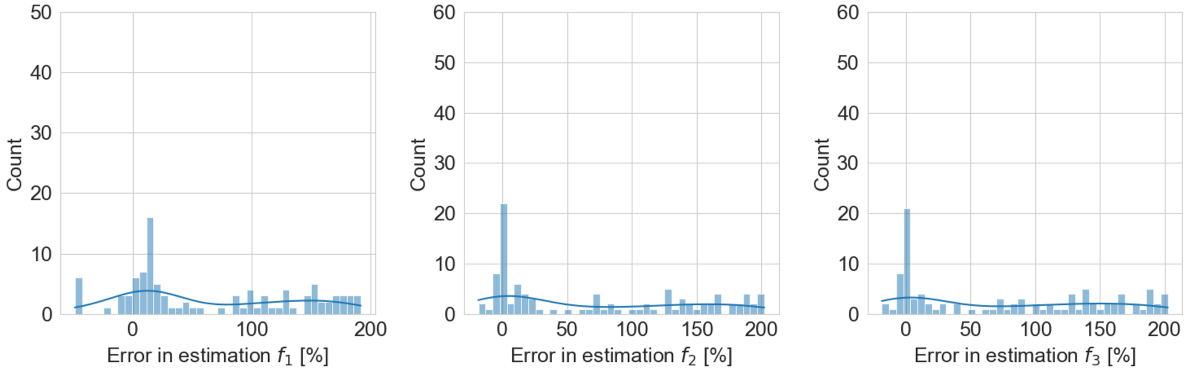

(a) Error distribution for the first three natural frequencies obtained from the updating procedure with parameter ρ fixed. The errors are calculated by comparing the natural frequencies obtained from the updating procedure with those of the reference model.

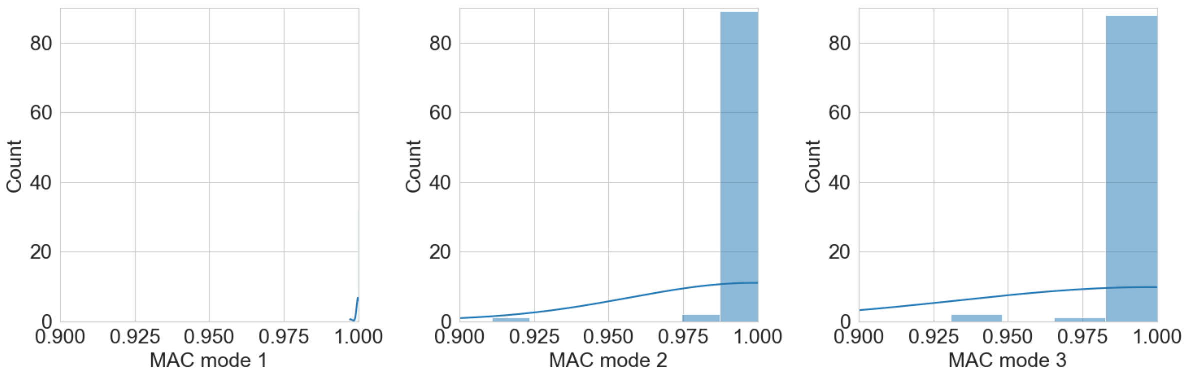

(b) MAC value distribution for the first three modes obtained from the updating procedure, compared to the mode shapes of the reference model. In this case, parameter ρ was fixed.

Figure C.2: Errors in estimation of dynamic properties of the reference model.

The observed behavior can be explained by two factors. Firstly, with ρ fixed, the starting value of E_{steel} in the optimization process needs to change more significantly to achieve the optimal E_{steel}/ρ ratio. This increases the likelihood of the optimization ending in a local minimum. Secondly, the chance of converging to a local minimum is further increased because the MAC values are optimized based primarily on the $\frac{E_{steel}}{E_{spring}}$ ratio. As demonstrated in the sensitivity study in figure 4.5, ρ has no impact on the mode shapes, since the mass is uniformly distributed across the structure's height. By fixing ρ, the optimization algorithm may find a local minimum where the mode shapes are satisfied, optimizing the $\frac{E_{steel}}{E_{spring}}$ ratio. This is supported by figure C.2b, where the MAC values remain close to 1 for the first mode and only show minor deviations for the second and third modes, consistent with **??**. Since the natural frequencies are more sensitive to the $\frac{E_{steel}}{\rho}$ ratio, they are not fully optimized, as ρ is fixed, and a local minimum is reached when the $\frac{E_{steel}}{E_{spring}}$ ratio produces high MAC values. The period lengthening is largely dependent on this ratio, which explains why 4.00% of the solutions for period lengthening fall within 1% error when ρ is fixed, compared to 5.00% in the case where ρ was not fixed. This small difference likely arises from the random selection of starting values, indicating that fixing ρ produces results that are almost equivalent when the objective is to match the period lengthening behavior.
In figure C.3 and figure C.4, it can be seen that when rho is not fixed, the optimization is still updating the $\frac{E_{steel}}{\rho}$ ratio. A clear convergence towards a value can be seen for this ratio, based on the cost

function. The value with the lowest cost function is at the $\frac{E_{steel}}{\rho}$ ratio of the reference model. Since ρ is fixed, and this ratio needs to be satisfied to obtain the proper dynamic properties (and thus a low cost function), the parameter E is also converging towards an optimal value. Therefore, this value will be closer to the actual physical value of the structure.
This study showed that it is beneficial to not fix rho, since it decreases the change that the updating procedure ends up in a local minimum. Therefore, larger bounds can be applied, meaning more uncertainty in the parameters is acceptable. When applying this procedure to real buildings, this is beneficial.

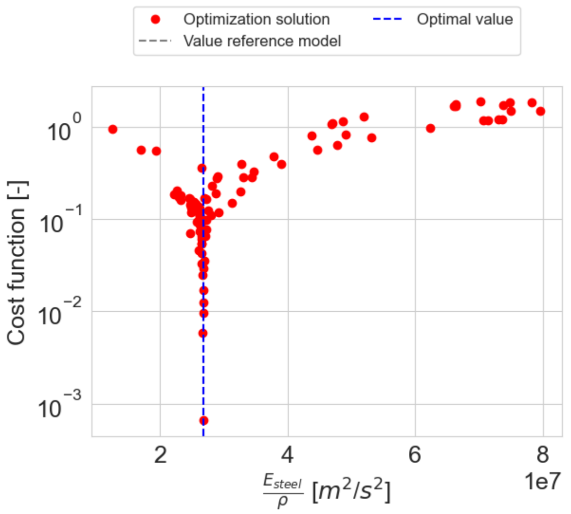

Figure C.3: Plot of the $\frac{E_{steel}}{\rho}$ ratios across the 100 solutions from the optimization algorithm. Dashed lines indicate value of the actual ratio (of the reference model) and optimal value obtained from the optimization.

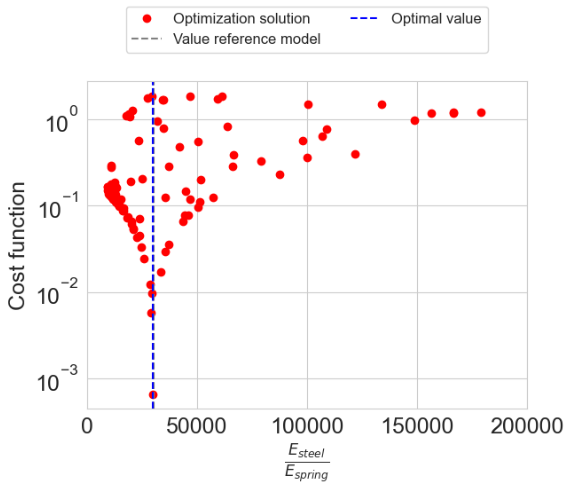

Figure C.4: Plot of the $\frac{E_{steel}}{E_{spring}}$ ratios across the 100 solutions from the optimization algorithm. Dashed lines indicate value of the actual ratio (of the reference model) and optimal value obtained from the optimization.

D

Sequential update

D.0.1. Sensitivity to local parameters

The second stage involved varying the stiffness of specific member types, such as the 1.5 mm thick columns, the floor plates, and the 2 mm thick columns. This was done to examine the effect of localized stiffness variation on the dynamic properties. This approach helped to identify specific members whose stiffness significantly influence the overall model behavior. The parameters investigated were $E_{column1,5}$, $E_{column2}$, E_{plate}, E_{base}, and ν (since the shear stiffness was calculated using equation (3.2)). Overall, one can see that a change in the stiffness of the 2mm thick columns have the largest effect on the natural frequencies and MAC-values. This is largely because these columns make up the largest part of the structure.

A change in stiffness of the springs has a large influence on the first natural fequency. For other natural frequencies, this effect is very small (less than 3% effect on frequency as well as MAC, against up to 19% for the first natural frequency.)

A change in stiffness of the baseplate (the plate that connects the columns at the bottom) has a negligible effect on both natural frequency and MAC.

Changes in stiffness of the horizontal plates do affect the natural frequency and the MAC. For all modes, this effect is approximately the same, with only a few percentage points difference.

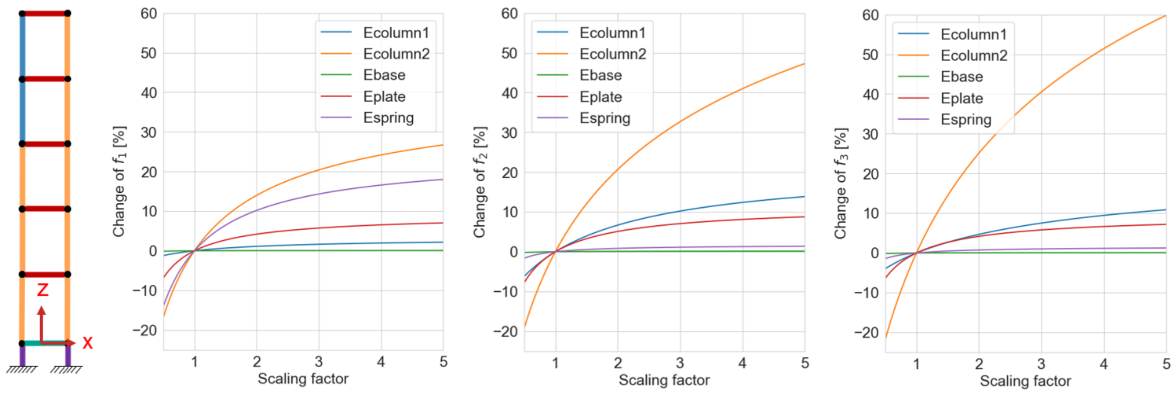

Figure D.1: Percentual change of the first three natrual frequencies resulting from scaling the parameters E_{spring}, E_{plate}, E_{base}, $E_{column1}$ and $E_{column2}$ individually. The x-axis represents the scaling factor applied to each parameter, while the y-axis indicates the corresponding percentage change in natural frequency. The colors of the lines correspons to the colors of the 2D FEM-model on the left.

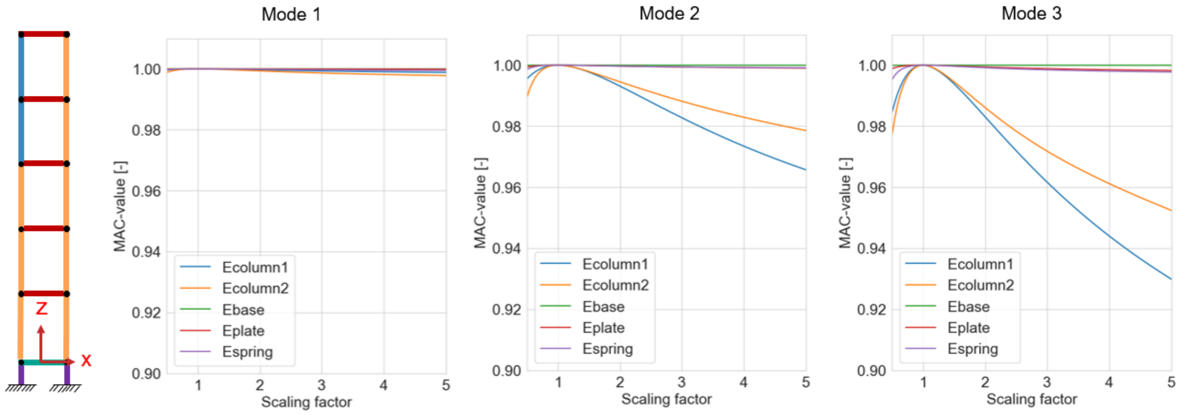

Figure D.2: Percentual change of the first three modeshapes measured in means of MAC value resulting from scaling the parameters E_{spring}, E_{plate}, E_{base}, $E_{column1}$ and $E_{column2}$ individually. The x-axis represents the scaling factor applied to each parameter, while the y-axis indicates the corresponding change of the MAC-value of the specific mode. The colors of the lines correspons to the colors of the 2D FEM-model on the left.

D.1. Sequential Update

In this section, the results of the sequential update method are presented and compared with the direct update method. The primary distinction between the two approaches lies in how the building and spring properties are updated. In the direct method, both sets of properties are updated simultaneously, whereas in the sequential update, the building properties are updated first, followed by the spring properties. Although the sequential method offers a clearer separation of influences, it is not possible in real-world scenarios, as buildings cannot be placed on different foundation types.

The results are structured into three parts. First, the global parameters in the fixed-base configuration are updated and compared to the results from the direct update case. Next,local parameters are updated, to obtain the best fit for the frequencies and MAC possible. Finally, the spring stiffness update is examined and the period lengthening calculated.

D.1.1. Updating Fixed Base

The update settings and finite element model (FEM) configuration for the first step of the sequential update are illustrated in figure D.3. This figure provides a visual representation of the FEM model, including its objectives and update settings for this initial phase.

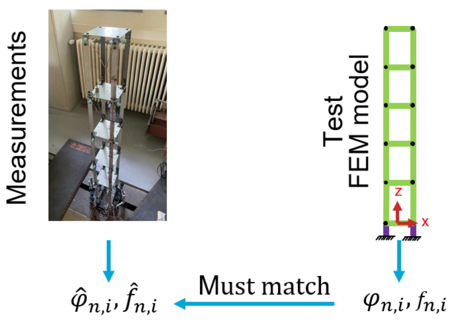

Configuration	C5, flexible base
Parameters updated	E_{steel}, rho_{steel}, E_{spring}
Bounds (equal for each parameter)	[0.3, 3]
Objective	3 $\hat{f}_{n,i}$ =[3.33, 12.05, 20.45] 3 $\hat{\varphi}_{n,i}$
Starting values	100, random

Figure D.3: Overview of the FEM model, its objectives, and update settings for the first step of the sequential update.

The resulting natural frequencies before and after the update are detailed in table D.1. The data demonstrates a significant reduction in errors following the update, achieving a minimum cost function of 0.079757. The MAC values, as expected, did not change, as no relative adjustments to stiffness or mass were made.
The natural frequencies show significant following the update, particularly for the first and second modes. For instance, the error for the first natural frequency dropped from 11.26% to 1.29%.

	Measurements	FEM model (before update)	FEM model (after update)	Error before update [%]	Error after update [%]
fn [Hz]	4.35	3.86	4.294025	11.26%	1.29%
	12.39	10.94	12.177268	11.72%	1.72%
	20.92	18.79	20.918612	10.18%	0.01%
MAC [-]	1	0.99992	0.99992	0.008%	0.008%
	1	0.99909	0.99909	0.091%	0.091%
	1	0.99424	0.99424	0.576%	0.576%

Table D.1: Comparison of measured values with FEM model predictions before and after the update for configuration C5 with fixed base conditions.

Like before, a fit of the frequencies does not mean that accurate structural properties are determined from the updating procedure. However, a clear pattern can be seen when the E/ρ ratio is plotted against the corresponding cost function that is obtained from the optimization. In figure D.4, this clear dependency of the cost function on the value of the E/ρ ratio can be seen. The optimized value from the sequential update closely matches the result from the direct method, with only a 0.43% difference in the E/ρ ratio, as seen in table D.2.

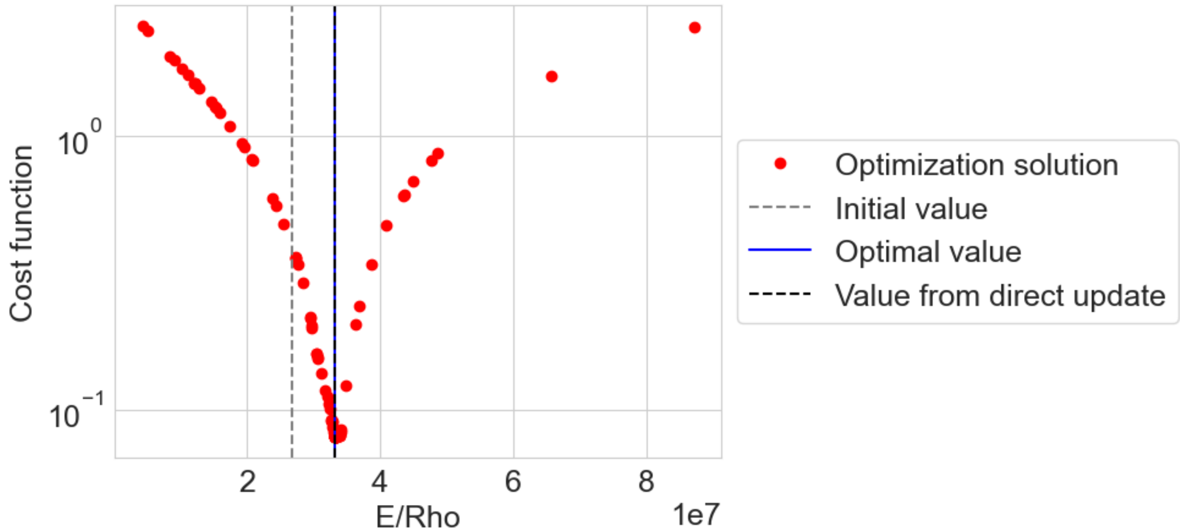

Figure D.4: E/ρ ratio against the corresponding cost function of each of the 100 solutions.

Cost Function (Direct)	Cost Function (Sequential)	Difference [%]	E/Rho Ratio (Direct)	E/Rho Ratio (Sequential)	Difference [%]
0.025158	0.079757	216.92%	33,325,150.37	33,182,544.47	0.43%

Table D.2: Comparison of cost functions and E/ρ ratios between direct and sequential updates.

D.1.2. Updating Local Variables

In the second step of the sequential update, local stiffness variations were introduced to allow different structural sections to be modified independently. In this step, ρ was fixed at the value from the solution with the lowest cost of the previous update step (47166.86) and only local stiffness properties were adjusted within bounds of [0.3, 3]. figure D.5 provides an overview of the second step of the sequential update.

Structural Properties

The updated values for the local stiffness properties are displayed in table D.3. Slight changes occur in the values of $E_{column1}$, $E_{column2}$ and E_{plate}, which are scaled by 1.056, 0.93 and 1.425 respectively. This change means that the plates behave much more stiff, and the columns of 2 mm thickness relatively behave less stiff.

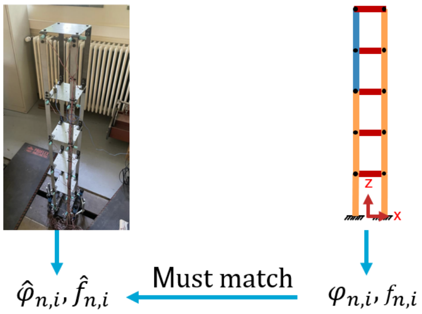

Configuration	C5, fixed base
Parameters updated	$E_{col1}, E_{col2}, E_{plate}$
Bounds (equal for each parameter)	[0.1, 10]
Objective	3 $\hat{f}_{n,i}$ =[4.35, 12.39, 20.92] 3 $\hat{\varphi}_{n,i}$
Starting values	100, random

Figure D.5: Overview of the FEM model, its objectives, and update settings for the second step of the sequential update.

Parameters	**Starting model** Value	**Updated model (lowest cost)** Bounds for update	Scalar applied	Updated value
$E_{column1}$ [Pa]	1.653×10^{12}	[0.3, 3]	1.056	1.653×10^{12}
$E_{column2}$ [Pa]	1.457×10^{12}	[0.3, 3]	0.93	1.457×10^{12}
E_{plate} [Pa]	2.232×10^{12}	[0.3, 3]	1.425	2.232×10^{12}

Table D.3: Updated structural properties after the second step of the sequential update, corresponding to the solution with the lowest cost function.

Dynamic Properties

The adjustment of local stiffness properties led to a substantial reduction in the cost function, from 0.079757 to 0.00647, marking a decrease of 91.89%. As demonstrated in table D.4, the errors in the first and second frequencies were reduced from 1.29% to -0.12% and from 1.72% to -0.37%, respectively, with only a slight increase in the error for the third frequency.

	Measurements	FEM model (after update)	FEM model (after second update)	Error before second update [%]	Error after second update [%]
fn [Hz]	4.35	4.294025	4.344655	1.29%	-0.12%
	12.39	12.177268	12.344666	1.72%	-0.37%
	20.92	20.918612	20.925055	0.01%	0.02%
MAC [-]	1	0.99992	0.999925	-0.008%	-0.0075%
	1	0.99909	0.999807	-0.091%	-0.0193%
	1	0.99424	0.998028	-0.576%	-0.1972%

Table D.4: Comparison of measured values with FEM model predictions before and after the second update for configuration C5 with fixed base conditions.

D.1.3. Updating spring stiffness

in this section, the resulting spring stiffness values are presented. Again, the value obtained for spring stiffness is not close to the actual value, nor the value from the manual. However, the optimization seeks to balance all stiffness parameters such that the dynamic behaviour is best replicated. More interesting is to investigate the influence of the parameter E_{spring} on the period lenghtening, and the way lower cost functions as a result of the E_{spring} choice cause more accurate results for the period lengthening when compared to measurements.

PL Measurements	PL Before Update	PL After Update	Error Before Update [%]	Error After Update [%]
1.306	1.246	1.305	-4.69	0.0625%

Table D.5: Comparison of period lengthening (PL) measurements, FEM model values before the update and after the final step in the sequential update, along with respective percentage errors.

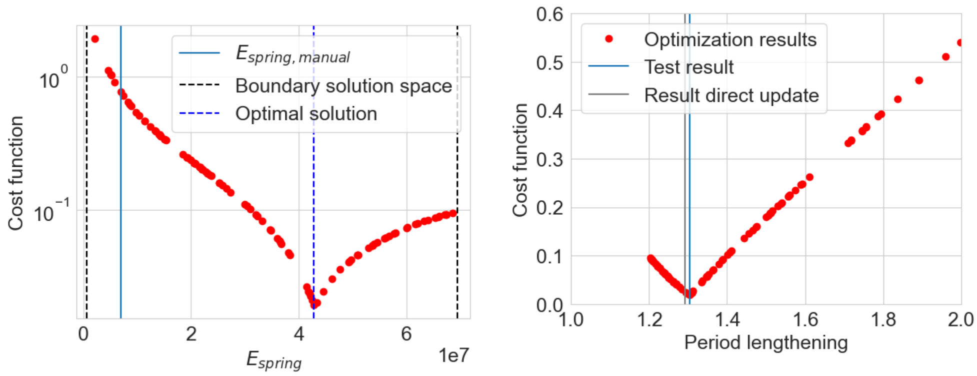

(a) E_{spring} values of all 100 solutions plotted against cost function. The vertical lines represent the value that were mentioned in the manual and optimal value obtained.

(b) Period lengthening values obtained from the 100 sequential optimization solutions plotted against the period lengthening. The vertical lines represent the test result and the result of the direct update.

Figure D.6: Results for the period lenthening and the value of the spring chosen. The value for the spring stiffness that leads to a low cost function, also leads to a period lenthening value that is close to the test result.